Neutral winds and tides over South Africa

A thesis submitted in fulfillment of the requirements
for the degree of

DOCTOR OF PHILOSOPHY

of

Rhodes University

by

Taiwo Theophilus Ojo

March 2022

Abstract

This thesis presents the first results of a climatology of nighttime thermospheric neutral winds between February 2018 and January 2019 measured by a Fabry-Perot interferometer (FPI) in Sutherland, South Africa (32.2°S, 20.48°E; geomagnetic latitude: 40.7°S). This FPI measures the nighttime oxygen airglow emission at 630.0 nm, which has a peak intensity at an altitude of roughly 250 km. The performance of the Horizontal Wind Model (HWM14) was evaluated by comparing results from HWM14 with the FPI measurements. The results showed that the model had a better agreement with the measurements for meridional component compared to the zonal component. In addition, the HWM14 zonal wind consistently peaked several hours ($\sim$3 h) prior to the measured wind, creating what looks like a phase shift compared to the measured wind. An investigation of this apparent phase shift revealed it to be a consequence of a difference in phase shift of the terdiunal tide. Since ionosondes are more prolific with wider temporal and spatial coverage than FPIs, nighttime meridional winds aligned to the magnetic meridian were inferred from the peak height (hmF2) of ionospheric data taken from South Africa ionosonde network using the servo model during February 2018–June 2019. These were compared with FPI measured meridional wind and benchmarked with HWM14 and Magnetic mEridional NeuTrAl Thermospheric (MENTAT) model. The amplitudes and trends of the calculated meridional winds across all four ionosonde stations agreed relatively well with the observed data, especially during the summer months. Furthermore, the results confirmed that the ionosonde station located closest to the FPI, i.e. Hermanus station, had better agreement with measurements compared to the stations located at further distances. The extraction and analysis of atmospheric tides, namely the diurnal, semidiurnal, terdiurnal and 6-hour components from the FPI as well as the long-term tidal winds variations from the thermospheric wind measurements were investigated. The results showed that the semidiurnal peak mostly had the highest peak across all the months, indicating that the semidiurnal tides dominate the dynamic structure of the upper mesosphere at midlatitudes, consistent with previous observation over midlatitudes. Futhermore, the signature of the diurnal tide in the meridional (zonal) wind was stronger in winter (summer) and weaker in summer (winter). Also, semidiurnal tide didn't show any trend with season, while the terdiurnal tide was dominant in summer (zonal) and winter (meridional). Lastly, the 6 hour tide was detected intermittently during the period of the study and had the weakest signature (i.e. lowest amplitudes).

Publications from this thesis

Ojo, T.T., Katamzi-Joseph, Z.T., Chu, K.T., Grawe, M.A. & Makela, J.J. (2021). A climatolog of the nighttime thermospheric winds over Sutherland, South Africa. Advances in Space Research, https://doi.org/10.1016/j.asr.2021.10.015.

Acknowledgement

First and foremost, I would like to thank my heavenly Father, the Father to the fatherless, the giver of wisdom, and the way maker. I want to thank Him for funding this project. Thank You for seeing me through the thick and thin of the study. You gave me hope when I had completely lost my hope, and now I can say, All things are possible to them that believe.

I am very much indebted to Dr. Zama Katamzi-Joseph, for giving me this golden opportunity to pursue a Ph.D. under her supervision. With her support, contributions, and guidance, I conducted this research. Thank you for accommodating and tolerating my sincere ignorance. You are indeed a great mentor!. My sincere appreciation goes to Prof Michael Kosch for his contributions to the success of this work and for supervising this work when my supervisor was briefly away. Thanks to the South African National Space Agency (SANSA) Space Science for providing required instruments and office space during my study. I will also like to thank all the staff of SANSA Space Science for their hospitality, encouragement, and support during my study. Special thanks to Prof Jonathan Makela, Kristina Chu (Department of Electrical and Computer Engineering, the University of Illinois at Urbana-Champaign, Urbana, IL, USA), and Dr Matthew Grawe for their contributions (Johns Hopkins University Applied Physics Laboratory Laurel, MD, USA).

Throughout this study, the great support from Tsige Atilaw, Dr Mike Heyns, Dr Mpho Tshisaphungo, Dr Daniel Okoh, and Dr Tshimangadzo Matamba in programming related issues is well appreciated. Special thanks to Golekamang Thaganyana and my fellow students for their contributions. A special thanks to Dr Damilola Folley for her motivations, support, encouragement, and kindness in many ways. I will not forget the immeasurable supports and encouragement from Dr Pierre Cilliers and Mrs Jeanne Cilliers. God only will reward you abundantly. My sincere appreciation goes to the Shofer family for their supports in all ramifications. You have been a source of blessing to me and my family. I want to specially thank my lovely wife, Olufunke Ojo, for all your unquantifiable support and my son, Joshua Ojo, who was born just a few days before my thesis submission indeed, you are a great joy to our family. I will like to express my gratitude to my family for their numerous supports.

Contents

List of Figures

List of Tables

Chapter 1

Introduction

The Earths atmosphere is a mixture of different gases, particles and aerosols collectively known as air, which envelops the Earth. It contains several highly concentrated gases, such as nitrogen (N_2), oxygen (O_2), and argon (Ar), and many trace gases, among them are water vapour (H_2O), carbon dioxide (CO_2), methane (CH_4), and ozone (O_3). The atmosphere can be conveniently described by the variation of its composition, density, pressure and temperature with altitude, the latter being widely used to describe its different layers (Häusler *et al.*, 2007; Prölss, 2004). The factors that play a significant role in atmospheric temperature variations include direct absorption of solar radiation, heating of the lowest layer on the Earths surface, and re-absorption of atmospheric infrared radiation primarily, reflected by atmospheric water vapour (Prölss, 2004). The Earths atmosphere is made up of five regions based on the altitude variation of temperature, as shown in Figure 1.1. The troposphere is the lowest atmospheric region and has a temperature gradient of -10 K/km at altitudes from the ground up to ~10-12 km. In this region, the atmosphere cools with increasing altitude until the absorption of ultraviolet solar radiation by ozone becomes important and the temperature increases, at which point the layer terminates. The stratosphere, a region where the temperature increases with altitude up to a maximum of about 270 K, lies above the troposphere and ends at an altitude of roughly 45-50 km. The mesosphere is the region of decreasing temperature with altitude and is located between 45 and 85 km. It is considered the coldest part of the Earth's atmosphere, with a minimum temperature found at around 85 km. The thermosphere is the region above the mesosphere where at an altitude roughly above 160 km the absorption of extreme solar ultraviolet (EUV) radiation causes the temperature to increase again until asymptotic to a constant value. The positive temperature gradient leads to temperatures greater than 1000 K in this region. The dominant constituents in this region are the molecular nitrogen (N_2), atomic oxygen (O), and molecular oxygen (O_2), and the minor constituents are helium (He) and argon (Ar) among other species.

The ionised part of the atmosphere, known as the ionosphere, sits across the mesosphere and the thermosphere with the largest part found in the latter. The ionosphere is electrically conductive and supports strong electric currents. It also plays an essential role in radio wave applications, as it can affect radio propagation. Above the thermosphere is the exosphere, a region at an altitude above 1000 km. It is usually defined as the region where the neutral density is so low that the atmosphere no longer acts like a fluid, and kinetic equations are necessary (Banks & Kockarts, 1973; Hargreaves, 1992).

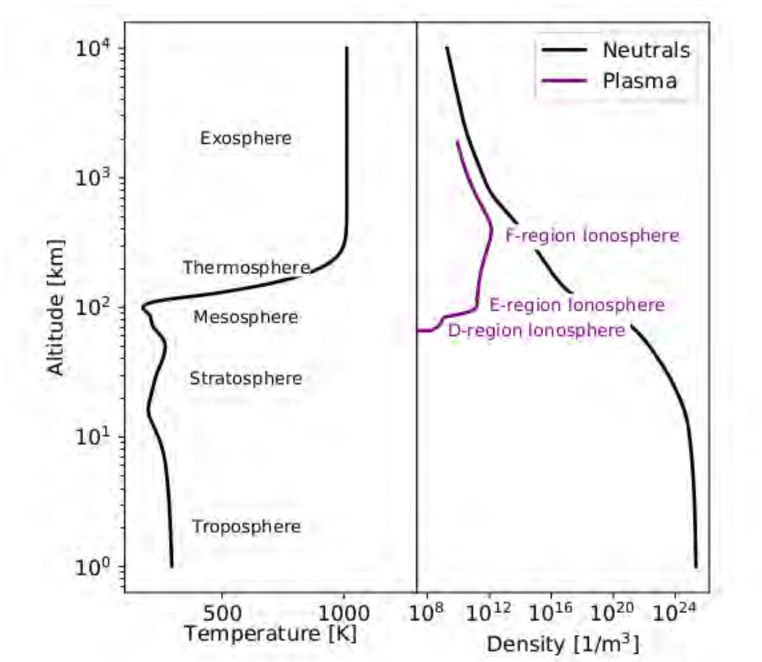

Figure 1.1: Typical profiles of neutral atmospheric temperature and ionospheric plasma density with the various layers designated. Figure adapted from Kelley (2009).

The thermosphere is of particular interest to this dissertation, because it contains the highest density plasma in geospace (the region of the outer space near Earth) and therefore contributes to space weather. Space weather refers to the Sun-driven variability in the Earths magnetosphere, thermosphere, and ionosphere that can affect the functioning and reliability of space-borne and ground-based systems and the services they provide, and which may lead to socio-economic losses (Nwankwo & Chakrabarti, 2018). Numerous studies have been made on a broad international level on how to understand and mitigate its impact on technical systems and to forecast its behaviour (e.g. Balan *et al.*, 2014; Baker & Lanzerotti, 2016; Nwankwo & Chakrabarti, 2018).

In the past few decades there has been an increase in technologies that rely on these space-based systems, e.g., global navigation satellite systems, communication, and earth observation satellites. It is therefore of huge importance to understand the dynamics of thermosphere-ionosphere, and how it influences these technologies. For example, the thermosphere-ionosphere system regulates energy transfer from space to the atmosphere and vice versa, and causes variations in satellite drag (Harding, 2017). Studying the motion of neutrals, i.e., neutral winds, can help better understand the thermosphere's underlying physics due to the higher concentration of neutrals present. Rees (1995) and Heelis (2004) reported that neutral winds greatly influence the dynamics in the upper atmosphere as they play a crucial role in the dynamics of the ionospheric F region as well as in the generation of electric fields and currents, instabilities, and Joule heating. Despite their significant contribution to ionospheric dynamics, themospheric winds are generally an insufficiently sampled parameters in the Earth's upper atmosphere. The most common instrument that measures the motion and temperature of the neutrals directly is the Fabry-Perot interferometer (FPI) which can be located on the ground or on-board satellites, such as the Ionospheric Connection Explorer (ICON) and Thermosphere-Ionosphere-Mesosphere, Energetics and Dynamics (TIMED) (Emmert *et al.*, 2002; Häusler *et al.*, 2007; Yu *et al.*, 2014; Fisher *et al.*, 2015). Most of the climatological studies of these neutral parameters have been conducted over the American and Asian longitudinal sectors, as well as the European mid-to-high latitude regions with the African continent largely unrepresented (e.g. Fisher *et al.*, 2015; Yu *et al.*, 2014; Xu *et al.*, 2019). However, over the past decade, there have been several FPI deployments in the African continent, making it possible to study neutral winds over the African sector. One of the first studies to report wind climatology over the African continent was by Fisher *et al.* (2015), using FPI measurements over Morocco, North Africa. Subsequent studies have been conducted by Tesema *et al.* (2017), Kaab *et al.* (2017) and Sivla *et al.* (2019) and Rabiu *et al.* (2021) over Ethiopia, Morocco and Nigeria respectively. Still, there has not been a detailed climatological study of neutral winds over the southern midlatitude region in Africa due to lack of observations. This has changed with the deployment of an FPI at Sutherland (32.2°S, 20.48°E; geomagnetic latitude: 40.7°S) in January 2018. Therefore, this thesis will investigate neutral wind variability, as well as tidal influence on this variability over South Africa using this instrument. Tidal signatures and their variability have been studied by means of different instruments and models across different latitudes, except over South Africa (e.g. Amayenc & Reddy, 1972; Forbes, 1982; Fisher *et al.*, 2002; Wang *et al.*, 2021).

1.1 Thesis Objectives

The main aim is to determine wind variability over South Africa and the factors that influence it. This project focuses on wind variability during quiet geomagnetic conditions, meaning our interest is mainly in the effects of waves from below on this variability rather than magnetospheric input from above. The objectives are:

- Derive thermospheric winds from the FPI located at Sutherland.

- Derive thermospheric winds over South Africa from ionospheric parameters measured by ionosondes in the South African ionosonde network.
- Extract and analyse signatures of atmospheric tides in the measurements of the thermospheric winds and determine their variability.

1.2 Thesis Overview

A brief theory of the thermosphere-ionosphere is given at the start of Chapter 2, which includes an overview of layers of the ionosphere and airglow, a crucial part of studying the thermosphere using a FPI. Thermospheric winds and atmospheric tides are discussed in the nal section of Chapter 2.

Chapter 3 will present the Instruments and data analysis. Then the theory, design, operation, and data processing behind the FPI and its use in measuring the thermospheric winds are discussed. A denition of ionosonde is given as this provides the measurement of hmF2 that would be used in the derivation of the meridional neutral wind, the principle of ionospheric sounding, and the ionograms and its interpretation are given, a derivation of ionosonde derived meridional neutral wind: servo model is given. Different space weather indices such as Kp, Ap indices, and Solar radio index ($F_{10.7}$) used to determine the space weather conditions are discussed. Finally, Chapter 3 comes to an end with data analysis techniques.

Chapter 4 presents the first climatological study of thermospheric winds over Sutherland, South Africa. Since FPI was used to validate HWM14, a brief description of HWM was given. Results of night-to-night variability of thermospheric winds and monthly averages of meridional and zonal winds were given. The discrepancies observed in the HWM14 zonal wind were investigated, and brief HWM14 correction: the terdiurnal tide was also presented. Lastly, a summary (discussion) of the results was presented.

An ionosonde-derived meridional neutral wind is explored in Chapter 5. This wind is derived using the hmF2 obtained from the South Africa ionosonde network since this model requires input parameters from other atmospheric models. Therefore, a brief discussion of the Mass-Spectrometer-Incoherent-Scatter (MSIS), the International Reference Ionosphere (IRI), and International Geomagnetic Reference Field (IGRF) models are given. One of the models that will be used to benchmark the servo model-the MENTAT model was briefly discussed. Data Analysis and comparison of different models were presented. The chapter is concluded with a summary of the results and conclusions.

Chapter 6 presents tidal variability in the thermospheric wind. Extraction and analysis of atmospheric tides, namely the diurnal, semidiurnal, and terdiurnal components, were done using the Lomb-Scargle spectrogram. Therefore, a brief discussion on this spectrogram was given. The chapter is concluded with a summary of the results and conclusions.

In Chapter 7, a summary of all the results and conclusions drawn are given. A brief discussion of possible future work and recommendations is also presented in this chapter.

Chapter 2

Theoretical background

In this chapter, the theoretical background of the thermosphere, ionosphere, thermospheric wind, and the airglow is described. In addition, an overview of basic terminology and mathematical formulations for thermospheric winds and atmospheric tides is presented.

2.1 Theory of the thermosphere-ionosphere

The thermosphere is a region of Earths atmosphere exhibiting low neutral density and strong coupling with the ionosphere. In a steady-state atmosphere the various gases in the thermosphere are in thermal equilibrium with each other and therefore fluid dynamic principles are valid. Figure 2.1 shows the exponential decrease of the neutral density (n) with height, as well as that of the densities of a few species found in thermosphere (e.g., O, O_2, N_2, He, Ar). This figure shows that the atomic oxygen (O), produced as a result of photodissociation of molecular oxygen (0_2), is the most dominant neutral species above approximately 200 km. At lower thermospheric altitudes N_2 is the most dominant species between 100 and 200 km, while O_2 is the most dominant species below 100 km, as also seen in Figure 2.1.

The energy source in the thermosphere is mainly the activity of the sun. The solar ultraviolet (UV) and extreme ultra-violet (EUV) radiations from the sun are responsible for the high temperatures observed in the thermosphere. Photochemical processes are the means by which this energy is transferred to the various thermospheric constituents in different latitudes. In addition, on a global basis, heating by various sources is essentially balanced by the downward thermal conduction and the radiative cooling by species such as nitric oxide, and results in the observed thermal structure of the thermosphere. Killeen *et al.* (1987) presents an excellent review on the global energy balance of the thermosphere, taking into account the various sources and sinks. The absorption of solar energy by different regions of the thermosphere generates pressure gradients on a global scale that drive neutral air circulation.

The thermosphere is coincidental with the ionosphere, a lightly ionized plasma region, i.e. comprising generally an equal number of free electrons and ions therefore electrically neu-

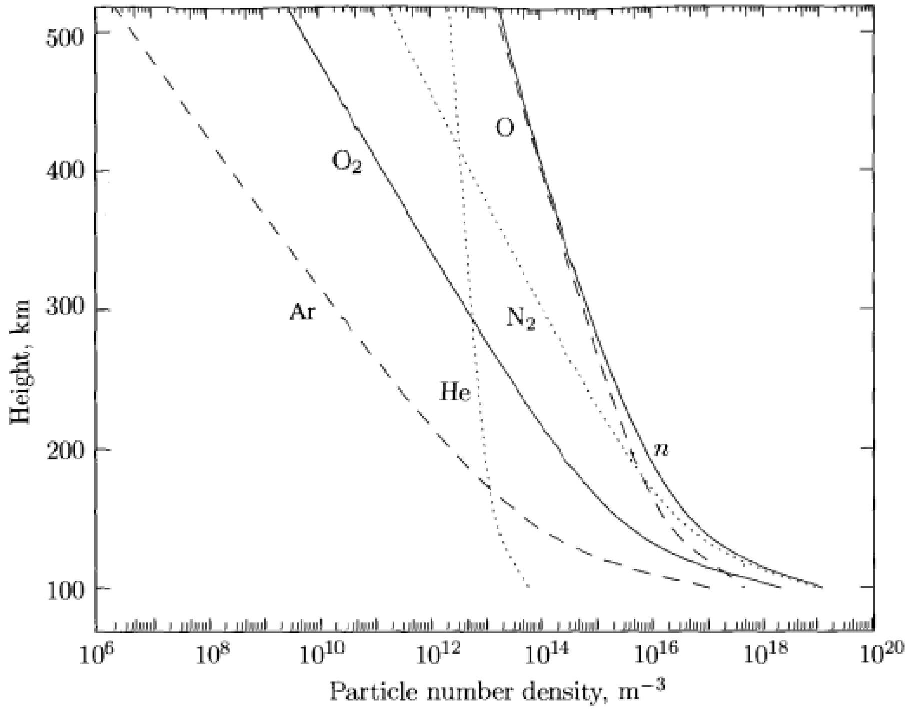

Figure 2.1: Typical number density profiles for neutral constituents in the thermopshere at an altitude of 100 to and 500 km, adapted from Prölss (2004).

tral, located at about $\sim$ 50–1000 km in altitude. The ionosphere has a sufficiently large concentration of plasma to affect the propagation of radio waves (Hunsucker & Hargreaves, 2007). Historically, Appleton & Barnett (1925) and Breit & Tuve (1926) were the first to use ionosondes to experimentally confirm the existence of the ionosphere. Since then, the ionosphere has been a subject of intensive study for its different roles in radio wave propagation and the need to fully understand space weather dynamics. As a refractive medium to radio waves, the ionosphere also affects a wide range of radio frequencies, from extremely low frequencies $\sim$ 3 kHz to super high frequencies $\sim$30 GHz (Davies, 1990).

The ionosphere is created by photo-ionisation, whereby extreme ultra-violet (EUV) radiation and high energy solar particles interact with the atoms/molecules in the mesosphere and thermosphere, which results in the electrons being stripped away from the parent atoms and molecules, creating a number of free negatively charged electrons and positively charged ions. The net value of the number of free electrons and ions in the ionosphere is determined by the rate of photo-ionisation and the rate at which specific species of ions recombine with electrons to form neutral atoms, through a process called recombination (McNamara, 1991; Baumjohann & Treumann, 1997).

Due to the varying chemical composition with altitude, different ionisation layers or regions are produced within the ionosphere, as illustrated by Figure 2.2 and detailed below:

- D layer: This layer has an altitude range of $\sim$ 50 km to $\sim$ 90 km. In this layer, ionisation is mainly by galactric cosmic rays and solar hard X-ray radiation, and is associated with NO, and at high solar activity with N_2 and O_2, to produce positive ions NO^+, O_2^+, and N_2^+ (Zolesi & Cander, 2014; Harding, 2017). This lower part of the ionosphere is weakly ionised due to the high neutral density in this layer, resulting in a high collision rate between electrons and neutral atoms and molecules, leading to a high recombination rate, and therefore tends to disappear during nighttime (Rishbeth & Garriott, 1969; McNamara, 1991). The other consequence of high neutral density in this layer is the absorption of high frequency (HF) radio signals, generally around 10 MHz and lower (McNamara, 1991).

- E layer: This layer of the ionosphere falls within altitudes of ∼90–140 km. Ionisation in the E layer is mainly soft X-rays and UV solar radiation of molecular oxygen, to produce NO^+, O_2^+, and N_2^+ (McNamara, 1991; Moldwin, 2008). Dense ionisation may cause HF radio waves to be reflected in long-distance communication (Rishbeth & Garriott, 1969).

- F layer: This layer is located between 140 and 600 km in altitude and is produced by EUV radiation. The principal ionisation of atomic O results in the formation of oxygen ion (O^+), and an electron. One of the intriguing features of the F-layer is the large variability it exhibits in its vertical motion, since transport processes, namely, diffusion and plasma drifts, compete with the photo-ionisation and recombination loss processes to take control of the behaviour of the entire F-layer. The F layer is present during the day and at nighttime. During the day, usually at noon, when the ion production rate is greatest, the F-layer splits into F1 and F2. This layer is a major segment of the terrestrial ionosphere and the most important from the point of view of radio communication and navigation systems (Zolesi & Cander, 2014). This layer is embedded in the thermospheric region, a crucial part of this work.

- Topside ionosphere: This region lies above the peak of the $F2$ layer and may extend to 1000 km. The electron density decreases sharply in this region to reach a minimum at higher altitudes. The topside ionosphere is characterised mainly by the presence of more H^+ ions than O^+ ions and subsequently H^+ ions are more dominant in the plasmasphere. Above the topside ionosphere is the plasmasphere, which forms the boundary of the ionosphere and extends into the outer space (Rishbeth & Garriott, 1969; Ratcliffe *et al.*, 1972; Liu *et al.*, 2007).

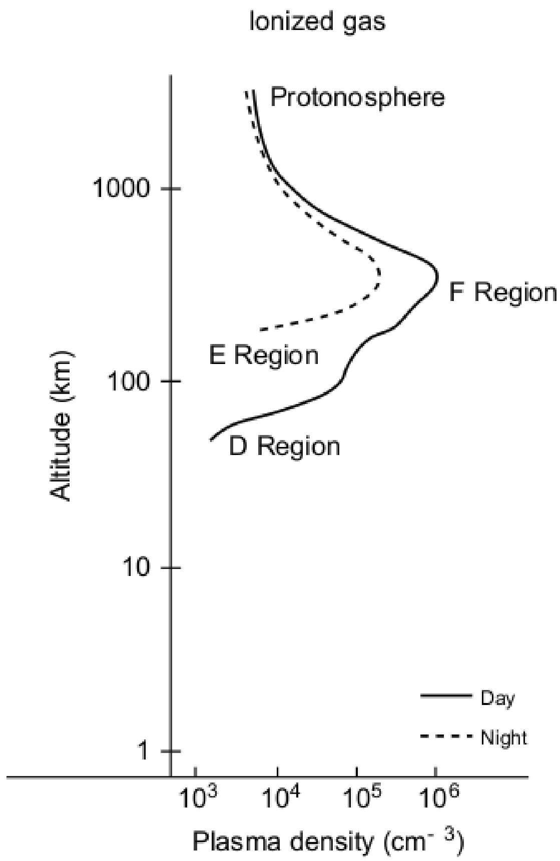

Figure 2.2: A schematic illustration of the ionospheric structure and the plasma density for both day time and night time, adapted from Kelley & Ulwick, 1988.

The various layers of the ionosphere, as discussed above, prove that the ionosphere is not stable. The variation in the ionosphere is interlinked with the sun and its activity under different space weather conditions. As a result, the ionosphere varies with time of day, season, geomagnetic activity and solar cycle. In addition, the ionosphere has distinct features in different latitudinal regions. The ionosphere and thermosphere are closely coupled, therefore, the study of the motion and behaviour of neutrals to better understand the motion of the plasma is possible. In this work, measurements of the F2 layer would be used to infer the movement of neutrals in the thermosphere, specifically measurements of the peak height of the F2 layer would be used to derive meridional neutral winds. The study of the thermospheric-ionospheric region is of particular interest, because it contains the highest density plasma in geospace, which affects propagation of radio signals which are also used by satellites. These satellites provide applications and technology that human life relies on for day-to-day activities. In addition, the thermospheric-ionospheric region is the home to many low-Earth orbit (LEO) satellites, that experience the effects of thermospheric winds and satellite drag that occur in this region (Harding, 2017; Chu, 2019).

2.2 Airglow

Airglow, otherwise known as "nightglow", occurs when various molecules are excited by photoionization during the daytime, and at night these molecules gradually release excess energy in the form of light (Herzberg & Spinks, 1944). Knowledge of natural chemiluminescence (airglow) is important in studying the thermosphere by means of a Fabry-Perot interferometer. The importance of airglow emission spectroscopy in monitoring the thermosphere and its various emission lines with their relative intensities was demonstrated and presented by Babcock (1923) and Chamberlain (1961). Measurements of Doppler parameters on the atomic oxygen green 557.7 nm, 630.0 nm, and 777.4 nm lines were made by several studies (e.g. Babcock, 1923; Bens *et al.*, 1965; Biondi & Feibelman, 1968; Rishbeth & Garriott, 1969; Hernandez & Roble, 1976; Sipler & Biondi, 1978; Hernandez & Roble, 1979 ; Burnside *et al.*, 1981; Meriwether Jr *et al.*, 1983; Yagi & Dyson, 1985; Cogger *et al.*, 1985; Gurubaran, 1993; Fisher, 2013). However, since the wind measurements used in this study are obtained from observations of the 630.0 nm redline emssions, this section focusses mainly on this emission. In addition, 630.0 nm redline emissions has its peak within the thermosphere (an altitude of above 200 km during nighttime), where oxygen is the dominant species (Fisher, 2017). This emission is described by:

$$O(^1D) \rightarrow O(^3P) + hv, \tag{2.1}$$

where the photon (hv) emitted occurs at $\sim$ 630.0 nm with a rate coefficient of A_{630}. The excited oxygen is mainly produced through the dissociative recombination of O_2^+ (Hays *et al.*, 1978; Link & Cogger, 1988):

$$O_2^+ + e^- \rightarrow O(^1S,^1D,^3P) + O(^3P). \tag{2.2}$$

The main source of $O(^1D)$ is limited by the amount of O_2^+ reactant in this process. This is produced through an ion exchange with an ionised oxygen atom (Prölss, 2004):

$$O^+ + O_2 \rightarrow O + O_2^+. \tag{2.3}$$

However, this is not the only source of the excited oxygen, as it is also produced through the photodissociation of O_2, as follows (Hays *et al.*, 1978):

$$O_2 + hv \rightarrow O(^1D) + O(^3P). \tag{2.4}$$

Also, the reactions below cause the $O(^1D)$ to be depleted before it can successfully emit a photon:

$$
\begin{aligned}
O(^1D) + N_2 &\rightarrow O(^3P) + N_2 \\
O(^1D) + O_2 &\rightarrow O(^3P) + O_2 \\
O(^1D) + e^- &\rightarrow O(^3P) + e^-.
\end{aligned} \tag{2.5}
$$

Using the above equations, in addition with the laboratory-measured reaction rate coefficients (k), the volume emission rate (V_{630}) or intensity of the nighttime redline emission can be calculated by using the method described by Link & Cogger (1988), as follows:

$$
V_{630} = \frac{A_{630}\beta_1 k_1 [O_2][O^+]}{A_{1D} + k_3[N_2] + k_4[O_2] + k_5[e]}, \tag{2.6}
$$

where β_1 is the production efficiencies of $O(^1D)$, $N(^2D)$ from dissociative recombination of O_2^+ and NO^+, and A_{1D} accounts for the loss of $O(^1D)$ through spontaneous emission at multiple wavelengths (e.g., 630 nm) and the k_i ($i = 1, 2, ..., 5$) are the laboratory-measured reaction rate coefficients. Table 2.1 gives the values/equations for the production efficiencies and the various reaction coefficients, as well as their respective units. Equation 2.6 indicates that the production of a 630.0 nm photon is affected by plasma and neutral conditions in the thermosphere.

Table 2.1: The reaction rate coefficients for 630.0-nm emission after Link & Cogger (1988)

Coefficients	Value	Units
A_{630}	5.15×10^{-3}	1/s
A_{1D}	6.81×10^{-3}	1/s
β_1	1.1	
k_1	$3.23 \times 10^{-12} e^{3.72/(T_i/300) - 1.87/(T_i/300)^2}$	cm^3/s
k_3	$2.00 \times 10^{-11} e^{111.8/T_n}$	cm^3/s
k_4	$2.90 \times 10^{-11} e^{67.5/T_n}$	cm^3/s
k_5	$1.60 \times 10^{-12} T_e^{0.91}$	cm^3/s
T_i	Ion Temperature	K
T_e	Electron Temperature	K
T_n	Neutral Temperature	K

The redline emission peaks are typically located around 250 km, due to the balance between ion and neutral concentrations, in a similar manner as the ionosphere forms due to the balance between solar energy and particle density (Harding, 2017). As these two concentrations vary, so will the redline peak-altitude shift. For instance, if the plasma density decreases, it results in a decrease in electron density, dissociative recombination and O^+ ions leading to a decrease in airglow intensity of the redline emission. In addition, less airglow intensity could be due to a drop in neutral collision rate, due to an increase in the F layer peak height, resulting in a reduced ion exchange. Furthermore, less airglow intensity could be attributed to changes in the thermospheric neutral composition, causing an increase in the depletion of excited oxygen, as can be deduced from equation 2.5.

2.3 Thermospheric Winds

Thermospheric neutral wind is defined as the mean velocities of particles within a small parcel of air (Harding, 2017). Thermospheric winds, often written as $\mathbf{U}$, are represented as a vector (u, v, w), where u represents the zonal wind component (defined positive eastward), v represents the meridional wind component (defined positive northward) and w is the vertical component (defined positive upward). The major purpose for studying the thermospheric winds is the dynamo process in the thermosphere, through which the mechanical motion of the neutral particles creates an electrical forcing, instabilities, Joule heating and influences the dynamics of the ionospheric F-region (Rees, 1995; Heelis, 2004; Fisher, 2013). For example, Hanson & Moffett (1966) showed that neutral winds can account qualitatively for the day-to-night changes in the height and density of the ionospheric F2 peak, while Emmert *et al.* (2006) reported that neutral winds play an important role in the transport of ionospheric plasma along magnetic field lines. The alteration of ion densities in the F2 region that affects the rate at which the O^+ ions diffuse downward is caused by the component of the neutral wind along the magnetic field (Heelis, 2004). Martyn (1956) opines that the processes responsible for the vertical motion of the F2 layer are the drifts imposed by electrodynamic forces and the winds associated with the ionospheric electric current systems which are manifested as the daily magnetic variations at the ground. Thermospheric winds are responsible for the redistribution of heat, transferring energy from the warmer dayside toward the cooler nightside of the thermosphere. Also, inhomogeneities in ionisation densities produce drag effects on the neutral air motion that may lead to localised heating and associated circulation (Dickinson *et al.*, 1971; Gurubaran, 1993).

Thermospheric winds are generated primarily by pressure gradients due to changes in temperature that are mainly driven by solar heating (Brum *et al.*, 2012). In addition, other forces that contribute to thermospheric wind dynamics include, gravity, the Coriolis force, ion-neutral collisions, and the viscosity of air (Rishbeth & Garriott, 1969; Rishbeth, 1972). The pressure gradient forces zonal winds, causing an eastward wind during the early dusk that eventually shifts slightly westward in the early morning. Another factor that affects the direction and magnitude of the thermospheric wind depending on altitude and height, is the Earth's angular rotation about a vertical axis. This apparent force (as viewed from the rotating system) deflects all free-moving particles to the right of their path of motion in the northern hemisphere and to the left in the southern hemisphere. The ratio of the Coriolis force to ion drag determines the direction of the thermospheric wind. Ion drag caused by neutral-ion collision tends to slow down the neutral particles. The viscous drag force is a mechanism that converts the kinetic energy of moving objects into thermal energy. The force of gravity predominantly balances the vertical pressure gradient, so it causes minimal air movement. Since the gravitational force balances the vertical pressure gradient force, the neutral winds are assumed to be horizontal (Rishbeth, 1972). At night, the acceleration is slow, and it is affected by viscosity (Rishbeth & Garriott, 1969). Gravitational acceleration is caused by force per unit mass exerted on the atmosphere by the Earth's gravitational attraction. The kinematic viscosity plays a crucial role, particularly at high altitudes where the density drops off.

The equation for motion below describes the influences of these forces on the winds (Rishbeth, 2000):

$$\frac{d\mathbf{U}}{d\mathbf{t}} = \nabla\mathbf{P} - 2\Omega \times \mathbf{U} - \nu(\mathbf{U} - \mathbf{V}) + \frac{\mu}{\rho}\nabla^2\mathbf{U} + g, \tag{2.7}$$

where

$\frac{d\mathbf{U}}{d\mathbf{t}}$: acceleration,
$\mathbf{P}$: pressure gradient force per unit mass,
$2\Omega \times \mathbf{U}$: coriolis acceleration,
$\nu(\mathbf{U} - \mathbf{V})$: ion drag,
$\frac{\mu}{\rho}\nabla^2\mathbf{U}$: viscous drag,
g: gravity,
Ω: Earth's angular velocity,
ν: neutral-ion collision frequency,
$\mathbf{V}$: ion drift velocity,
μ: the dynamic viscosity,
ρ: neutral mass density,
$\frac{\mu}{\rho}$:the kinematic viscosity.

While these terms describe the circulation that occurs in the thermosphere, there are still many other drivers that cause spatial and temporal variation in the neutral winds, which hugely impact different interaction within the thermosphere-ionosphere. It is therefore crucial to make measurements of the winds to investigate further potential causes and factors influencing them.

Direct measurement of thermospheric winds are done using a Fabry-Perot interferometer (FPI). Indirect measurements of the thermospheric winds are done using measurements of the maximum height of the ionospheric F2 layer (hmF2) obtained from instruments such as ionosondes and incoherent scatter radars. Where there is a lack of instrumentation, models such as the Horizontal Wind Model (HWM) (e.g. Drob *et al.*, 2015), and Thermosphere Ionosphere Electrodynamic General Circulation Model (TIE-GCM) (Richmond *et al.*, 1992) are used. While there are various methods used to derive thermospheric winds from ionospheric measurements, this work focusses on the method developed by Rishbeth (1972), which will be described in the next chapter. In addition, wind models developed by Drob *et al.* (2015) and Dandenault (2018) are also used in this study for validation purposes and will be discussed in detail in chapters 4 and 5.

2.4 Atmospheric Tides

Atmospheric tides are global-scale oscillations that arise primarily as a result of solar heat, wind or lunar influences (Schunk & Nagy, 2009). The main source of atmospheric tides is heating associated with the absorption of solar radiation by water vapor and ozone in the troposphere. However, they can also be excited in situ in the thermosphere by the absorption of local thermospheric UV and EUV solar radiation and by high-latitude ion-drag momentum coupling (Parish *et al.*, 1990). Theoretical descriptions of atmospheric tides have been presented by Chapman & Lindzen (1970), Forbes (1982), Forbes *et al.* (2008), and Wang *et al.* (2016)). Atmospheric tides have also been derived from different observations (e.g. Amayenc & Reddy, 1972; Portnyagin *et al.*, 1993; Merzlyakov *et al.*, 2009; Oberheide *et al.*, 2002; Oberheide *et al.*, 2011). There is considerable theoretical and experimental evidence that neutral motions in the thermosphere consists predominantly of tidal periods and a steady or slowly varying component (Amayenc & Reddy, 1972).

Atmospheric tides accelerate the mean flow and heat of the atmosphere, and modulate atmospheric gravity waves. Park *et al.* (2010) presented direct evidence that the winds associated with non-migrating tides have a direct impact on the F-region ionosphere, in addition to any effect they may have on the plasma density. In addition, England (2012) presented three mechanisms by which non-migrating tides may affect the ionospheric F-region density: (1) advection of the plasma along the geomagnetic field lines at F-region altitudes; (2) electrodynamic coupling to the E-region dynamo; (3) modification of the photochemical equilibrium. The study of atmospheric tides has a long and fascinating history, beginning with many years of barometric observations and in the modern sense, with the development of the classical atmospheric tidal theory (see the review by Lindzen & Chapman, 1969). Atmospheric tides can be classified into two main categories:

- Solar atmospheric tides: are persistent and global variations in atmospheric parameters, such as neutral winds, with periods that are some integer fraction of a solar day (Oberheide *et al.*, 2015). Solar tides have many modes that are excited, with the most observed being the diurnal, semidiurnal, and terdiurnal harmonics with periods of 24, 12, and 8 hours, respectively, while the 6-hour tide is observed occasionally. At approximately 250 km altitude, the solar-driven diurnal tide dominates, while between 100 and 250 km both diurnal and semi-diurnal components are present (Schunk & Nagy, 2009).

- Lunar atmospheric tides: are tides with periods which correspond to the period of the full moon to new moon cycle, i.e. the diurnal tide has a period of 24.8 hours while the period of the semi-diurnal tide is 12.4 hours. The influences of these tides are largest at full and new moon (Haurwitz, 1964; Paulino *et al.*, 2013).

Solar and lunar tides are either migrating or non-migrating tides. The migrating tides are sun-synchronous tides that propagate westward and are constant across different longitudes when observed at the same local time. They are either gravitationally or thermally induced because the tidal perturbations move westward relative to a fixed location on the rotating Earth (Oberheide *et al.*, 2002; Schunk & Nagy, 2009). Non-migrating tides are sun-synchronous tides that can create longitudinal variations in the ionosphere and can affect the plasma density. Their apparent motion is either slower or faster than the Sun due to linear interaction with stationary planetary waves (England, 2012).

The following descriptions and derivations follow those contained in Holton (1975) and Forbes *et al.* (1995). Navier-Stokes equations are used to form the mathematical basis for atmospheric tides. These equations are linearised to describe the zonal mean state and perturbations from this mean state of the background atmosphere. On the assumption that the background atmosphere is horizontally stratified (i.e. the zonal mean winds are zero) and isothermal background atmosphere. By further simplification, the linearised equations for perturbations in a spherical isothermal atmosphere are:

$$\frac{\partial u}{\partial t} - 2\Omega v sin\theta + \frac{1}{acos\theta}\frac{\partial \Phi}{\partial \lambda} = 0, \tag{2.8}$$

$$\frac{\partial u}{\partial t} + 2\Omega u sin\theta + \frac{1}{a}\frac{\partial \Phi}{\partial \lambda} = 0, \tag{2.9}$$

$$\frac{\partial}{\partial t}\Phi_z + N^2\omega = \frac{kJ}{H}, \tag{2.10}$$

$$\frac{1}{\rho_0}\frac{\partial}{\partial z}(\rho_0\omega) + \left[\frac{\partial u}{\partial \lambda} + \frac{\partial}{\partial \theta}vcos\theta\right]\frac{1}{acos\theta} = 0, \tag{2.11}$$

where

u	eastward velocity
v	northward velocity
w	upward velocity
Φ	perturbation geopotential
N^2	buoyancy frequency square = kg/H
Ω	angular velocity of Earth
ρ_0	basic state density, $\propto e^{-z/H}$
z	altitude
λ	longitude
θ	latitude
k	$R/c_p \approx 2/7$
J	heating per unit mass
a	radius of Earth
g	acceleration due to gravity
H	constant scale height
t	time

Assuming that the perturbations consist of longitudinally propagating waves of zonal wave number s (defined to give the maxima n of sinusoidal oscillation in longitude), and frequency σ, then the plane wave solution will be described by the following equation (Forbes *et al.*, 1995):

$$\{u, v, w, \Phi\} = \{\hat{u}, \hat{v}, \hat{w}, \hat{\Phi}\}exp\left[i(s\lambda - \sigma t)\right]. \tag{2.12}$$

The phase term $(s\lambda - \sigma t)$ is chosen so that the positive (negative) values for σ correspond to eastward (westward) propagating waves, i.e., the real part of equation 2.12 is cos $(s\lambda - \sigma t)$ and the crest of the wave occurs when $\lambda = \sigma t/s$. Substituting equation 2.12 into equations $2.8 - 2.11$ eliminates derivatives with respect to t and λ, and using a single second-order differential equation for Ω in z and θ, gives a separable solution as follows:

$$\hat{x} = \sum_n \Theta_n(\theta)G_n(z), \tag{2.13}$$

where $\hat{x} \in \{\hat{u}, \hat{v}, \hat{w}, \hat{\Phi}\}$, $\{\Theta_n\}$ is a complete orthogonal set. From equations (2.8), (2.9) and (2.13) expressions for the velocity components in terms of Θ_n and G_n can be derived:

$$\hat{u} = \frac{\sigma}{4\Omega^2 a} \sum_n L_n(\theta) G_n(z), \tag{2.14}$$

$$\hat{v} = \frac{-i\sigma}{4\Omega^2 a} \sum_n M_n(\theta) G_n(z), \tag{2.15}$$

where

$$L_n = \frac{1}{(\frac{\sigma}{2\Omega})^2 - sin^2\theta} \left[\frac{s}{cos(\theta)} + \frac{sin(\theta)}{\frac{\sigma}{2\Omega}} \frac{d}{d\theta} \right] \Theta_n, \tag{2.16}$$

$$M_n = \frac{1}{(\frac{\sigma}{2\Omega})^2 - sin^2\theta} \left[\frac{s\, tan(\theta)}{cos(\theta)} + \frac{sin(\theta)}{\frac{\sigma}{2\Omega}} \frac{d}{d\theta} \right] \Theta_n. \tag{2.17}$$

The expression below is a consequence of separation, which can be rearranged to describe how tides propagate vertically, defining $G_n^1 = G_n \rho_0^{0.5} N^{-1}$, taking $N^2 = kg/H$ for an isothermal atmosphere $H = 7.5$ km, and $x = z/H$ that results in the canonical form for the vertical structure equation:

$$\frac{d^2 G_n'}{den} + \left[\frac{kH}{h_n} - \frac{1}{4} \right] G_n^{'} = -\frac{\rho_0^{-1/2}}{i\sigma N} \frac{d}{dx} (\rho_0 J_n), \tag{2.18}$$

where h_n is the separation constant or equivalent dept and J_n is the vertical profile heating. Considering only the θ dependent part of this equation, to obtain a Laplaces tidal equation (Laplace, 1799):

$$\frac{d}{d\mu} \left[\frac{(1-\mu^2)}{(f^2-\mu^2)} \frac{d\Theta_n}{d\mu} \right] - \frac{1}{(f^2-\mu^2)} \left[\frac{s}{f} \frac{(f^2+\mu^2)}{(f^2-\mu^2)} + \frac{s^2}{1-\mu^2} \right] \Theta_n + \epsilon_n \Theta_n = 0, \tag{2.19}$$

where $\mu = sin(\theta)$ and $\epsilon_n = (2\Omega a)^2 / gh_n$. To emphasise the explicit dependence on s, σ and ϵ_n this Laplace equation may also be written as

$$F_{s,\sigma}(\Theta_n^{s,\sigma}) = \epsilon_n^{s,\sigma} \Theta_n^{s,\sigma}. \tag{2.20}$$

For each of s and σ, there exist sets of ϵ_n and Θ_n (the eigenfunctions or Hough function of the Laplace tidal equation) that satisfy equation 2.20 and boundary conditions are located at the poles ($\mu = \pm 1$) (Hough, 1897; Hough, 1898). The solution to the Laplace tidal equation was pioneered by Hough (1897) and Hough (1898) in terms of associated Legendre functions, which are the latitudinal basis functions for waves propagating in spherical coordinates. Groves (1981) provides a detailed explanation of the Hough function and its use in solving the Laplace equation.

When describing tides in the mesosphere and lower thermosphere, the above method suffices and describes tides well. However, in the thermosphere, once the mean zonal winds are included, these equations are no longer separable into vertical and latitudinal components, hence other methods for solving the tidal equations, such as as numerical methods, would be employed (Oberheide *et al.*, 2015; Chu, 2019). The horizontal variation of the atmospheric tides (u and v) can be obtained by rearranging equation (2.12), using $\sigma = -n\Omega$, and is generalised by including a phase term (Chu, 2019):

$$A_{n,s}cos(n\Omega t - s\lambda - \phi_{n,s}), \tag{2.21}$$

where t is universal time (days), Ω is the rotation of the Earth which is equal to 2π (rads/day), λ is the longitude, n denotes a subharmonic of the solar/lunar day (e.g. n = 1 for diurnal, n = 2 for semidiurnal, n = 3 for terdiurnal, etc.), $A_{n,s}$ is the amplitude, $\phi_{n,s}$ is the phase, which is defined as the universal time when the maximum passes the zero degree longitude, s is the zonal wave-number (Forbes *et al.*, 2006). Equation (2.21) can be slightly modified to calculate phase, amplitude and background tidal winds for different tidal harmonics:

$$V = A_i cos(\omega_i t - \phi_n) + B, \tag{2.22}$$

where ω_i is the diurnal, semidiurnal and terdiurnal tide, and B is the non-zero mean signal (Amayenc & Reddy, 1972; Fisher *et al.*, 2002; Zhang *et al.*, 2006; Forbes, 2007; Liu *et al.*, 2014).

2.5 Summary

This chapter briefly described the thermosphere and ionosphere, and gave a brief overview of airglow, thermospheric winds and atmospheric tides. The next chapter discusses different ground-based instruments that are used for measuring thermospheric winds, and the parameters obtained from them, and data processing methods.

Chapter 3

Instrumentation and data analysis

This chapter describes the basic principles of a Fabry-Perot interferometer, including the instrument design, operation, and data processing methodology. Also covered in this chapter is the principle of ionospheric sounding with ionosondes, including interpretation of ionograms and ionosonde derived meridional neutral wind. Lastly, data analysis methods and space weather indices pertaining to this project are described.

3.1 Fabry Perot interferometer (FPI)

The FPI is a widely-used optical instrument for probing the thermosphere to measure thermospheric neutral winds. The first FPI to observe the aurora was made by Babcock (1923). About fifty years later Hernandez & Roble (1976), from the Fritz Peak Observatory, Colorado (39.9° N, 105.5° W), recorded the first measurements of thermospheric winds using the 630.0 nm emission. There have been several FPI deployments across the globe which made it possible to study neutral winds. FPIs were also used for other applications, such as laser cavity development, optical computing and in the telecommunications industry (Bamgboye & McClure, 1982, Spencer *et al.*, 1982; Sahai *et al.*, 1992; McLandress *et al.*, 1996; Emmert *et al.*, 2002; Fejer *et al.*, 2002; Meriwether, 2006; Emmert *et al.*, 2006; Häusler *et al.*, 2007; Brum *et al.*, 2012; Yu *et al.*, 2014; Fisher *et al.*, 2015; Tesema *et al.*, 2017; Harding, 2017; Grawe *et al.*, 2019). This research focuses on obtaining high resolution spectral measurements of the redline emission at 630.0 nm. This research project will use the FPI's high resolution spectral measurements of the nighttime redline emission at 630.0 nm, which naturally occurs at an altitude of approximately 250 km (Fisher, 2017). This FPI is located at Sutherland, South Africa (32.2°S, 20.48°E; geomagnetic latitude: 40.7°S), as shown in Figure 3.1 (denoted by a green plus sign). From these spectral measurements, neutral winds were extracted and evaluated.

3.1.1 Theory of FPI

An etalon is an essential part of the FPI instrument and is responsible for creating a fringe pattern that is analysed to obtain neutral winds and temperatures. The etalon is made up

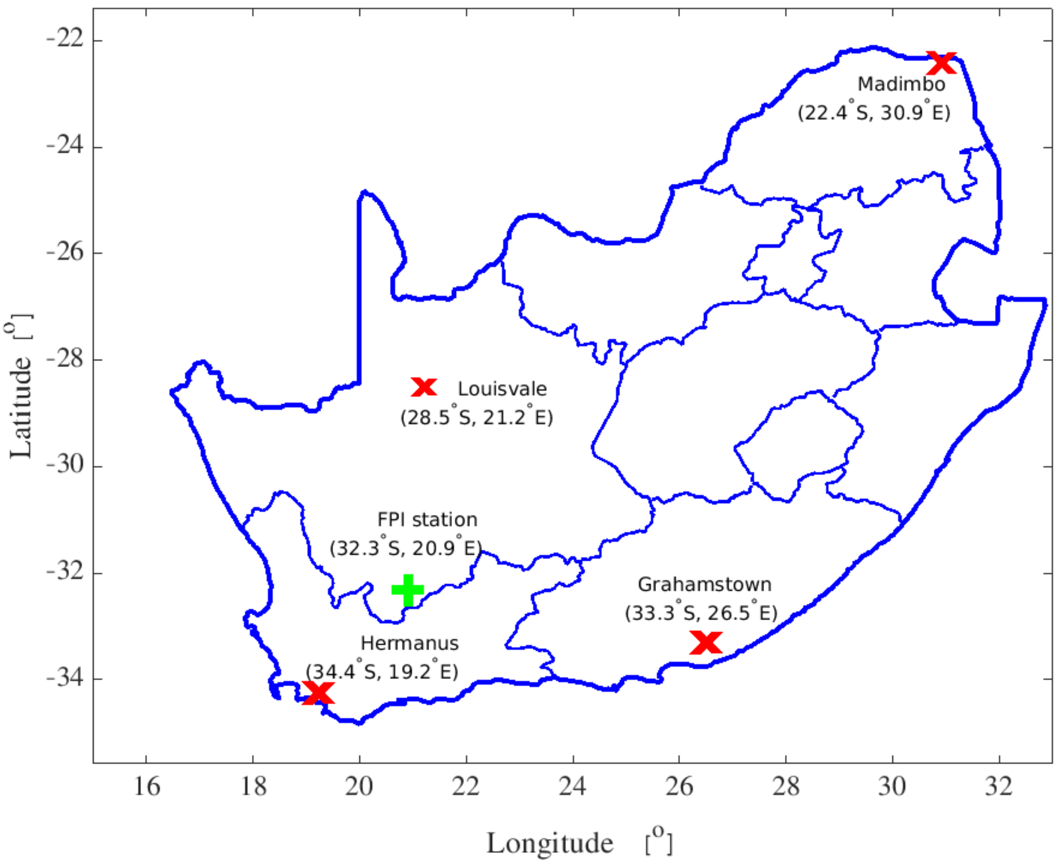

Figure 3.1: South African map showing four locations in the South African network of ionosondes indicated by red crosses. The location of the FPI is indicated by a green plus sign.

of two parallel partially reflective pieces of glass separated by distance d, and an n being the order of interference, as illustrated in Figure 3.2. When light of wavelength λ is incident on the top of the etalon, at an angle θ, it undergoes multiple reflections such that the transmitted and reflected rays interfere to form circular fringes. The optical path difference between successive reflections creates a phase lag, ϕ, as given by Ranade (1950) and Vaughan (1989):

$$\phi = \left(\frac{2\pi}{\lambda}\right) 2ndcos(\theta). \tag{3.1}$$

The electric field amplitude (E) and phase (ϕ) accumulation for each transmitted ray are shown in Figure 3.2. Starting from the beginning, after the incident light has passed through the first plate but before it hits the second, and after this ray has reflected off the bottom and top plates again, the electric field amplitudes are obtained respectively: $E_1 = tE_{in}$, $E_2 = r^2 tE_{in} e^t E_i e^{-j\phi} \ldots$ $E_5 r^8 tE_{in} e^t E_i e^{-j4\phi}$, where t is the transmission coefficient and r is the reflection coefficient. The total intensity of the transmitted electric field (E_{total}) can be calculated by using simple geometric optics and summation of all the transmitted rays that emerge from between the two plates (etalon), i.e.,

$$\begin{aligned} E_{total} &= \sum E_{transmitted} \\ &= tE_1 + tE_2 + tE_3 + tE_4 + \ldots \\ &= t^2 E_{in}(1 + r^2 e^{-j\phi} + r^4 e^{-j2\phi} + \ldots). \end{aligned} \tag{3.2}$$

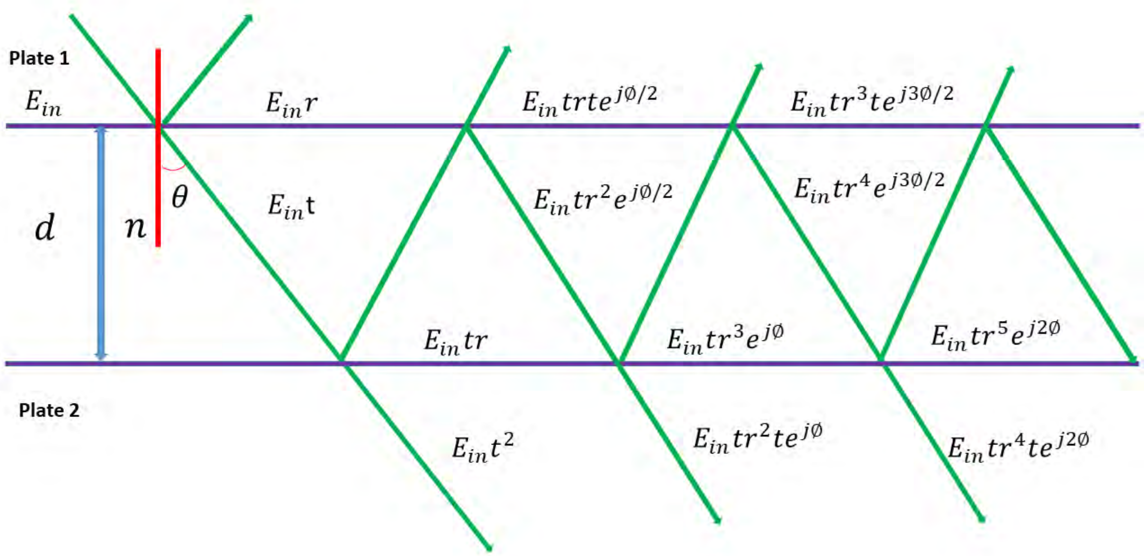

Figure 3.2: Light passing through the etalon of a Fabry-Perot interferometer, adapted from Ranade (1950).

Assuming that the etalon is infinitely long and that both t and r are identical such that $T = t^2$ and $R = r^2$, where T is the transmittance and R is the reflectance, an infinite geometric Taylor series can be used to simplify this expression (Ranade, 1950; Vaughan, 1989; Fisher, 2013):

$$\begin{aligned} E_{total} &= \frac{t^2 E_{in}}{(1 - r^2 e^{-j\phi})} \\ &= \frac{TE_{in}}{(1 - R^2 e^{-j\phi})}. \end{aligned} \tag{3.3}$$

The intensity of the light passing through the etalon is equivalent to $|E_{total}|^2$, i.e., $I = |E_{total}|^2$, such that:

$$
\begin{aligned}
I = |E_{total}|^2 &= \frac{T^2|E_{in}|^2}{\left(1 - R^2 e^{-j\phi}\right)^2} \\
&= \frac{T^2|E_{in}|^2}{\left(1 - R^2 e^{-j\phi}\right)\left(1 - R^2 e^{-j\phi}\right)} \\
&= \frac{T^2|E_{in}|^2}{1 + R^2 - 2Rcos(\phi)}.
\end{aligned}
\tag{3.4}
$$

Letting $cos(\phi) = \left(1 - sin^2(\phi/2)\right)^2$, then the above equation becomes:

$$
\begin{aligned}
I &= \frac{T^2|E_{in}|^2}{1 + R^2 - 2R\left(1 - 2sin^2(\frac{\phi}{2})\right)} \\
&= \frac{T^2|E_{in}|^2}{(1 - R^2 + 4Rsin^2(\frac{\phi}{2})}.
\end{aligned}
\tag{3.5}
$$

Since $R + T = 1$, the intensity can therefore be simplified to:

$$
I = \frac{|E_{in}|^2}{1 + \frac{4R}{(1-R)^2} sin^2\left(\frac{2\pi nd}{\lambda} cos(\theta)\right)}. \tag{3.6}
$$

The term $4R/(1 - R)^2$ is known as the coefficient of finesse and is donated by F such that an Airy function can be obtained as follows (Hernandez, 1982):

$$
A(\theta, \phi) = \frac{I}{1 + Fsin^2\left(\dfrac{2\pi nd}{\lambda} cos(\theta)\right)}. \tag{3.7}
$$

The phase term $\frac{2\pi nd}{\lambda} cos(\theta)$ is one of the most important terms. It is crucial because it is susceptible to large changes in wavelength, order of interference, etalon gap, or angle. It is its sensitivity to small changes in wavelength that allows for monitoring changes in Doppler shifts caused by winds. The Free Spectral Range, i.e., FSR ($\Delta\lambda$), is the maximum change in wavelength that can be unambiguously resolved, or, the shift in wavelength resulting in a phase shift of π (Chu, 2019). The FSR is another important parameter of the Airy function and categorises the resolving power of the system. It can be obtained by taking the derivative of the phase term with respect to λ and setting it equal to π, i.e.

$$
\Delta\lambda 2\pi nd\lambda^{-2} cos(\theta) = \pi, \tag{3.8}
$$

$$
\Delta\lambda = \frac{\lambda^2}{2ndcos(\theta)}. \tag{3.9}
$$

In order to obtain a significant result, at least one FSR must be captured, and for our application the FSR must be large enough so that consecutive fringes do not overlap.

3.1.2 Design of the FPI

The FPI used in this project was designed and built by the University of Illinois at Urbana-Champaign. It consists of a SkyScanner, a filter, a charge-coupled device (CCD), a lens, and an etalon as shown in Figure 3.3. The etalon is composed of two partially reflective surfaces separated by an air gap of 15 mm and reflectivity of $\sim$77%. The properties of this gap determines the phase offset of the reflected copies of the light that enters the etalon. The diameter of the etalon may vary depending on the system, but the etalon in the FPI used in this project has a diameter of 7 cm. The interference pattern created by the etalon is then imaged by using an objective lens onto a 13.3×13.3 mm Andor CCD. This CCD has 1024×1024 pixels (binned to 512×512) and is thermoelectrically cooled to below $-60°C$ to reduce the effects of dark current and read out noise. A diffuser box was used to create an approximately uniform calibration source and to image the output of the diffuser box, by means of approximation of the laser as a δ source to enable characterisation of the system function. Doing this, it allows most of the fluctuations in the etalon gap and other instrument parameters that occur throughout the data taking process to be tracked. Inspite of being outside the passband of the interference filter, the laser light is bright enough to pass through the filter and provide a usable fringe pattern. When the laser is not being imaged by the FPI, a USB-controlled shutter is closed, to minimise possible contamination to sky observations.

The light enters the system through the dual-mirror-SkyScanner, and passes through a narrowband (1.0 nm full width half maximum) interference filter centred at 630.0 nm with $\sim$ 55% transmission placed in the optical path before the etalon to isolate the redline emission from other background emissions. As soon as the desired wavelength has been isolated, the light enters the etalon to create the interference pattern. This system is driven by a smart motor on each axis. It is directly above the optics and allows observations of the sky in any direction by rotating in the elevation and the azimuth planes. The FPI looks at a 1.8° field of view at an elevation angle of 45°, set up to observe in the zenith direction first, followed by each of the four cardinal directions (north, east, south, and west) at the same elevation angle. This is regarded as "cardinal mode" and allows both meridional and zonal components to be extracted with few assumptions (Makela *et al.*, 2013; Harding *et al.*, 2014; Fisher *et al.*, 2015). Each observation of the sky is followed by an observation of a frequency-stabilised HeNe laser to monitor the parameters of the instrument.

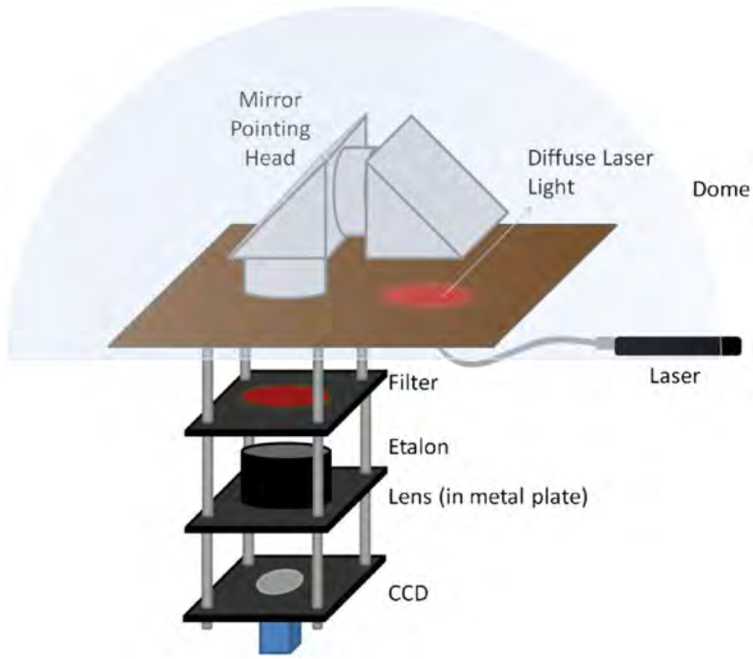

Figure 3.3: Configuration of FPI in Sutherland, adapted from Grawe *et al.* (2019).

Since all that is obtained from sky measurements is a fringe pattern, it is essential to have external sensors to monitor viewing conditions. A roof-mounted Boltwood Cloud Sensor II was used to compare the sky temperature (infrared reading in the 8–14 μm wavelength) and the ambient temperature. When the sky temperature is subtracted from the ambient temperature and the result is less than (more negative than) a threshold, which is often dependent on site and season, the sky is declared to be clear. Similarly, if the difference between the sky temperature and the ambient temperature is larger than the threshold, this indicates the presence of clouds. In general, most systems use a threshold of -10°C to -22°C as the cutoff (Fisher *et al.*, 2015), but a threshold of -20°C was used for this instrument.

3.1.3 Operation of FPI

Each night the instrument will automatically power on and begin to take data after sunset. Throughout the night until dawn, the SkyScanner will turn to point either at the sky in one of the four cardinal directions, a point at zenith or at the laser to take a calibration fringe. For a sky fringe in the cardinal directions, the SkyScanner azimuth mirror will rotate to the correct cardinal direction and the zenith mirror will turn to an angle of 45°. A zenith measurement is also made as part of this cycle by rotating to any azimuth and setting the zenith angle to 0°. Once the cardinal directions and the zenith have been recorded, the cycle repeats itself until data collection stops for the night (Makela *et al.*, 2012; Fisher, 2013; Fisher *et al.*, 2015; Fisher, 2017; Chu, 2019). Then a 1–10 minutes exposure is taken (with length depending on emission intensity in the prior sky position). For a laser image, the light from the HeNe laser is scattered in the scattering chamber on top of the instrument plate, from which it can enter the optical path via the SkyScanner to provide a uniform calibration source. Laser exposures are fixed at 30 seconds since the laser intensity is essentially constant. For this project the light from the scattering chamber serves as the calibration source for the FPI, used in data processing. At the end of the night, the instrument will automatically stop collecting data and the data will be sent to the University of Illinois server for processing. For a quick look at processed data, all data is displayed on the calendar at `http://airglow.ece.illinois.edu/Data/Calendar` under the abbreviation SAO.

3.1.4 FPI data processing

This section presents FPI data processing. More details can be found in Harding *et al.* (2014). Data processing begins by analysing the laser images as presented in Figure 3.4 to estimate the instrument function, given by equation 3.7. For a narrow field FPI such as our instrument, θ is given by the relation below:

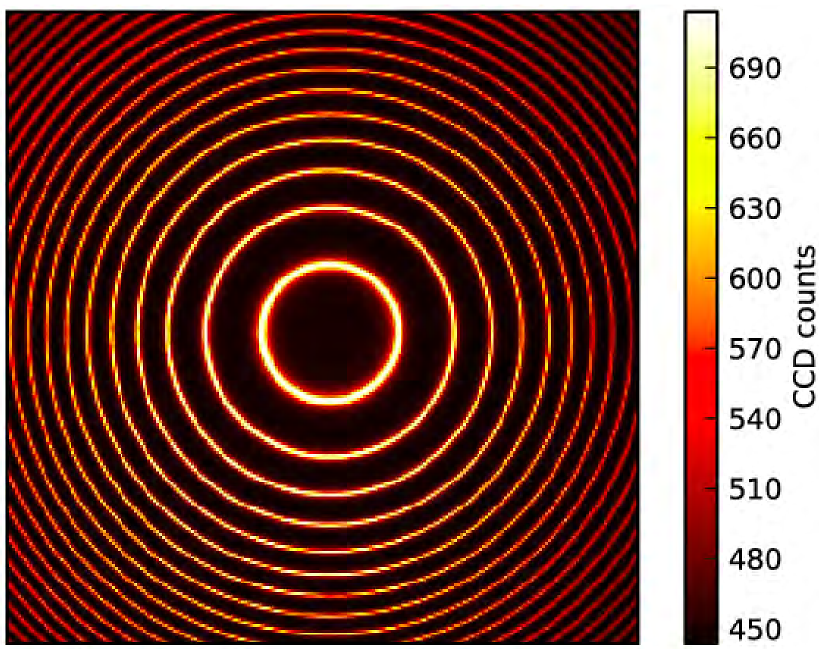

Figure 3.4: Example of FPI laser calibration adapted from Harding *et al.* (2014).

$$\theta = tan^{-1}(\alpha r), \tag{3.10}$$

where α is a constant that will be estimated from the laser calibration fringe image, and r is the radius. The intensity (I) can be replaced with a quadratic falloff term to better characterise the instrument function, and is given by:

$$I = I_o \left(1 + I_1 \left(\frac{r}{r_{max}}\right) + I_2 \left(\frac{r}{r_{max}}\right)^2\right), \tag{3.11}$$

where r_{max} is the maximum value of r on the CCD. Substituting the value of F, equation 3.10 and equation 3.11 into equation 3.7, the Airy function becomes

$$A(\theta, \lambda) = I_o \frac{1 + I1 \left(\frac{r}{r_{max}}\right) + I_2 \left(\frac{r}{r_{max}}\right)^2}{1 + \frac{4R}{(1-R)^2} sin^2 \left(\frac{2\pi nd}{\lambda}\right) cos(tan^{-1}(\alpha r))}. \tag{3.12}$$

Applying a Gaussian blur radially to the equation above, the Airy function becomes

$$\tilde{A}(r, \lambda) = I_o \int_a^b \frac{1 + I_1 \left(\frac{s}{r_{max}}\right) + I_2 \left(\frac{s}{r_{max}}\right)^2 e^{-\frac{(s-r)^2}{\sigma(r)^2}}}{1 + \frac{4R}{(1-R)^2} sin^2 \left(\frac{2\pi}{\lambda} \frac{nd}{\sqrt{(\alpha a)^2 + 1}}\right) \sqrt{2\pi\sigma(r)}} ds, \tag{3.13}$$

where $\sigma(r) = \sigma_o + \sigma_1 sin\left(\pi \frac{r}{r_m}\right) + \sigma_2 cos\left(\pi \frac{r}{r_m}\right)$ is the blurring width. To represent the entire laser fringe pattern, the relation below is used

$$S(r) = \int_{-\infty}^{+\infty} \tilde{A}(r, \lambda) Y(\lambda) d\lambda + B, \tag{3.14}$$

where B is the CCD counts due to the bias on the CCD, and $Y(\lambda)$ is based on the light source being observed. For the laser, $Y(\lambda) = \delta(\lambda - \lambda_{laser})$ which leads to the forward model for the laser images, expressed by,

$$S(r) = \tilde{A}(r, \lambda_{laser}) + B. \tag{3.15}$$

In order to extract the instrument parameters from the fringe pattern for each of the images, the Airy function was permitted to vary systematically and the Levenberg-Marquardt inversion algorithm was used to fit the laser fringe pattern to the laser data. All laser images were fitted and the extracted parameters were then interpolated in time. This process is necessary because it accounts for the system variation that occurs during the time between two laser images and to have close approximations of the system parameters at any time throughout the night. After obtaining the system parameters, the sky fringe images were then processed by annulus summation using the centre from the laser images. Using the interpolated laser parameters at the time of the sky fringe image, another Levenberg-Marquardt was performed on the inversion equation 3.14 with

$$Y(\lambda) = Y_{bg} + Y_{lin}\ exp\left(-\frac{1}{2}\left(\frac{(\lambda - \lambda_c)^2}{\Delta\lambda}\right)\right), \tag{3.16}$$

a thermally-broadened and Doppler-shifted Gaussian. In equation 3.16, Y_{bg} is the background sky emission, Y_{lin} is the intensity of the airglow emission, λ_c is its centre wavelength, and $\Delta\lambda$ is the Doppler. The line-of-sight (LOS) wind velocities and temperatures are obtained through Doppler shift and doppler broadening, respectively:

$$\begin{aligned} v &= \left(\frac{\lambda_c}{\lambda_o} - 1\right) c, \\ T &= \frac{m}{k}\left(\frac{c\Delta\lambda}{\lambda}\right)^2, \end{aligned} \tag{3.17}$$

where v is the line-of-sight velocity, λ_c is the emission centre wavelength, c is the speed of light, k is the Boltzmann constant, m is the mass of the emitting species, T is the temperature, λ_o is the nominal centre wavelength which is 630.0 nm. Figure 3.5 presents a sample of how winds affect a single fringe. Each estimate of wind and temperature is followed by an associated uncertainty as an output of the Levenberg-Marquardt inversion.

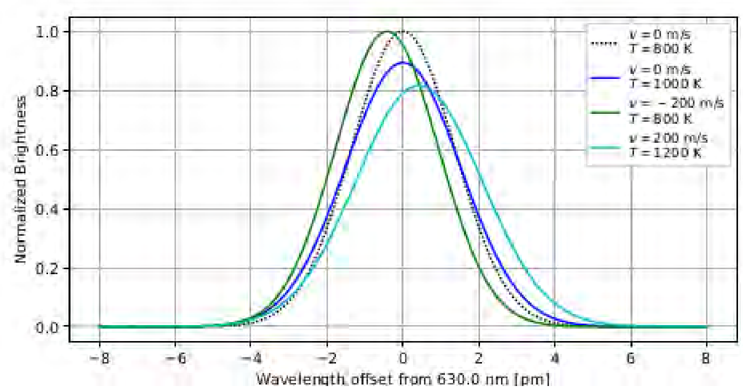

Figure 3.5: Example of 630.0-nm illustrating the effect of various LOS winds (v), and temperatures (T) on position and shape of the measured sky spectra. Adapted from Harding (2017).

Laser and sky fringe image processing, is followed by Doppler referencing, which is necessary as the exact laser or emission wavelength is unknown, meaning the reference location of zero wind is unknown. One method is the Doppler referencing method (often referred to as the zenith reference), which assumes zero vertical wind. It uses the zenith-looking measurements (*zenith reference*) to determine the wavelength shift of zero wind, which is then applied to all other cardinal measurements. Another method is the *laser reference* which assumes that the mean vertical wind throughout the night is approximately zero (Hernandez, 1982).

The next step is to convert line of sight winds to cardinal winds, using the method described by Makela *et al.* (2012). These winds will already have had a Doppler reference (calculated by either zenith or laser referencing, depending on the manner in which the data will be processed) subtracted off. To convert to cardinal winds, the winds are rotated into a geographic coordinate frame using:

$$LOS_{direc} = wcos(\alpha) + [vcos(\theta) + usin(\theta)]\, sin(\alpha) + \beta, \tag{3.18}$$

where LOS_{direc} is the given LOS wind, w is the vertical wind, v is the meridional wind (defined positive north), u is the zonal wind (defined positive eastward), α is the zenith angle, θ is the azimuth angle and β is the velocity offset due to an unknown Doppler reference. Since a laser is used to characterise the instrument function, any zenith LOS measurements ($\alpha = 90°$) are equal to the vertical wind, or

$$\tilde{w} = LOS_{zenith} - \beta_{zenith}. \tag{3.19}$$

The zonal and meridional winds can be therefore calculated by

$$\begin{aligned} u_{direc} &= \frac{LOS_{direc} - \tilde{w}cos(\alpha) - \beta_{direc}}{sin(\theta)sin(\alpha)} \; where\ direc \in \{East, West\}, \\ v_{direc} &= \frac{LOS_{direc} - \tilde{w}cos(\alpha) - \beta_{direc}}{cos(\theta)sin(\alpha)} \; where\ direc \in \{North, South\}. \end{aligned} \tag{3.20}$$

Note that the $\tilde{w}$ shown here is an interpolated vertical wind, which ensures that the vertical wind is used as at the time of the LOS measurement. Since the zonal (meridional) wind is defined as eastward (northward), the resultant $u(v)$ for westward (southward) should be multiplied by -1 to maintain that convention. The angles for azimuth and elevation for each direction are listed in Table 3.1

Table 3.1: Azimuth and elevation angles for each cardinal direction

Direction	θ	α
east	90°	45°
west	270°	45°
north	0°	45°
south	180°	45°

The uncertainties must also be converted from LOS to cardinal using:

$$\sigma_{direc} = \sqrt{\sigma^2_{LOS,direc} + \sigma^2_w}. \tag{3.21}$$

For wind data there are automated quality flags, either a 0, 1, or 2. A 2 indicates that the measurements should not be used because of large uncertainties, clouds or something else that made the measurements look suspicious. A 1 indicates that there are possible sources of bias and data should be used with caution. For example, contamination from other emissions particularly the OH emissions at ∼630.7 nm and ∼629.8 nm. When the redline 630.0 nm emission gets particularly dim, there is potential for OH to become visible in the fringe pattern and disrupt the inversion algorithm. If the emission brightness is detected to go below the defined threshold (−20°C), then the measurement's quality flag is raised to 1, there are possible sources of bias in the measurements. And lastly a 0 indicates that the data are reasonable measurements. While this quality flag system detects many potential bad data points, attention is also paid to instrument conditions, uncertainties, fit chi square values, etc., during the analysis and before using the results. An example of the output of the complete processing code run on data from a single night is displayed in Figure 3.6.

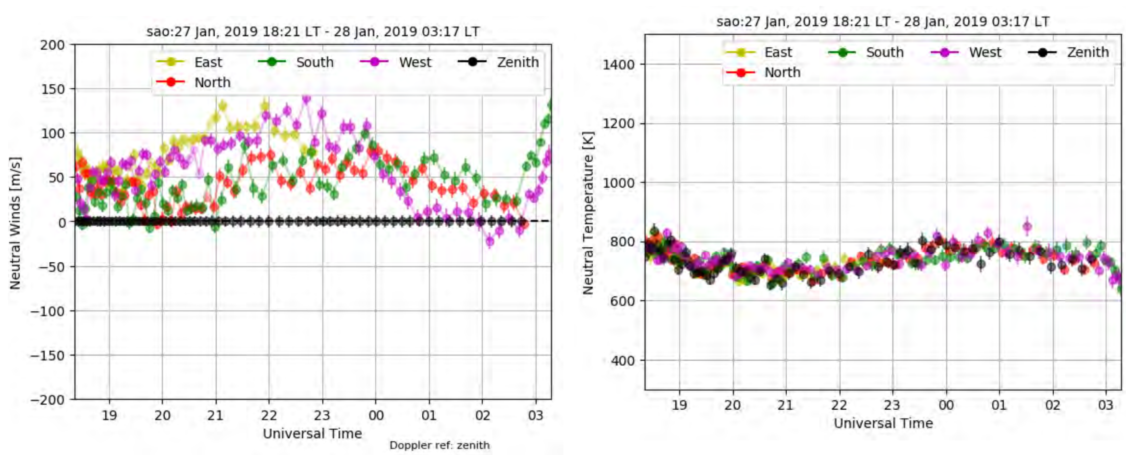

Figure 3.6: Example of neutral wind estimates and temperatures obtained after applying the standard processing algorithm on observations on 27 January 2019 over Sutherland, South Africa (http://airglow.ece.illinois.edu/Data/SiteDisplayData).

A cloud sensor has been co-located with the FPI to provide information on the viewing conditions. The sensor measures the difference between the sky and ambient temperatures, which is then used as cloud cover indicator. When available, this information was used to remove observations made when the sky was cloudy during the quality check process. The empirically chosen cutoff temperature for detecting cloud cover is -20°C and higher (Fisher *et al.*, 2015). To ensure only good quality data for quiet geomagnetic conditions are used in the analysis, wind values outside the range of -200–200 m/s were considered as unrealistic and therefore discarded. Also wind measurements with uncertainties greater than 25 m/s were discarded. In addition any wind measurements associated with temperature measurements in the range of 600–1400 K or with uncertainty of more than 50 K were treated as suspicious and therefore also not used. Finally the measurements are sorted and binned into 30 minutes local time bins for each month for winds measurements from each viewing direction in order to combine wind data from different nights. Any small spatial and temporal gradients will be removed in this binning process.

3.2 Ionosonde

An ionosonde is a vertical sounding radar system that measures ionospheric properties, or bottom-side ionosphere, by vertical transmission and reception of radio wave signals at frequencies between $\sim$ 0.5 and 30 MHz. It is a type of HF radar that is most frequently used today as an ionospheric sounding device and is one of the most important techniques for the global investigation of ionospheric structures. An ionosonde is either a bistatic radar system, which means that the transmitting antenna and the receiving antenna are separated from each other and with two separate energy paths, or mono-static, where the transmitting antenna and the receiving antennas are located together (Chen , 1984; McNamara, 1991; Hunsucker & Hargreaves, 2007).

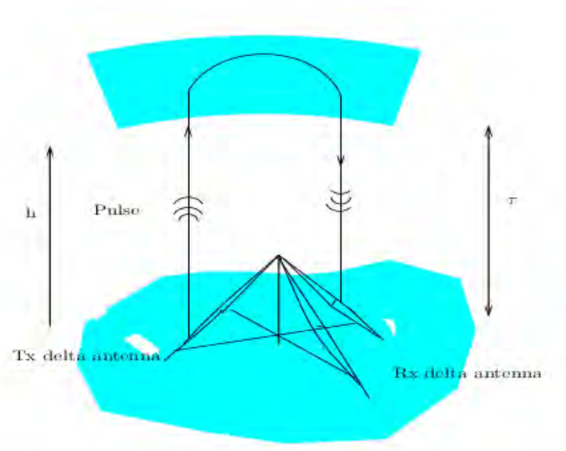

Figure 3.7: Schematic diagram illustrating the components and operation of the pulse ionosonde, adapted from Amabayo (2011).

The ionosonde transmits short pulses from the transmitter (Tx), consisting of a number of cycles that sweep over a wide frequency range, straight up into the ionosphere, as shown in Figure 3.7. Historically, Appleton & Barnett (1925) and Breit & Tuve (1926) were the first to use ionosondes to confirm the existence of the ionosphere. A short historical review and evolution of the development of ionospheric sounders can be found in Villard Jr (1976) and Bibl (1998). Ionosondes have been used extensively for various applications, such as remote sensing for monitoring long-term temporal and spatial variations of the ionosphere, and also for scientific research (Davies, 1990). A variety of ionospheric parameters can be obtained from ionosonde measurements, such as the maximum sounding frequency of the F2 region (foF2), and the maximum usable frequency reflected in the F2 region for a ground distance of 3000 km (MUF(3000)F2), the peak heights of the F2 region (hmF2), and ionospheric total electron content (TEC).

3.2.1 Principle of Ionospheric Sounding

The concept of ionospheric sounding goes back to the early 1920s with experimental proof of the existence of an ionised layer (Breit & Tuve, 1926 and Appleton & Barnett, 1925). The principle of ionospheric sounding experiments is used to determine the electron density profile by varying the probing frequency and measuring the time it takes a radio signal wave to travel from the transmitter to the reflection point and back.

Appleton & Barnett (1925) derived a refractive index equation that describes the propagation of radio waves in the ionosphere in the Earths magnetic field. In the derivation, a uniform external magnetic field **B** makes an angle θ with the direction of propagation of a plane electromagnetic wave in the x-direction. The expression for the refractive index μ of the ionosphere in terms of the Appleton-Hatree formula for the negligible collision frequency in the F region, when $Z = 0$, expressed as (Davies, 1990):

$$\mu^2 = 1 - \frac{X(1-X)}{(1-X) - \frac{1}{2}Y_T^2 \pm \left[\frac{1}{4}Y_T^4 + (1-X)^2 Y_L^2\right]^{1/2}}, \tag{3.22}$$

where X, and Y are magneto-ionic parameters, i.e., dimensionless quantities defined by the following expressions:

$$\begin{aligned} X &= \omega_N^2/\omega^2 \\ Y_T &= Y cos(\theta) = \frac{\omega_H}{\omega} cos(\theta), \\ Y_L &= Y sin(\theta) = \frac{\omega_H}{\omega} sin(\theta), \end{aligned} \tag{3.23}$$

where ω is the angular frequency of the propagating wave, $\omega = 2\pi f$, ω_H is the electron gyrofrequency, $\omega_H = Be/m$, ω_N is the angular plasma frequency, $\omega_N^2 = N_e e^2/m\epsilon_0$, f: signal carrier frequency (Hz), m: electron rest mass (9.11×10^{-31} kg), e: charge of an electron (-1.602×10^{19} C), N_e : electron density (per m^3), ϵ_0 : permittivity of free space (8.854×10^{-12} Fm^{-1}).

Note that the the positive (+) and negative (-) signs in equation 3.22 refer to the ordinary and extraordinary waves, respectively. In the absence of an external magnetic field $Y_L = 0$ and $Y_T = 0$ (Rishbeth & Garriott, 1969; Basu *et al.*, 1985; Hargreaves, 1992; Zolesi & Cander, 2014). Equation 3.22 of the Appleton-Hartree equation for the phase refractive index can be simplified as:

$$\mu^2 = 1 - X = 1 - \left(\frac{\omega_N}{\omega}\right)^2 = 1 - \frac{N_e e^2}{4\pi^2 \epsilon_0 m f^2}. \tag{3.24}$$

Vertical reflection occurs when $\mu = 0$, and this means from the equation 3.24 the plasma frequency ω_N equals the wave frequency ω. Substitute the respective values for angular plasma frequency, angular frequency of the propagating wave, electron mass, electron charge and the permittivity of free space, and solve for N_e in equation 3.24:

$$N_e = 1.24 \times 10^{10} f^2, \tag{3.25}$$

where N_e and f are measured in units of electrons/m^3 and MHz, respectively. This implies that the maximum electron density of the F2 layer, $N_m F_2$, is directly proportional to the square of the critical frequency of the F2 layer, $f_0 F_2$.

The time of flight, τ, of the reflected radio wave is related to the virtual height, $h^{'}$, which is also related to the refractive index as follows:

$$h^{'} = \frac{c\tau}{2} = \int_0^{h_r} \frac{dh}{u}, \tag{3.26}$$

where c is the speed of light, u is the group speed, and h_r is the real height of reflection. It is clear from equation 3.26 that virtual height depends on the electron density profile, the geomagnetic field, and the frequency of the wave, since it depends on the refractive index, which is dependent on these parameters (Davies, 1990). For wave a to propagate through the ionosphere and go out into space, the virtual height has to be greater than the true height of reflection (Rishbeth & Garriott, 1969; Hargreaves, 1992).

3.2.2 The ionogram and its interpretation

The ionogram is the record of ionosonde measurements which is defined as a plot of virtual height against frequency. A typical example of an ionogram recorded at the Hermanus ionosonde station is shown in Figure 3.8. The ionogram displays two traces of the radio signal waves for each layer of the ionosphere: the ordinary (O) and extraordinary (X) waves, as shown in red and green, respectively. The overplotted black curves are the generated electron density profiles. The vertical asymptotes of the O and X traces represent the crit-

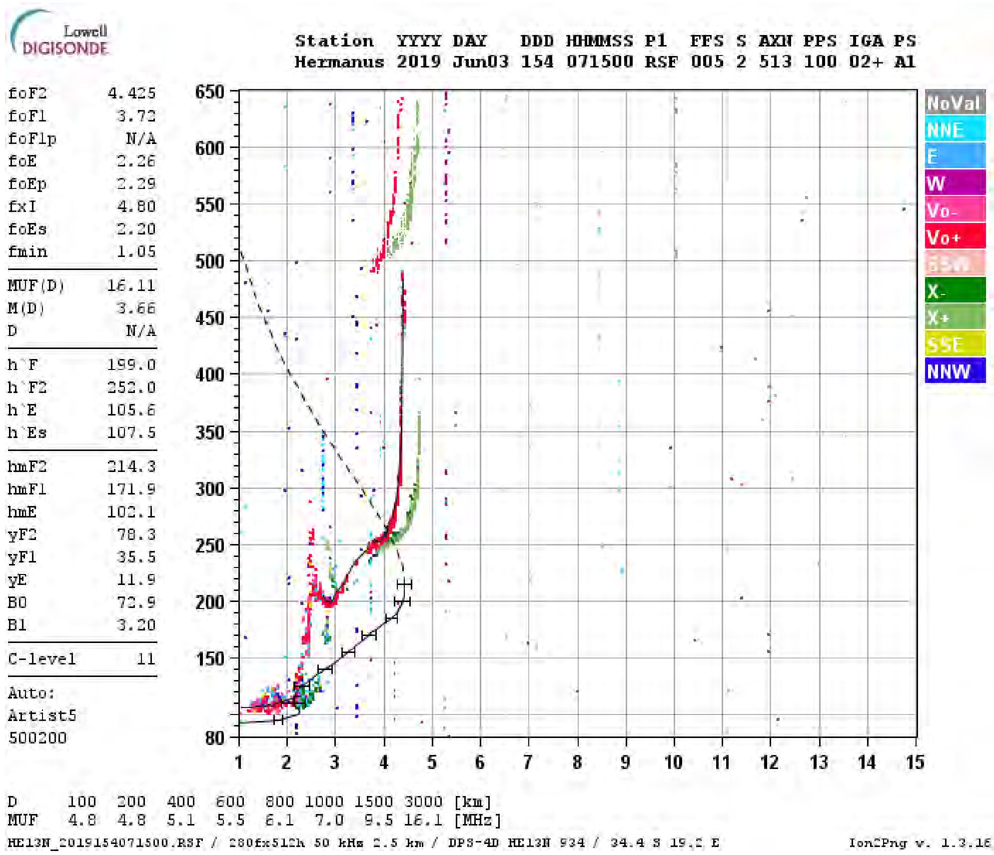

Figure 3.8: An example of an ionogram recorded at 7:15:00 UT on 03 June 2019 for the Hermanus (34.43° S, 19.23° E, 64.08° dip angle).

ical frequencies $foF2$ and $fxF2$ respectively, and are separated by approximately half the gyrofrequency (McNamara, 1991).

South Africa has a network consisting of four (4) ionosondes which are located at: Hermanus (34.43° S, 19.23° E, 64.08° dip angle), Louisvale (28.5° S, 21.2° E, 63.21° dip angle) station, Grahamstown (33.3° S, 26.5° E, 62.79° dip angle), and Madimbo (22.4° S, 30.9° E, 57.68° dip angle). The locations of the ionosondes are marked by red crosses sign on the map shown in Figure 3.1. Ionosonde data have a 15 minutes cadence, were processed using the SAO Explorer software (Reinisch *et al.*, 2005). This software is used to view ionograms and to extract their characteristics. For this research 30-minute binned hmF2 measurements from these ionosondes will be used to derive meriodional neutral wind using the servo method, which is explained in the next section.

3.2.3 Ionosonde-derived meridional neutral wind: servo model

The F2-layer was envisaged to behave like a servo mechanism, following an approximation method developed by Rishbeth (1967) to compute the theoretical diurnal variation of the peak electron density in the midlatitude ionosphere, observing that external forces, such as winds perturb the equilibrium distribution. Rishbeth (1967) investigated the effect of winds, on both day equilibrium layer and night stationary layer and deduced that the day-to-night changes of the height of the peak electron density, hmF_2, at midlatitudes, are caused largely by the action of winds on the F2-layer. The servo model has been successfully used in previous studies to derive meridional neutral wind at the midlatitude using the F2-layer (Dowdy, 1993; Richards, 1991; Fagundes *et al.*, 2008). Rishbeth *et al.* (1978) provides a detailed description of the servo model including the reasonable assumptions made when formulated. It is briefly described here. The derivation of the meridional neutral wind using the servo method starts from the continuity equation given by:

$$\frac{\partial N}{\partial t} = q - \beta N - \frac{1}{H}\frac{\partial N V_z}{\partial z}, \tag{3.27}$$

where N = ion/electron concentration, t = time, q = production rate, β = loss coefficient, V_z = vertical plasma velocity (positive upwards), H = scale height of the neutral ionisable gas given by $H = 0.058T_n$, with T_n being neutral temperature, and z = reduced height, measured in units of H. Note that since the temperature profile of the upper thermosphere is almost constant, the scale height is assumed to be height independent for simplicity. Also the contribution to the transport term in the continuity equation (i.e. dNV_z/dz) is assumed to be mainly in the vertical direction. The balance height of the ionospheric F2-layer (h_s) occurs where there is no applied drift. When multiplying equation 3.27 by H and integrating from $z = zm$ to $z = \infty$, which is from the peak of the F2 layer to the top of the ionosphere, the following is obtained:

$$H\int_{zm}^{\infty}\frac{\partial N}{\partial t}dz = H\int_{zm}^{\infty}(q - \beta N)dz - \Phi_m + N + N_m(V_{zm} - H\frac{dzm}{dt}), \tag{3.28}$$

where the subscript m denotes the parameter at the peak of the F2 layer, e.g., Φ_m is the vertically upward plasma flux at the top of the F2 region, i.e., the limiting value of NV_z at great height. The term $(V_{zm} - H\frac{dzm}{dt})$ is the relative vertical plasma velocity at hmF_2.

The following assumptions were made in the construction of the servo model:

- The topside of the layer maintains a constant shape that is expressed by the Chapman alpha layer, $a = 2.82$, such that its height-integrated ion content is aHN_m.
- q is proportional to e^{-z}, since the F_2 peak is sufficiently above the peak of the production

layer.

- The dominant ion is O^+ and decays by reacting with neutral N_2, in which case it may be assumed that β is proportional to e^{-kz}, where k is the ratio of atomic and molecular scale heights given as 1.75.

The resulting equation after implementation of these assumptions is:

$$aH\frac{dN_m}{dt} = q_m H - \frac{\beta_m N_m H}{k} - \Phi_m + N_m\left(V_{zm} - H\frac{dz_m}{dt}\right), \tag{3.29}$$

where aHN_m is the height integrated ion content of the top layer. On the assumption that the F2 layer is isothermal, the peak vertical drift velocity is expressed by the following (Vasseur, 1969):

$$V_{zm} = W - \frac{D_s sin^2(I)}{H\nu_m} = W - \frac{D_m}{2H}sin^2(I), \tag{3.30}$$

where W is the vertical drift applied to the layer by a wind or electric field, I is the magnetic dip, ν_m is the ion-neutral collision frequency (Rishbeth & Garriott, 1969) and D_m is the plasma diffusion coefficient. Substituting equation 3.30 into equation 3.29, dividing by N_mH, and rearranging:

$$\frac{dz_m}{dt} = \frac{q_m}{N_m} - \frac{\Phi_\infty}{N_m H} - \frac{\beta_m}{k} - \frac{a}{N_m}\frac{dN_m}{dt} - \frac{D_m sin^2(I)}{2H^2} + \frac{W}{H}. \tag{3.31}$$

Applying the assumptions of the continuity equation as given by Rishbeth *et al.* (1978), equation 3.31 can be approximated to:

$$\frac{dN_m}{dt} = q_m - c\beta_m N_m - \frac{\Phi_m}{aH}, \tag{3.32}$$

where c is an empirical constant that adjusts the relative importance of the transport processes and the loss terms at the F2-peak, and is estimated from idealised solutions of the full diffusion equation. Here c is assumed to be 1.73. Equation 3.32 assumes that the flux (Φ_m) is distributed evenly over the thickness of the topside layer (aH). Substitution of equation 3.32 into equation 3.31 leads to

$$\frac{dz_m}{dt} = (1-a)\frac{q_m}{N_m} + \frac{(kac-1)\beta_m}{k} - \frac{D_m sin^2(I)}{2H^2} + \frac{W}{H}. \tag{3.33}$$

Using relationships similar to those given by Rishbeth *et al.* (1978) and Dowdy (1993) i.e. $\beta_m = \beta_s e^{-kz_m}$, $D_m = D_s e^{z_m}$, $q_m = q_s e^{-z_m}$, and substituting these relations into equation 3.33 the equation becomes:

$$\frac{dz_m}{dt} = (1-a)\frac{q_s e^{-z_m}}{N_m} + \frac{(kac-1)\beta_s e^{-kz_m}}{k} - \frac{D_s e^{z_m} sin^2(I)}{2H^2} + \frac{W}{H}. \tag{3.34}$$

Where there is no forcing that causes ionisation drift ($W = 0$), the nighttime F2-peak forms a 'balance/stationary height'. The balance height h_s occurs when there is a balance between the chemical loss and diffusion (Rishbeth *et al.*, 1978), i.e.

$$\beta_s = \frac{kD_s sin^2(I)}{2H^2(kac-1)}, \tag{3.35}$$

where $\beta_s = k_1[N_2] + k_2[O_2]$ with k_1 and k_2 being temperature-dependent reaction rate coefficients given by Torr & Torr (1979), and $[O_2]$ and $[N_2]$ being O_2 and N_2 neutral densities, respectively.

The $q_s = 0$ at nighttime, and by substituting β_s into equation 3.34, the equation reduces to:

$$\frac{dz_m}{dt} = \frac{D_s sin^2(I)}{2H^2}\left(e^{-kz_m} - e^{z_m}\right) + \frac{W}{H}. \tag{3.36}$$

The vertical plasma drift (W), being the result of a combination of motion along the magnetic field lines due to a meridional wind and of an ion drift, induced by the east-west electric field, is given by:

$$W = V_e cos(I) + U_m cos(I) sin(I), \tag{3.37}$$

where V_e is the ion drift velocity component perpendicular to the Earths magnetic eld, which can be neglected for the midlatitude because it does not have a significant effect on the meridional wind (Buonsanto *et al.*, 1989, Buonsanto, 1990, Muella *et al.*, 2008), and U_m is the horizontal component of the neutral wind. Substituting equation 3.37 into equation 3.36, and at night $dz_m/dt = 0$, equation 3.36 reduces to:

$$-U_m cos(I) sin(I) = \frac{D_s sin^2(I)}{2H}\left(e^{-kz_m} - e^{z_m}\right). \tag{3.38}$$

When the variation of z_m is small, e.g., less than the scale height H, then $e^{-kz_m} - e^{z_m} = -z_m(k+1)$, and $z_m = (hmF2 - hs)/H$ (Yagi & Dyson, 1985). With this approximation equation 3.38 becomes:

$$U_m cos(I) sin(I) = \frac{(k+1)D_s sin^2(I)}{2H}\left(\frac{hmF2 - h_s}{H}\right). \tag{3.39}$$

Solving for U_m yields the servo model equation:

$$U_m = \frac{hmF2 - h_s}{\alpha}, \tag{3.40}$$

where

$$\alpha = \frac{2H^2 cos(I)}{(k+1)D_s sin(I)}, \tag{3.41}$$

and D_s is the plasma diffusion coefficient, expressed by

$$D_s = D_{in}\left(1 + \frac{T_e}{T_i}\right), \tag{3.42}$$

and D_{in} is the overall ionneutral diffusion coefficient that reflects the relative importance of the diffusion of O^+ through the neutral atmosphere and its collision with O, O_2 and N_2. T_e and T_i represent the electron and ion temperatures, respectively. The coefficient D_{in} is calculated from the formula derived by Banks & Holzer (1968) and Dalgarno (1964):

$$D_{in} = \frac{3.19 \times 10^{19} T_i}{f(T_n + T_i)^{\frac{1}{2}}[O] + 42.3[N_2] + 41.1[O_2]}, \tag{3.43}$$

where f is the Burside factor and T_n is the neutral temperature.

3.3 Space weather indices

There are many solar and geomagnetic parameters that make it possible to determine space weather conditions. The geogmanetic indices Kp and Ap as well as the solar radio flux $F_{10.7}$ were used as indicators of the space weather conditions. They are briefly discussed in the following sections.

3.3.1 Kp index

The Kp index indicates the level of disturbance of the magnetic field observed on a magnetometer relative to a quiet day. It is measured in a 3-hour window by a global network of 13-magnetic observatories that lie in the midlatitude region. Only the horizontal component (H) and magnetic declination (D) are used to determine the Kp index (Mayaud, 1967; Menvielle & Berthelier, 1991). Storms or geomagnetic conditions are classified as follows, based on the Kp index (Kudeki *et al.*, 2007; Sergeyeva *et al.*, 2021): 0–3 (quiet magnetic conditions), 5–6 (moderate magnetic storm), and 6–9 (disturbed magnetic conditions). This project focused on thermospheric wind dynamics during quiet conditions, so observation nights during which the Kp index $\leqslant 3$ were used in the analysis that would be discussed in chapters 4 and 5.

3.3.2 Ap index

The Ap index is a linear measure of the Earth's magnetic field and is a parameter that describes the general level of geomagnetic activity over the globe for a given day. The Ap index has a semi-logarithmic relationship with the range which defines the Kp index. The daily Ap is obtained by averaging the eight 3-hour values of Ap for each day. Geomagnetic conditions are classified as follows, using the Ap index (Fraser-Smith, 1972): quiet magnetic conditions ($0 \leqslant \text{Ap} \leqslant 26$), an active/moderate storm ($27 \leqslant \text{Ap} \leqslant 47$) and disturbed or storm magnetic conditions ($48 \leqslant \text{Ap} \leqslant 400$).

3.3.3 Solar radio index ($F_{10.7}$)

The solar radio flux ($F_{10.7}$) is one of the most widely used indices of solar activity, and to determine strength of solar radio emission in a 100 MHz-wide band centred on 2800 MHz (a wavelength of 10.7 cm), averaged over an hour. The variation with $F_{10.7}$ reflects variation of the thermospheric winds. Therefore, the solar activity index is of paramount importance in the analysis of thermospheric winds. It is expressed in solar flux units (sfu), where 1 sfu = $10^{-22} W m^{-2} Hz^{-1}$. The solar flux scale can vary from 50-300 which indicate quiet to disturbed conditions. The solar flux is closely related to the level of ionisation and the electron concentration in the F2 region.

3.4 Data analysis techniques

In order to study long term wind variability at different months, a statistical analysis was done by computing weighted mean and sample standard deviations. The weighted mean for x, where x is the set of neutral wind or hmF2 measurements, was computed as:

$$\tilde{x} = \frac{\sum_i x_i w_i}{\sum_i w_i}, \tag{3.44}$$

where $w_i = \frac{1}{\sigma_i^2}$ is the weight and σ_i is the uncertainty of each measurement. The sample standard deviation was computed as:

$$s = \sqrt{\frac{1}{n-1} \sum_i (x - \tilde{x})^2}, \tag{3.45}$$

where n is the number of samples in x. When seasonal variation is discussed, seasons were categorised as summer (December-February), autumn (March-May), winter (June-August) and spring (September-November).

In order to investigate differences between data (observations) and models (e.g., servo model), a Taylor diagram (Taylor, 2001) was used. In this diagram a standard deviation s_x of the data x, s_d the standard deviation of the model d, root mean square error ($RMSE$) and the correlation coefficient R between the data and model are used to quantify the level of performance of the model. Using a set of these parameters to assess a match between models and observations is advantageous over using a single parameter since the latter can lead to misleading conclusions.

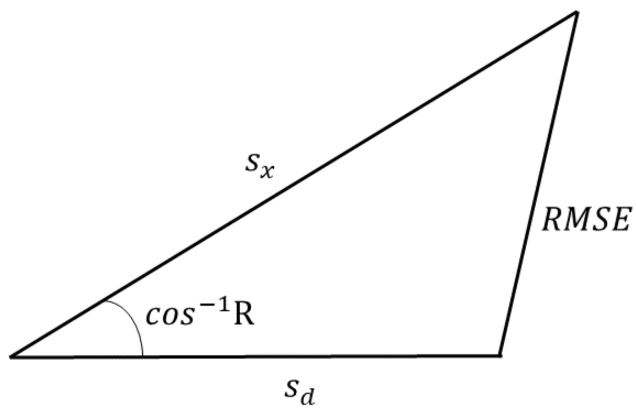

Figure 3.9: A diagram showing the relationship between various elements on Taylor diagram, adapted from Taylor (2001)

The correlation coefficient R between x and d is defined as:

$$R = \frac{\frac{1}{N}\sum_{n=1}^{N}(x_n - \tilde{x})(d_n - \tilde{d})}{s_x s_d}, \tag{3.46}$$

where N is the number of data points.

The $RMSE$ is the statistic used to quantify differences or errors between a model and measured data and is defined as (Taylor, 2001):

$$RMSE = \left[\frac{1}{N}\sum_{n=1}^{N}\Big[(x_n - \tilde{x}) - (d_n - \tilde{d})\Big]^2\right]^{1/2}. \tag{3.47}$$

The relationship between R, $RMSE$, s_x, and s_d can be derived by means of the law of cosines, as illustrated in Figure 3.9, and is expressed by (Taylor, 2001):

$$RMSE = \sqrt{s_x^2 + s_d^2 - 2s_x s_d R}. \tag{3.48}$$

To keep the geometry the same, a normalised Taylor diagram (in which the standard deviation of the model is normalised to the standard deviation of the data) was used. An example is given in Figure 3.10, which shows that a model that perfectly matches the data would be located at the intersection between the $s_r = 1$ arc and the x axis (indicating $R = 1$). The $RMSE$ between model and data are denoted by the green semi-circles, centred on the point of perfect agreement. In general, a model that agrees well with observations will be close to the point marked "data" (in red line) on the x-axis. Such a model will have relatively high correlation coefficient and low $RMSE$ (Guo *et al.*, 2016; Taylor, 2001).

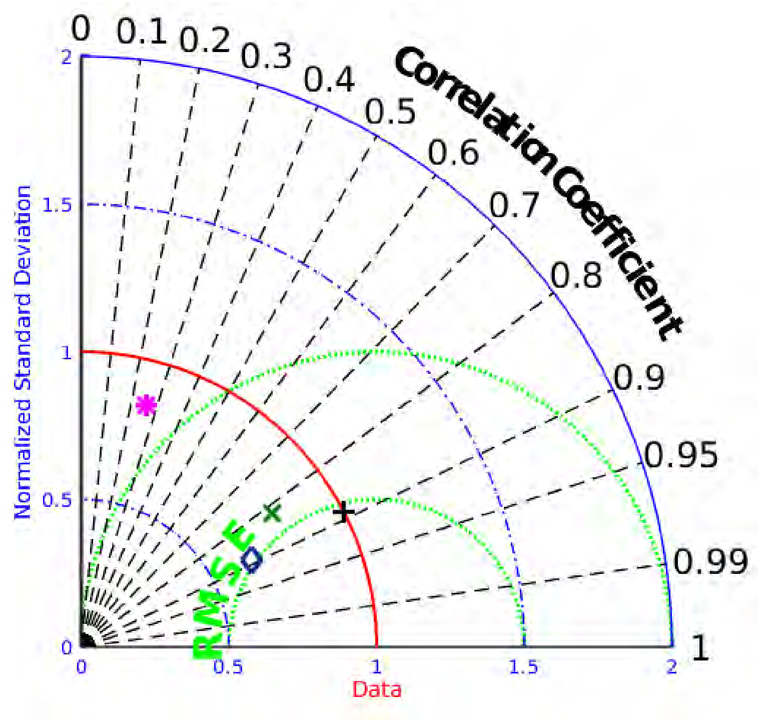

Figure 3.10: An example of a normalised Taylor diagram for different models.

3.5 Summary

This chapter briefly discussed the basic principles of an FPI, including the instrument design, operation, and data processing methodology that was used to obtain the thermospheric winds. This chapter also described ionospheric sounders and the ionospheric parameters, such as electron density and hmF2, that are derived from ionospheric sounder data to characterise the ionosphere. Since the ionosonde measured hmF2 will be used to derived meridional neutral winds using the servo model, a brief derivation of this model was also included in this chapter. Statistical analysis that would be used to gauge the accuracy of different models was also presented. Different space weather indices, such as Kp, Ap and $F_{10.7}$, that make it possible to determine space weather conditions were discussed.

Chapter 4

Climatological study of thermospheric winds over Sutherland, South Africa

This chapter presents the first climatology and analysis of thermospheric winds from Fabry-Perot interferometer (FPI) observations over Sutherland, South Africa, during quiet geomagnetic conditions. This study also included the first validation of the Horizontal Wind Model, version 2014 (HWM14) over South Africa and therefore a brief introduction to the model is also included in this chapter.

4.1 The Horizontal Wind Model (HWM)

The Horizontal Wind Model (HWM) is a standard empirical model that provides an estimate of the global climatology of the horizontal neutral wind of the upper atmosphere (Hedin *et al.*, 1988). The input parameters for the model include latitude, longitude, altitude, date, and time. It was first developed by Hedin *et al.* (1988), using only satellite data from Dynamic Explorer 2 and Atmospheric Explorer. Since then there have been several improvements to increasingly include measurements from diverse instruments, such as incoherent scatter radars (ISRs), FPIs, and satellite measurements from both optical techniques and in situ mass spectrometer from different geographical locations (Hedin *et al.*, 1988; Hedin *et al.*, 1991; Hedin *et al.*, 1996; Drob *et al.*, 2015). The recent HWM was updated in 2014, otherwise called HWM14, using $\sim 73 \times 10^6$ data spanning 60 years from 44 different instruments in different geographical locations (Drob *et al.*, 2015). In places where no local data were used in the model development (such as southern African midlatitudes), the model fills in the gaps by using spherical harmonic functions that contain annual, semiannual, diurnal, semidiurnal, and terdiurnal harmonic variations. The equation representing cyclical climatological spatial-temporal variations of the zonal wind U(τ,δ,θ,ϕ,z), is formulated as follows in the model (Drob *et al.*, 2015):

$$U(\tau, \delta, \theta, \phi, z) = \sum_j \beta_j(z) u_j(\tau, \delta, \theta, \phi) \tag{4.1}$$

where τ is the day of the year, δ is the solar local time, θ is the latitude, ϕ is the longitude, z is the altitude, and β_j represents the jth vertical cubic B-spline weighting kernel. The horizontal variations $u_j(\tau, \delta, \theta, \phi)$ for the jth vertical model kernel are represented by (Drob *et al.*, 2015):

$$u_j(\tau, \delta, \theta, \phi) = \sum_{s=0}^{S=2} \sum_{n=1}^{N=8} \Psi_j^1(\tau, \theta, s, n) + \sum_{s=0}^{S=2} \sum_{l=1}^{N=3} \sum_{n=1}^{N=8} \Psi_j^2(\tau, \theta, s, l, n) + \sum_{s=0}^{S=2} \sum_{m=1}^{M=2} \sum_{n=1}^{N=8} \Psi_j^3(\tau, \theta, s, m, n) \tag{4.2}$$

where n represents the order in latitude, $\Psi_j^1(\tau, \theta, s, n)$ includes the annual and semiannual harmonics in terms of seasonal wave number s, $\Psi_j^2(\tau, \theta, s, l, n)$ includes the diurnal, semidiurnal and terdiurnal harmonics expressed in terms of tidal wave number l, $\Psi_j^3(\tau, \theta, s, m, n)$ includes the stationary planetary wave harmonics with longitudinal wave number m. The unknown model coefficients for these three terms can be determined by solving an overdetermined linear inverse problem. Similarly, the meridional winds take this same form with slightly different unknown model coefficient. Note that the model assumes that the horizontal winds are zero at the poles. One of the advantages of this model is that when and where appropriate, HWM14 reduces the computational complexity of theoretical and applied calculations by avoiding the need to simultaneously compute the wind fields from first principles and validate physical understanding of neutral wind fields in the upper atmosphere.

4.2 Results

Figure 4.1 presents seasonal occurrence of solar flux (F10.7), and geomagnetic activity indices Ap and Kp during the period of this study, i.e. February 2018–January 2019. The figure shows that the solar and geomagnetic activies are low throughout this period as the solar flux ranged between 65 and 85 solar flux units (sfu) where 1 sfu = 10^{-22} W/m^2/Hz, Kp ≤ 3, and Ap < 25. Figure 4.2 shows the number of nights having FPI observations, the number of observations nights which the geomagnetic conditions were quiet, and the number of observations nights during which the viewing and geomagnetic conditions were clear and quiet in each month during the period of study. According to this figure at least 65% of the nights with wind observations in each month had clear viewing conditions and were geomagnetically quiet. The next sections will first show a case study illustrating typical night-to-night variability seen in the FPI measurements, followed by the climatological variations.

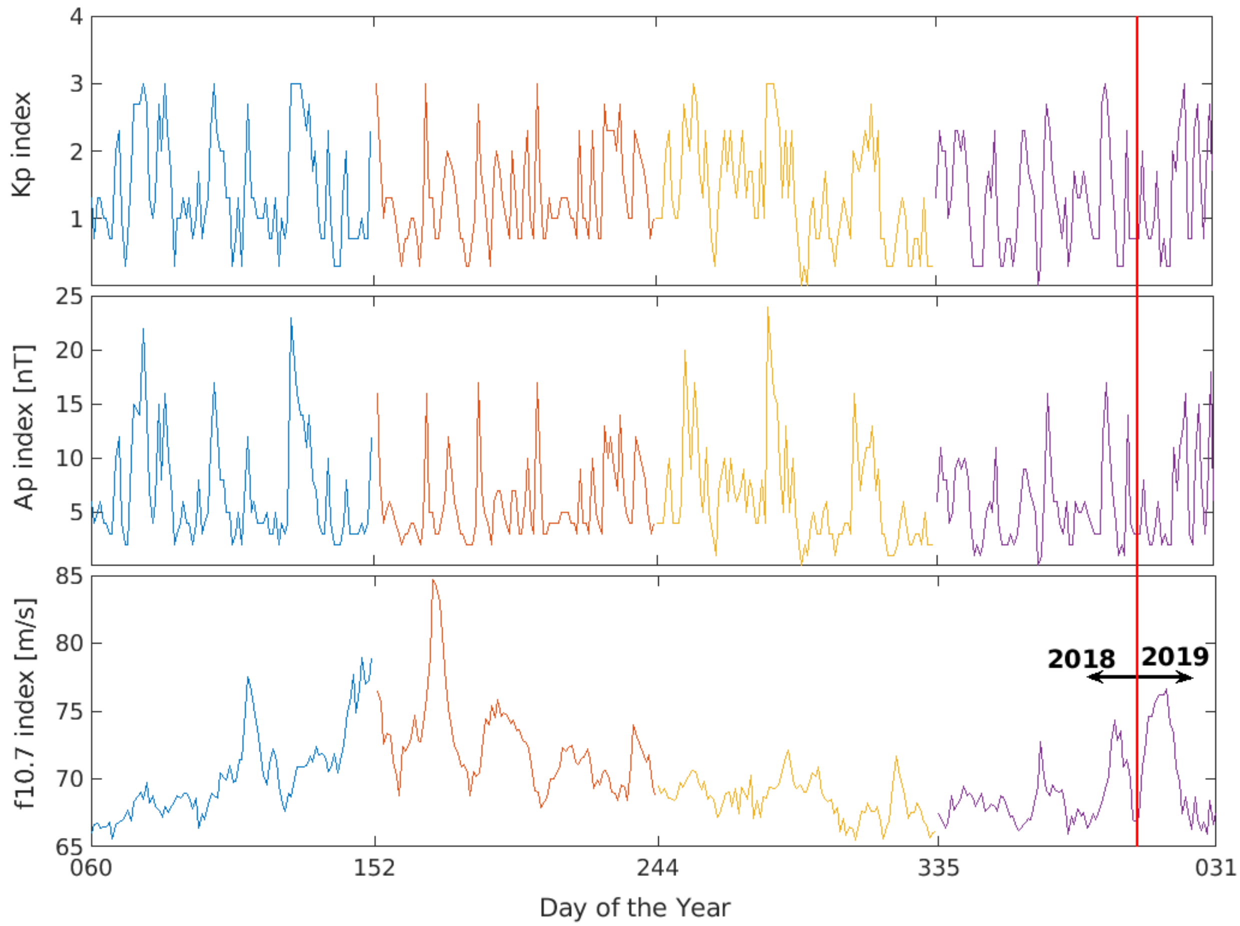

Figure 4.1: The seasonal occurrence of the Kp (top row), Ap index (middle row) and solar flux (third row) where blue, red, yellow and indigo represent autum, winter, spring, and summer, respectively.

4.2.1 Night-to-night variability of thermospheric winds

Figure 4.3 presents FPI measurements of the thermospheric zonal and meridional winds (top and bottom panels) obtained over the continuous period of 18 to 23 April 2018. Note that solar local time (SLT) defines noon as the time when the sun is the highest in the sky and can be mathematically calculated using:

$$SLT = t_{UT} + \theta \frac{24}{360^\circ}, \tag{4.3}$$

where SLT is the solar local time (hours), t_{UT} is the universal time (hours), and θ is the longitude of our FPI site. Therefore in this study $SLT = t_{UT} + 1.4$. From Figure 4.3 it is clear that the wind direction is predominantly eastward (positive) from dusk to about midnight, and switches westward (negative) after midnight until dawn. On most nights, the zonal

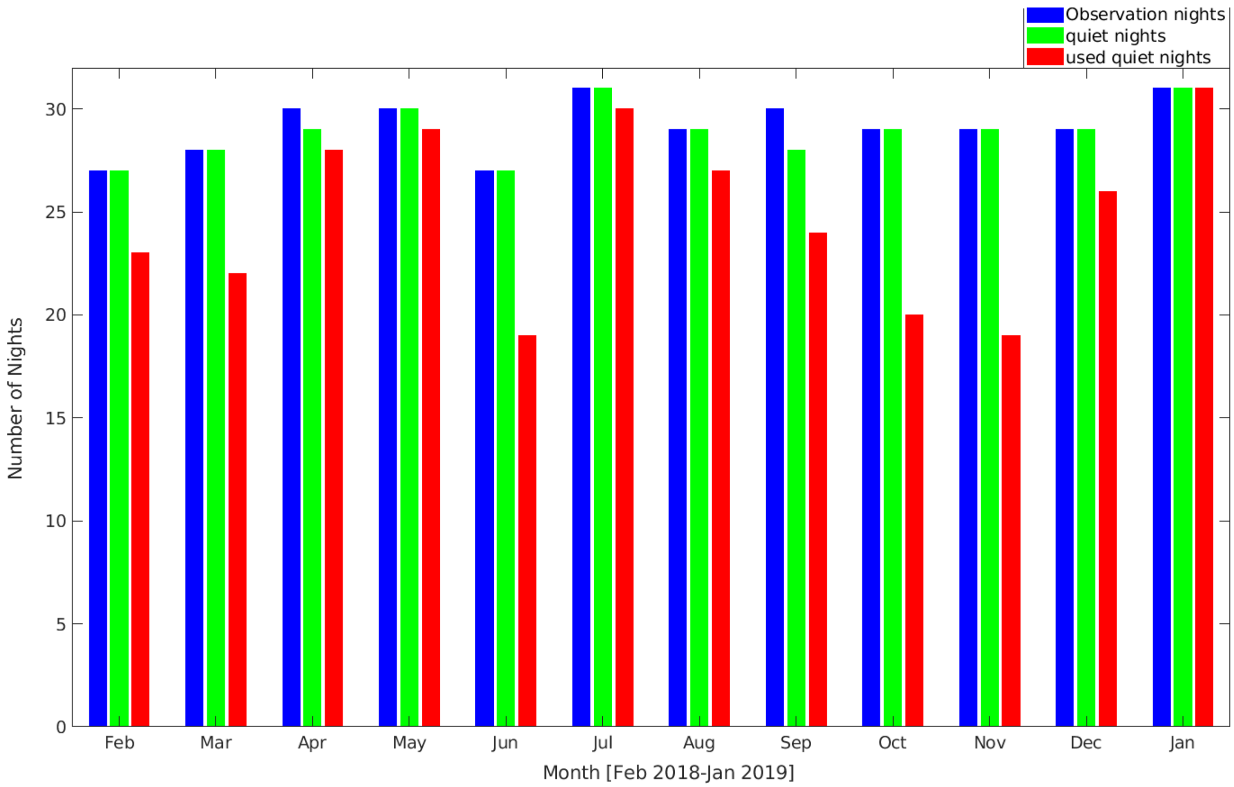

Figure 4.2: The number of observation nights (blue), the number of observations nights that were quiet (green), and the number of observations nights that were clear and quiet (red) per month from February 2018 to January 2019.

wind amplitude steadily increases to reach a maximum of around 100–150 m/s at around 21:00–01:00 SLT, except on the 19th of April, where the zonal wind varies dynamically. The westward zonal wind reaches a maximum of about 100 m/s (18 and 19 April) and 50 m/s (21 and 23 April) around 05:00 SLT. However, the westward wind on the 20th and 22nd of April is much slower compared to the other nights, reaching speeds not greater than 20 m/s.

For most nights (i.e. April 18, 20, 21, 23) the meridional wind direction is predominantly poleward (negative) before ∼23:00 SLT and switches equatorward (positive) to reach a peak of around 100–150 m/s at ∼01:30 SLT. However, the meridional wind on the 19th, 20th and 22nd of April deviates from the general trend observed on the other nights. On the 19th of April the meridional wind is mostly equatorward throughout the night, except for 2 hours between 22:50 and 01:50 SLT when it is poleward. On the 20th and 22nd of April the meridional wind is initially poleward but erratically changes direction between equatorward and poleward for the rest of the night.

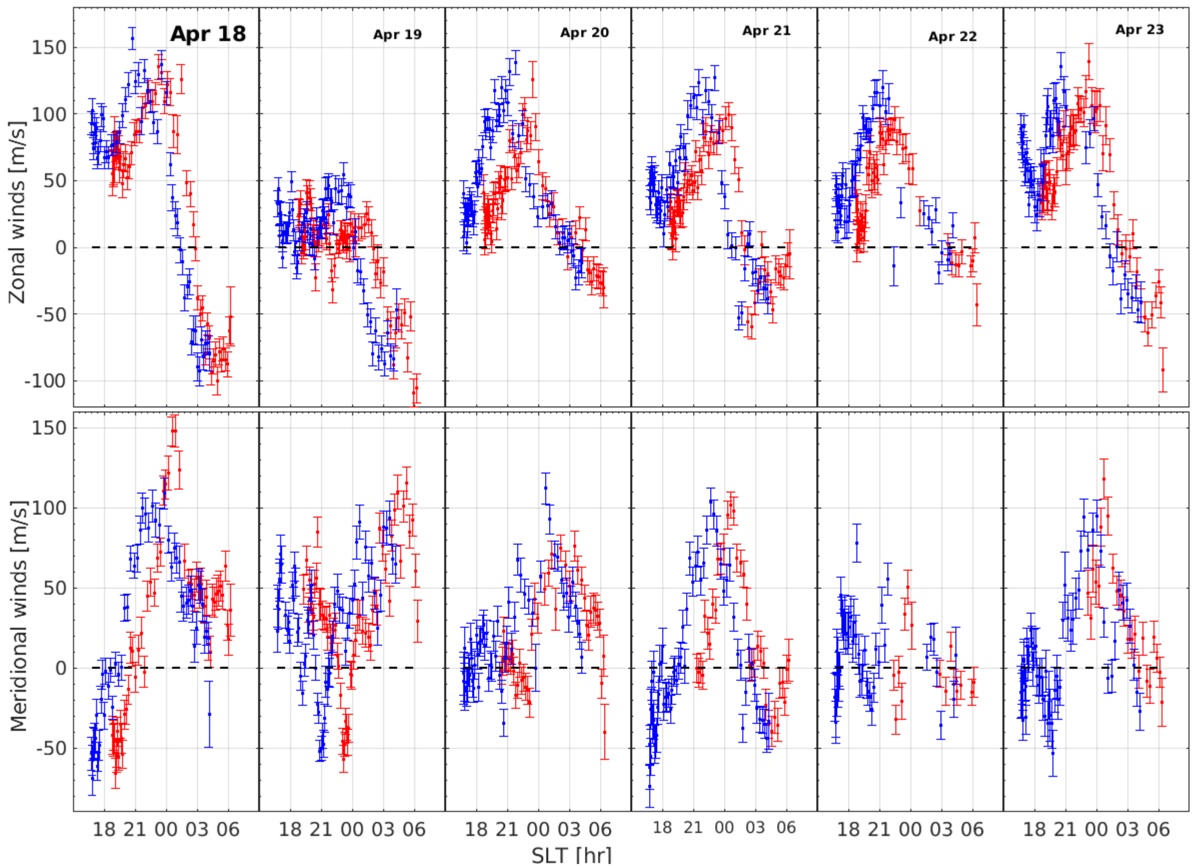

.

Figure 4.3: Sequential nights (18 to 23 April 2018) of zonal wind measurements (top row) for west (red dots) and east (blue dots) directions, positive (negative) values represent eastward (westward) winds. Meridional wind measurements (second row) for south (red dots) and north (blue dots) directions, negative (positive) values indicate polewards (equatorward) winds

4.2.2 Meridional and zonal wind monthly averages

The contour plots in Figure 4.4 show the monthly averaged meridional (top) and zonal (bottom) winds during February 2018–January 2019. The annual behavior shows meridional wind that is more equatorward during the summer, although poleward wind is seen in the early evening during local winter. In addition to the annual variation, the meridional wind exhibits semiannual and quasi-terannual variations where the wind velocities peak around the summer and winter solstices (i.e. January and June) as well as around spring equinox (i.e. September), with the highest peak seen in summer. The zonal wind exhibits an annual variation and is more eastward during the winter than during the summer, the wind is higher in the winter months compared to the other seasons.

Monthly averages of the FPI meridional and zonal winds measurement made between Febru-

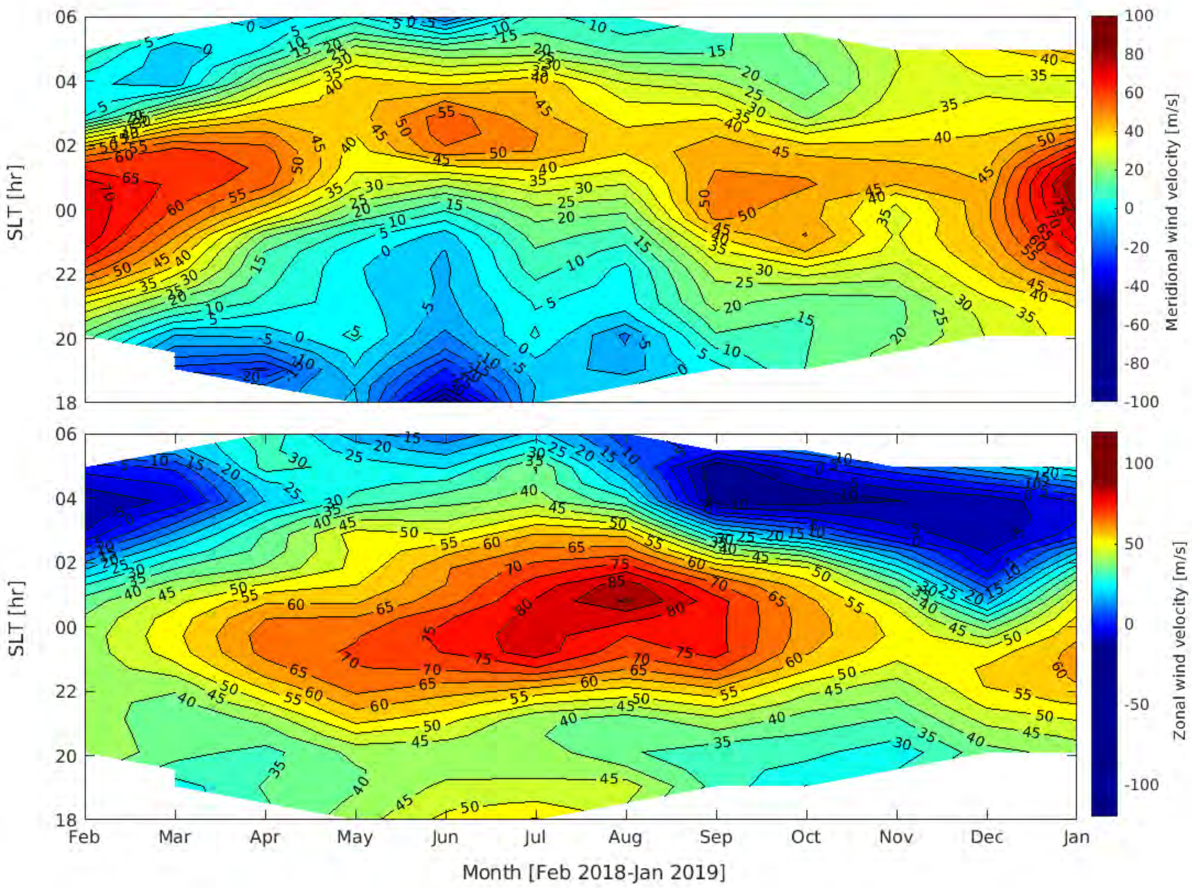

Figure 4.4: Contour plots of the monthly-averaged meridional wind (top) and zonal wind (bottom) measured by the FPI.

ary 2018 and January 2019 are presented in Figures 4.5 and 4.6, respectively. Also plotted are winds provided by the HWM14 model (green curves). Generally, for most months (March–November) the observed meridional wind is poleward (southward; negative) after dusk, turning equatorward and remaining in this direction for the rest of the night or turning poleward again a couple of hours before dawn. The poleward-to-equatorward transition time is between 21:00 and 02:00 SLT for May–November, and between 04:00 and 06:00 SLT for March and April. During February the measured meridional wind is equatorward until 04:00 SLT when it turns poleward, while in December and January wind flows equatorward only. For most of the months (with the exception of May–August) an increase in measured meridional wind is observed from the early evening to reach a premidnight peak of $\sim$ 70–90 m/s before decreasing and turning poleward. The peak is observed post midnight for the months of May-August. This indicates that the peak of the equatorward wind shifts from around midnight in the summer months to postmidnight in winter months. Also, during

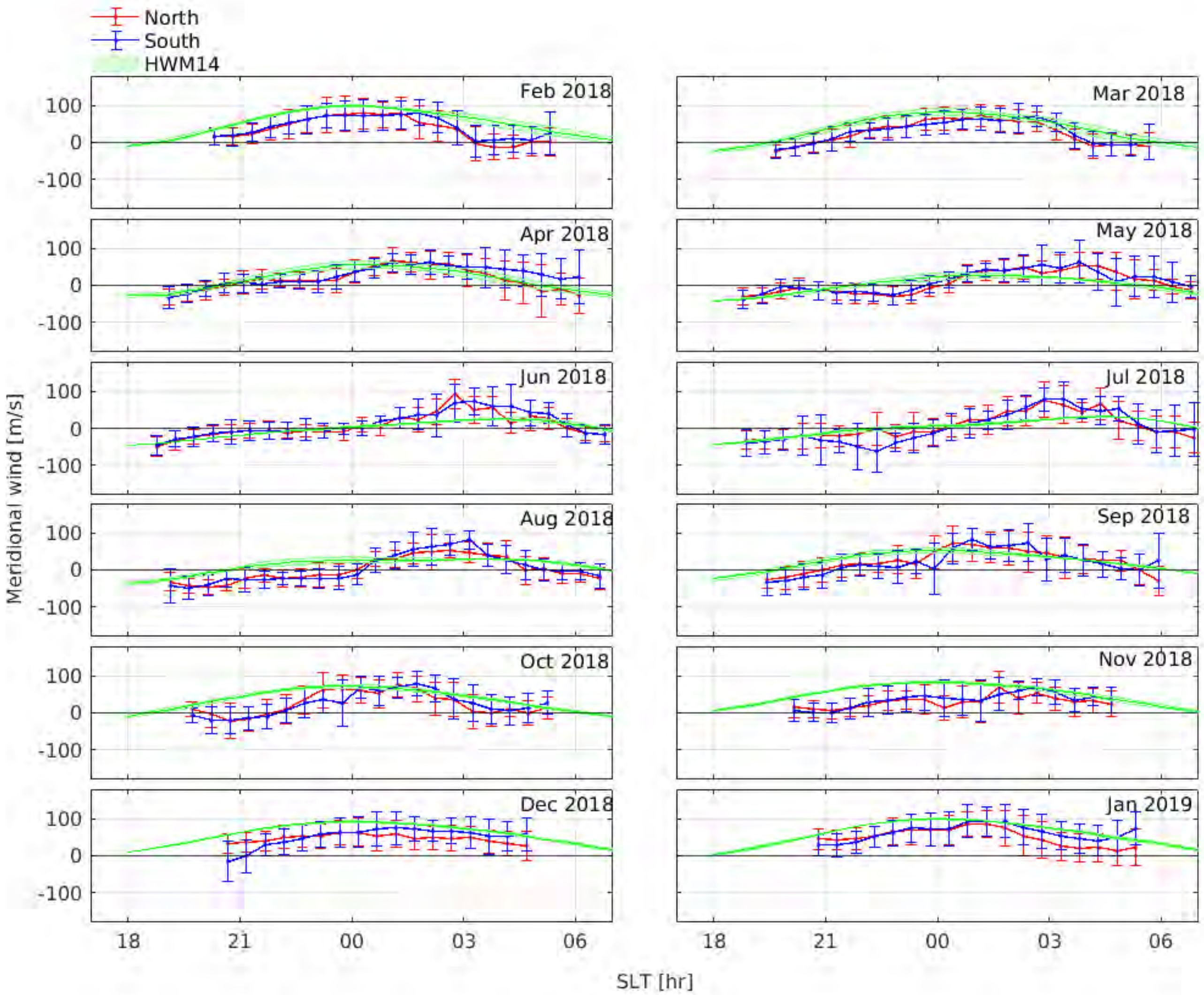

Figure 4.5: Monthly-averaged meridional wind measured by the FPI (red and blue) and predicted by HWM14 (green) between February 2018 and January 2019. Negative (positive) values indicate polewards (equatorward) winds. The error bars indicate standard deviation in the measurements while thickness in the HWM14 represents the range of variability.

the summer months the measured meridional wind is only or mostly equatorward. For the winter months (May–July) it is predominantly poleward (negative) during the evening period between 19:00 and 21:00 SLT and changes to equatorward at midnight. This is followed by a gradual decrease in the amplitude of meridional wind and a poleward reversal before dawn. While this wind direction change is also observed during spring and autumn months, the switch in direction occurs much later in winter, at around midnight, compared to around 20:30–21:00 SLT during the months of March, April and September.

In comparison to the measured winds, the HWM14 model generally captures a similar wind

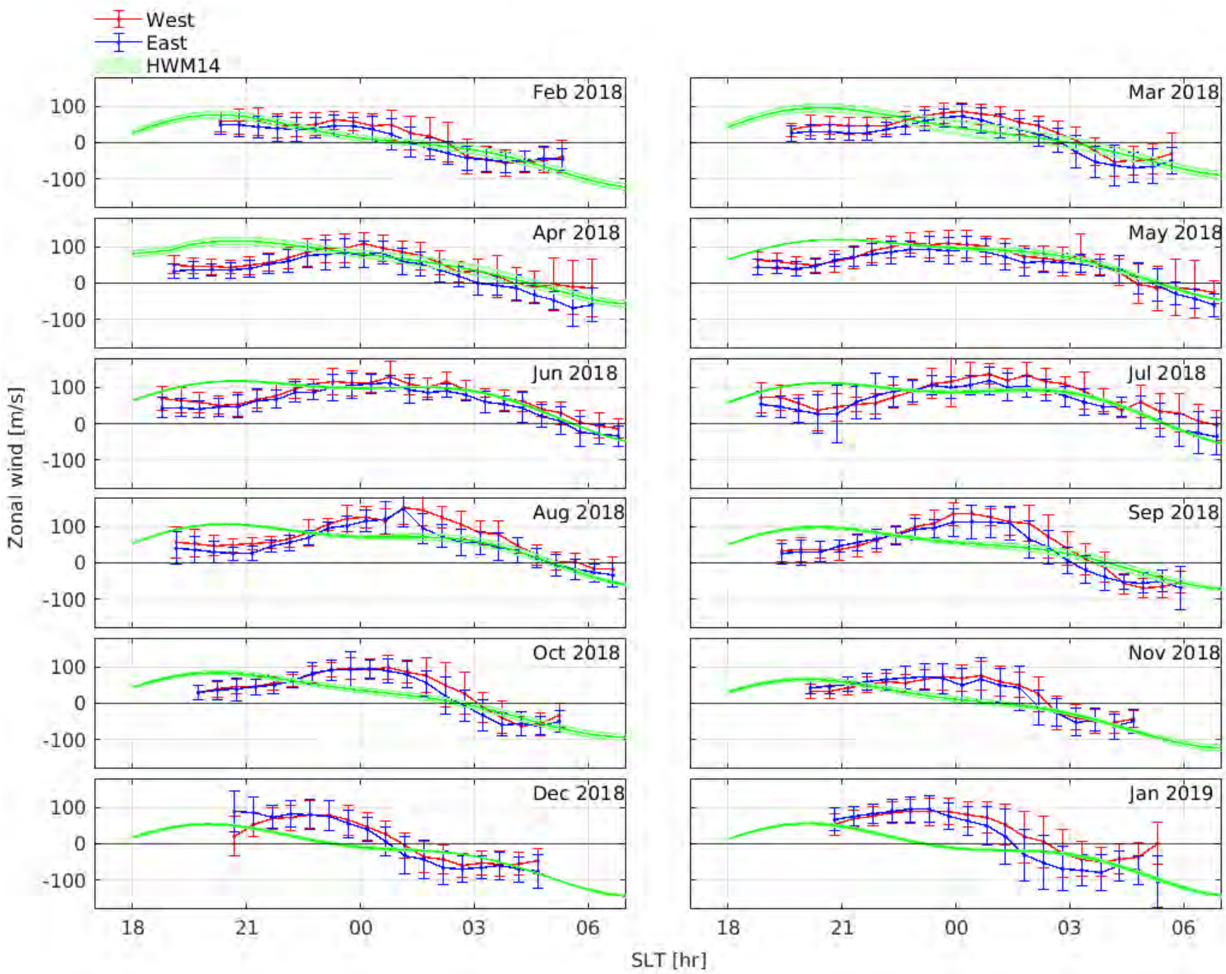

Figure 4.6: Monthly-averaged zonal wind (red and blue FPI, and green HWM14) between February 2018 and January 2019. Positive (negative) values represent eastward (westward) winds.

trend for the months of October through February i.e. HWM14 model predicted equatorward wind for all or most observed hours of the nights. Also, similar to the FPI, the HWM14 results during the months of April–September show a poleward wind in the early evening which later switches equatorward. Furthermore, the amplitudes of the HWM14 meridional winds during the winter months (May–August) are smaller than summer months (November-February) in general agreement with the measurements.

However, when looking at the details of the comparison there are several discrepancies between the data and model in regards to the time of wind direction transition, the amplitude of wind, and the time when the peak of equatorward wind occurs. For instance, the HWM14 model overestimates the meridional winds by $\sim$ 20 m/s in the summer months, mostly at the beginning of the night. Also, the model predicts the peak of the equatorward meridional wind much earlier during April, August–January, while it occurs later during the months of June-July compared to measurements from the FPI. The time difference between the peaks in HWM14 and FPI measurements can vary between 2 hours (April) and 5 hours (August). These sort of discrepancies are perhaps not terribly surprising given that the general construction of HWM14 lacked data from the Africa region.

Turning to the zonal winds, the direction of the measured zonal wind presented in Figure 4.6 is predominantly eastward (positive) before midnight, and westward (negative) post-midnight until predawn. For all months, an increase in zonal wind is observed from the early evening to reach a premidnight peak of $\sim$ 90–120 m/s before decreasing and turning westward. The amplitude of the winds is larger during the winter months ($\sim$ 120 m/s; July and August) than the summer months ($\sim$ 60 m/s; February and December). This peak occurred much earlier during the winter months ($\sim$ 120 m/s; July and August) compared to the summer months ($\sim$ 60 m/s; February and December). The eastward-to-westward transition time is between 01:30 SLT and 02:00 SLT for the months of November-February, and between 04:00 and 05:30 SLT for months March-October. This indicates that the transition time occurs later during the winter season (May–August) compared to summer (December–February). For September, October, January and February, a peak in the eastward wind is observed around 23:00–02:00 SLT. Furthermore, the zonal wind around 19:00–22:00 SLT during spring and autumn (e.g. March, September, October and November) has lower values compared to the same time during winter and summer months (e.g. January and February).

Similar to the FPI measured zonal wind trends, the HWM14 model predicts eastward zonal wind during the evening hours prior to midnight ($\pm$3 hours) before switching to westward for the rest of the night. The eastward-to-westward transition time predicted by the HWM14 model is similar to those measured by the FPI for most months, e.g. February-October. However the model estimates a significantly earlier transition time for the months of November-January, with a discrepancy as large as $\sim$ 2 hours, creating what looks like a phase shift between the model and data. Between March and November the model disagrees with the observations from early hours of the evening (19:00 and 23:00 SLT), predicting eastward wind that is about $\sim$ 30 m/s faster than the FPI measurements. Furthermore, the peak of the eastward wind is predicted much earlier in time by the model compared to the observations, with a difference between the peak in HWM14 and FPI as large as $\sim$ 3 hours (e.g. March–October).

In the next section the apparent phase shift in the timing of the HMW14 zonal wind will be investigated further. This is motivated by the fact that the HWM14 is often used for background or boundary conditions in some models, or provides neutral winds variability estimates for methodical studies of the upper atmsophere for regions where there is a lack of instruments for measuring neutral winds (e.g. Hickey *et al.*, 2009; Harding *et al.*, 2019; Fisher *et al.*, 2015; Yuan *et al.*, 2013), since it is not limited to nighttime data nor affected by terrestrial weather conditions, like the FPI, and is not as expensive like the ISR. It is therefore crucial that the model captures the wind data accurately across the globe.

4.3 HWM14 correction: terdiurnal tide

As is evident in Figure 4.6, there is an apparent phase shift present in the zonal winds that offsets the peak seen in HWM14 to be approximately 2–3 hours earlier than that shown by the data. In order to investigate potential cause of this phase shift, a least squares fitting procedure, described in Chu (2019), was implemented to determine the contributions from the diurnal, semidiurnal and terdiurnal tides to the overall thermospheric wind in the model at 250 km altitude. In this procedure all the horizontal wind variation was assumed to be due to the diurnal, semidiurnal and terdiurnal tides and is described by a forward model as (Chu, 2019):

$$f = A_i sin(\omega_1 t + \gamma_i) + A_i sin(\omega_2 t + \gamma_i) + A_i sin(\omega_3 t + \gamma_i) + B, \tag{4.4}$$

where $\omega_1 = 2\pi/24$, $\omega_2 = 2\pi/12$, $\omega_3 = 2\pi/8$ are diurnal, semidiurnal and terdiurnal tidal components, respectively, t represents time in hours, A_i represents the amplitudes of the respective tidal components, γ_i represents the phases (in radians) of the tidal components ($i = 1, 2, 3$) and B is used to account for a non-zero mean signal. While this forward model is written in a slightly different form from the tides described in equation 2.22 the same form can be obtained if we let $\gamma_i = s\lambda - \phi_{n,s} - \pi/2$, where s is the zonal wave number, λ is the longitude and $\phi_{n,s}$ is the time of maximum at zero longitude. The forward model was inverted using a least squares methodology where $\left\{\hat{A}_i, \hat{\gamma}_i, \hat{B}\right\}_{i=1}^{i=3}$ was found such that:

$$\sum_{n=1}^{N} \left[y_n - f\left(t_n; \{A_i, \gamma_i, B\}_{i=1}^{i=3}\right)\right]^2, \tag{4.5}$$

is minimized. Here, y_n represents the averaged output of HWM14 at times δ_n, i.e.

$$y_n = \frac{1}{M} \sum_{j=mo}^{M} U(\tau_j, \delta_n, \theta, \phi), \tag{4.6}$$

where mo represents the first day of the month, M is the last day of the month, and τ represents the jth day in the month, and θ and ϕ are fixed by the site's latitude and longitude, and δ is the time of day.

The HWM14 modeled winds was decomposed into different tidal components by fitting the model's monthly averaged zonal wind to equation 4.4. Because factors influencing the terdiurnal tide occur much more locally than those influencing the diurnal or semidiurnal components (Fisher *et al.*, 2015; Jiang *et al.*, 2018; Chu, 2019), it is assumed that the changing characteristics of the terdiurnal tide will only affect the winds close to this site. Therefore, the components and the properties of the terdiurnal tide were adjusted to determine if through modifying it alone, a better data–model match can be found. Since the amplitude of the peak zonal wind estimated by the model matches the data relatively well, the focus is only on shifting the phase of the terdiurnal tide to create a better match between the model and data. For each month, a comparison of the averaged nightly winds obtained from FPI measurements, and binned and averaged winds from HWM14 was made, following the averaging technique described in chapter 3.

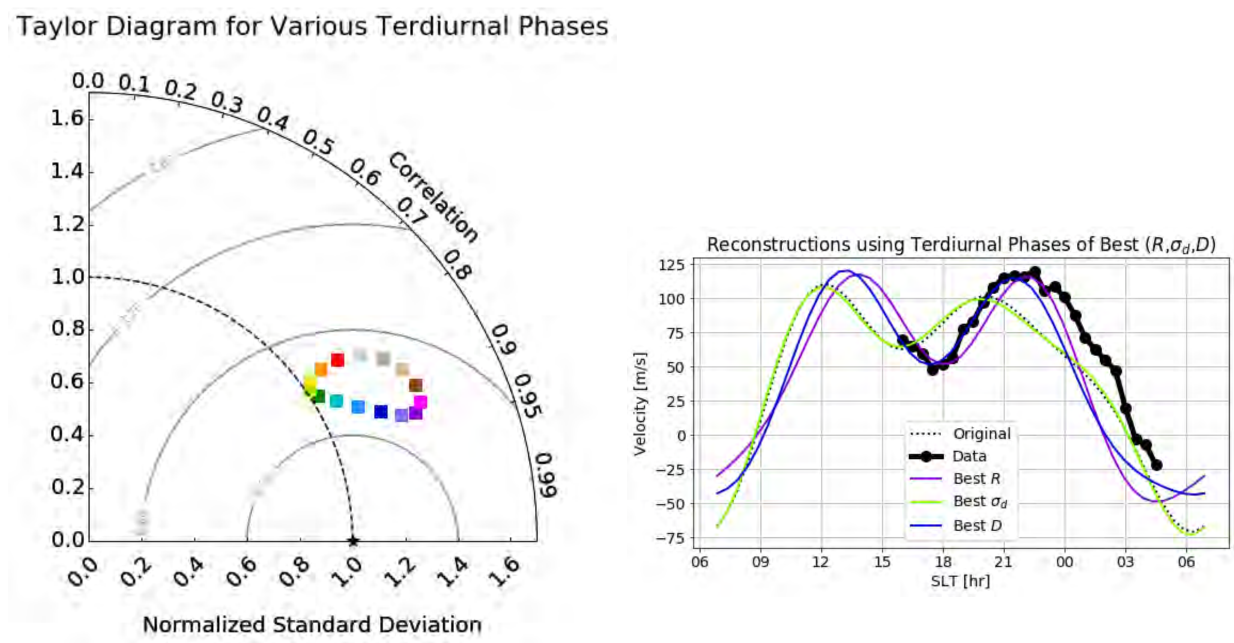

(a) (b)

Figure 4.7: Taylor diagram for various terdiurnal phases (left) and the reconstructions (right) corresponding to the best R_d (purple), σ_d (green) and D(blue) for February 2018.

The phase of the terdiurnal tide, γ_3 is shifted and the wind is then reconstructed (again, using equation 4.4). The phase shifts were stepped through and the reconstruction was compared to data by calculating the corresponding (s_d, R_d) and plotting each comparison on the Taylor diagram. An example is shown in Figure 4.7 (a). Each different hypothesized phase shift is shown by a different colour. Through this exercise, the phase shift that maximized correlation (R_d), matched the normalized standard deviation (s_d), or minimized RMSE (D) was identified.

Figure 4.7(b) shows an example of the reconstructed wind for February 2018. The results shown in purple, which maximized the correlation, is seen to match the data quite well in shape and amplitude at the peak. However, as the peak falls off after 21:00 SLT there is an amplitude difference between the model and the data (shown in black). The result shown in green point shows that the amplitude maximum matches the data fairly well and there is less of the amplitude discrepancy as the peak falls off than there is for the best correlation case, but the peak timing is quite different and remains almost identical to the original model output. Finally, the reconstruction corresponding to the phase that gives the smallest D (shown in blue) balances the correct peak timing and general shape from the best correlation case with the fall off behaviour influenced slightly by the best standard deviation case. Using D instead of just the correlation R helps to avoid cases where the best correlation case might result in a model output that is shifted so much that there is a large amplitude difference between model and data.

Table 4.1: RMSE of original HWM14, RMSE of terdiurnal tide shifted HWM14 and difference of the two for each month.

Months	D_{orig}	$D_{shifted}$	Improvements ($\Delta D = D_{orig} - D_{shifted}$)
Feb 2018	26.75	24.91	1.84
Mar 2018	30.60	16.39	14.21
Apr 2018	26.85	12.65	14.20
May 2018	19.58	14.92	4.66
Jun 2018	25.11	17.98	7.13
Jul 2018	31.00	19.08	11.92
Aug 2018	40.96	24.11	16.85
Sep 2018	41.73	19.27	22.46
Oct 2018	41.94	26.50	15.44
Nov 2018	31.93	9.04	22.89
Dec 2018	33.96	8.32	25.64
Jan 2019	43.27	10.42	32.85

Figure 4.8 clearly shows the improvements in data-model comparisons found by allowing for a phase shift in only the terdiurnal tidal component estimated from HWM14. Table 4.1 presents the comparison of RMSE of original HWM14 and RMSE of terdiurnal tide shifted HWM14 for each month that shows the improvements obtained from adjusting the terdiurnal

Figure 4.8: Improvement to HWM zonal wind for the entire year.

tide parameters in the model. It can be seen that during the local summer, i.e. February 2018, December 2018–January 2019, the improvements were between 1.84 and 32.85, while during local winter the improvements range from 7.13 to 16.85. The largest improvement of 32.85 was observed in January2019.

For all months, there was an improvement to both the standard deviation and the correlation of the original HWM14 output. Comparing the original and modified HWM14 wind results with the data, for almost all months, the modified HWM14 wind represents the data much more closely. In addition, the apparent phase shift between the peak wind in the data and HWM14 output has been greatly reduced as evident from results shown in Table 4.2. This table presents the phases of the original (first column) and shifted (second column) terdiurnal phases of the HWM14 zonal winds for each month. Shifting the terdiurnal phase is particularly effective for March–July, but in August–November the shift with the smallest

D results in shifting the predicted peak winds approximately an hour after the peak wind in the data. It also causes the peak amplitude to be overestimated, particularly in August and September, where it is overestimated by almost 30 m/s. It is also important to note that for February, shifting the terdiurnal tide was unsuccessful at correcting the apparent phase shift between data and HWM14, as evident from Figure 4.8. This indicates that there is still something that is not fully being captured with this simple three-sinusoid model. In future, adding additional terms onto this model may be necessary in order to correct the discrepancy that is still present between model and data. Still, the general conclusion is that the representation of the terdiurnal tide over South Africa in HWM14 does not appear to match the data presented here, indicating the importance of having well-distributed data in construction of such models.

Table 4.2: Phases of the original and shifted terdiurnal phases by month.

Months	Terdiurnal Phase$_{orig}$	Terdiurnal Phase$_{shifted}$	Δ Terdiurnal Phase
Feb 2018	2.77	8.00	5.23
Mar 2018	2.53	19.20	16.67
Apr 2018	2.21	17.60	15.39
May 2018	2.30	19.20	16.90
Jun 2018	2.55	19.20	16.65
Jul 2018	2.53	19.20	16.67
Aug 2018	2.12	19.20	17.08
Sep 2018	1.37	17.60	16.23
Oct 2018	0.95	17.60	16.65
Nov 2018	1.50	17.60	16.10
Dec 2018	2.30	17.60	15.30
Jan 2019	2.72	12.8	10.08

4.4 Summary

This work presents the first results of the study on the nighttime thermospheric neutral winds climatology over Sutherland, South Africa (i.e. midlatitude region) for a period between February 2018 and January 2019. The study was conducted using data during geomagnetically quiet conditions only, therefore only focusing on the effects of waves from below on the wind variability. Overall, the trend of the meridional wind shows predominantly annual, semiannual, and quasi-terannual variations of meridional wind where wind speed peaks in January, June, and September. However, only an annual variation for the zonal wind was observed. During local summer months (December–February), the meridional wind is predominantly equatorward, while the winter months show slower, poleward winds in th early evening. The peak of the equatorward wind and changes in the wind direction occur much earlier (premidnight) in the spring/autumn months compared to winter months (where they occur postmidnight). The equatorward summer and poleward winter winds are consistent with stronger heating in the summer hemisphere. In addition these seasonal observations are in line with observations made from other midlatitudes sites (e.g. Wu *et al.*, 2019).

This study also found that the zonal wind velocities are generally eastward during the evening just before midnight, and changed to westward post-midnight through to predawn. The eastward-to-westward transition time in the summer is between 01:30 SLT and 02:00 SLT, while the transition occurs much latter in the winter (between 04:00 and 05:30 SLT). Also, the magnitude of zonal wind is between ~ 90 and 120 m/s, consistent with observations from other sectors (e.g. Fejer *et al.*, 2002; Fisher *et al.*, 2015; Kaab *et al.*, 2017).

There was a better agreement between the FPI measured winds and the HWM14 predicted winds for the meridional component, and a particularly poor one for the zonal wind. Coupled with the relative lack of ground-based data from southern Africa being used in the construction of HWM14, it is not surprising, then, that the match between the data and model are not as good as in other sectors in which more ground-based data were available. For example, Fisher *et al.* (2015) reported similar phase shift in locations whose data were not in the formation of HWM14 when comparing HWM14 and the data, using Global High-resolution Thermospheric Imaging (MIGHTI) in different sectors. The cause of the difference between data and model observed in this study was investigated and determined to be the result of a difference in phase shift of the terdiurnal tide.

Chapter 5

Ionosonde derived neutral meridional wind

Since ionosondes are more prolific with wider temporal and spatial coverage than FPIs, many techniques have been developed to calculate meridional wind from their measure of the ionospheric F2 peak height (hmF2) (Buonsanto *et al.*, 1989; Buonsanto *et al.*, 1997; Miller *et al.*, 1986; Dyson *et al.*, 1997; Fagundes *et al.*, 2008; Muella *et al.*, 2008; Dandenault, 2018). This chapter presents meridional wind derived using hmF2 data obtained from the South African ionosonde network. The derivation is based on the servo model and validated using an FPI. The results are also compared to the widely used horizontal wind model (HWM14), and the Magnetic mEridional NeuTrAl Thermospheric (MENTAT) that was developed using historic ionosonde data including data from our region of interest. The comparison to the HWM14 and MENTAT is done to benchmark the performance of this technique since none of the ionosonde stations are co-located with the FPI. Taylor diagrams are again used to determine the model with the best agreement to the measurements.

5.1 Atmospheric models

This section provides descriptions of different atmospheric empirical models used in the derivations of meridional neutral wind.

5.1.1 Mass-Spectrometer-Incoherent-Scatter (MSIS)

The mass-spectrometer-incoherent-scatter (MSIS) model is an empirical global atmospheric model that describes the neutral temperature and densities in the upper atmosphere (above about 100 km) created by Hedin *et al.* (1988). The newest available version of MSIS is NRLMSISE-00 which is an improvement of the previous models, i.e. MSIS-86 and MSIS-90 (Picone *et al.*, 2002). The construction of NRLMSISE-00 used total mass density measurements from satellite accelerometers, temperature data from incoherent scatter radar covering a period of 1981–1997, and molecular oxygen number density measurements from solar UV occultation (Picone *et al.*, 2002). MSIS model input includes time and date, altitude, geographical location, local time, 81 day average F10.7 values, daily F10.7 from the previous day and daily magnetic index. Model outputs include, but are not limited to, neutral densities of O, O_2 and N_2 as well as neutral temperature (T_n). These parameters were extensively used in this study in servo the model.

5.1.2 The International Reference Ionosphere (IRI)

The international reference ionosphere (IRI) model is an empirical global model that provides different ionospheric parameters such as electron density, electron temperature, ion temperature, ion composition, ion drift, and ionospheric electron content (TEC) as a function of geographic location, date, time and altitude (Rawer *et al.*, 1978). The major data sources for this model are the incoherent scatter radars, topside sounders and in situ instruments on several satellite and rockets (Rawer *et al.*, 1978; Bilitza, 1993). Several steadily improved editions of the model have been released with the latest being IRI-2016 (Bilitza *et al.*, 2017). The input parameters includes solar indices, magnetic index, date, and geographical location. The main application of IRI in this thesis is to provide electron and ion temperatures for the servo model.

5.1.3 International Geomagnetic Reference Field (IGRF)

The international geomagnetic reference field (IGRF) is an internationally widely used empirical model of the Earths magnetic field of internal origin and its secular variation (Zmuda, 1971). Although the model was developed in the 1960s, there have been several updates on the model with the latest version released in 2014, called IGRF-12 (Mandea & Macmillan, 2000; Macmillan & Finlay, 2011). The negative gradient of a scalar potential V_i (r, θ, ϕ, t) is the main field which satisfies the Laplace's equation. This model has a set of spherical harmonics, of which is a solution to the Laplaces equation:

$$V_i(r,\theta,\phi,t) = a\sum_{n=1}^{N}\sum_{m=0}^{n}\left(\frac{a}{r}\right)^{n+1}\left(g_n^m(t)cos(m\phi) + h_n^m(t)sin(m\phi)\right)P_n^m cos(\theta), \tag{5.1}$$

where $a = 6371.2$ km is the mean radius of the Earth, r denotes the radial distance from the centre of the Earth, θ represent the geocentric colatitude, ϕ denotes the east longitude, t is the time, $P_n^m cos(\theta)$ are the Schmidt-normalized associated Legendre functions of degree n and order m, $g_n^m(t)$ and $h_n^m(t)$ are the corresponding Gauss coefficients. The IGRF model provides magnetic field parameters such as magnetic dip angle, magnetic inclination, dipole moment, etc. The input parameters includes solar indices, magnetic index, date, and geographical location. The only application of IGRF model in this research is to provide magnetic dip angle estimates required for the servo model.

5.1.4 MENTAT model

The MENTAT model is based on the Field Line Interhemispheric Plasma (FLIP) model, which ingests ionosonde data and uses krigging for data interpolation. A global database of ionosonde hmF2 observations between the period of 1961–1990 was used to develop a this model. This database included hmF2 measurements over South Africa, a region of interest in current study. Dandenault (2018) calculated magnetic meridional thermospheric neutral winds using the equation given by:

$$U(t + \Delta t) = \frac{hmF2(t + \Delta t) - h'(t)}{\alpha(t)} + U'(t), \tag{5.2}$$

where $h'(t)$ is a calculated height of the F2 layer, $\alpha(t)$ is the constant for small time steps and $U(t)$ is the equivalent neutral wind at time t.

5.2 Data Analysis

The period of the study presented here is February 2018 to July 2019, chosen to coincide with FPI data availability. However, the ionosondes don't all have data throughout this period, therefore Table 5.1 shows the summary of each ionosonde's data availability as well as their distances from the FPI using Haversine formula (Dauni *et al.*, 2019). In general, there is at least 80% ionosonde and FPI data availability for each month. It is important to note that the 10 months data availability over Madimbo covered the following periods: March–June 2018, December 2018, January–February 2019, and July 2019.

Table 5.1: Summary of period of study and their proximity to the FPI stations

Stations	Period of study	Number of Months	Distance from the FPI (km)
Hermanus	Feb 2018–Jan 2019	12	282
Grahamstown	Jul 2018–Jun 2019	12	535
Louisvale	Jul 2018–Dec 2018	6	434
Madimbo	Mar 2018–Jul 2019	10	1477

The period of study covers low solar activity phase of the solar cycle, with solar flux F10.7 ranging between 67 and 74 sfu, and the geomagnetic conditions are quiet, with the monthly averaged Ap and Kp indices in the ranges of 5.50–9.45, and 1.2–1.9, respectively as shown in Table 5.2.

In this study the $[O]$ has been increased by 20% while $[N_2]$ and $[O_2]$ have been multiplied by a factor of 8 to account for the uncertainties in the neutral densities as suggested by Buonsanto *et al.* (1989) and Dyson *et al.* (1997). These adjustments in the neutral densities reduced the

Table 5.2: Number of nights where the FPI and ionosonde data are available in each month, average Kp, Ap and F10.7

Months	Nights	Kp index	Ap index	F10.7
Feb 2018	23	1.5	6.88	70.0
Mar 2018	26	1.5	7.41	67.6
Apr 2018	28	1.4	7.07	70.6
May 2018	29	1.4	7.28	72.5
Jun 2018	26	1.5	7.18	74.9
Jul 2018	30	1.3	5.50	72.0
Aug 2018	27	1.4	6.01	70.0
Sep 2018	24	1.9	9.45	69.0
Oct 2018	28	1.3	6.30	69.0
Nov 2018	26	1.2	5.96	67.5
Dec 2018	26	1.2	5.62	67.7
Jan 2019	31	1.3	6.77	68.3
Feb 2019	28	1.2	5.77	67.4
Mar 2019	29	1.3	6.75	68.5
Apr 2019	28	1.4	6.74	69.6
May 2019	31	1.2	7.37	67.8
Jun 2019	29	1.3	6.47	67.2
Jul 2019	30	1.3	6.56	70.2

magnitude of the equatorward wind and was found to lead to a better agreement with the measurements. Dalgarno (1964) suggested that the Burside factor f, found in equation 3.43, should be 1. However, a value of 1.7-2.0 is suggested by latter studies (e.g. Buonsanto *et al.*, 1989; Salah, 1993), while others have recommended that this factor should be decreased between 1.0 and 1.3 (e.g. Pesnell *et al.*, 1993; Reddy *et al.*, 1994; Buonsanto *et al.*, 1997; Fagundes *et al.*, 2008; Dandenault, 2018), and Dyson *et al.* (1997) suggested that this factor should be increased to 2.0 for the midlatitude. This work adopts the suggestion by Dyson *et al.* (1997) as it was observed that using a small Burside factor results in large equatorward wind when the diffusion is more important.

5.3 Results

Figures 5.1–5.4 present meridional wind derived using the servo model (blue), MENTAT (magenta), and HWM14 (green) over Hermanus, Grahamstown, Madimbo, and Louisvale, respectively. Superposed on these figures is the measured meridional wind from the Sutherland FPI, which has been rotated along the magnetic meridian to match the ionosonde by multiplying the FPI data with cosine of the magnetic declination angle of the FPI site. Note that data from different ionosonde stations were available in different months during the period of this study as presented in Table 5.1. Therefore the months are not consistent throughout all the stations.

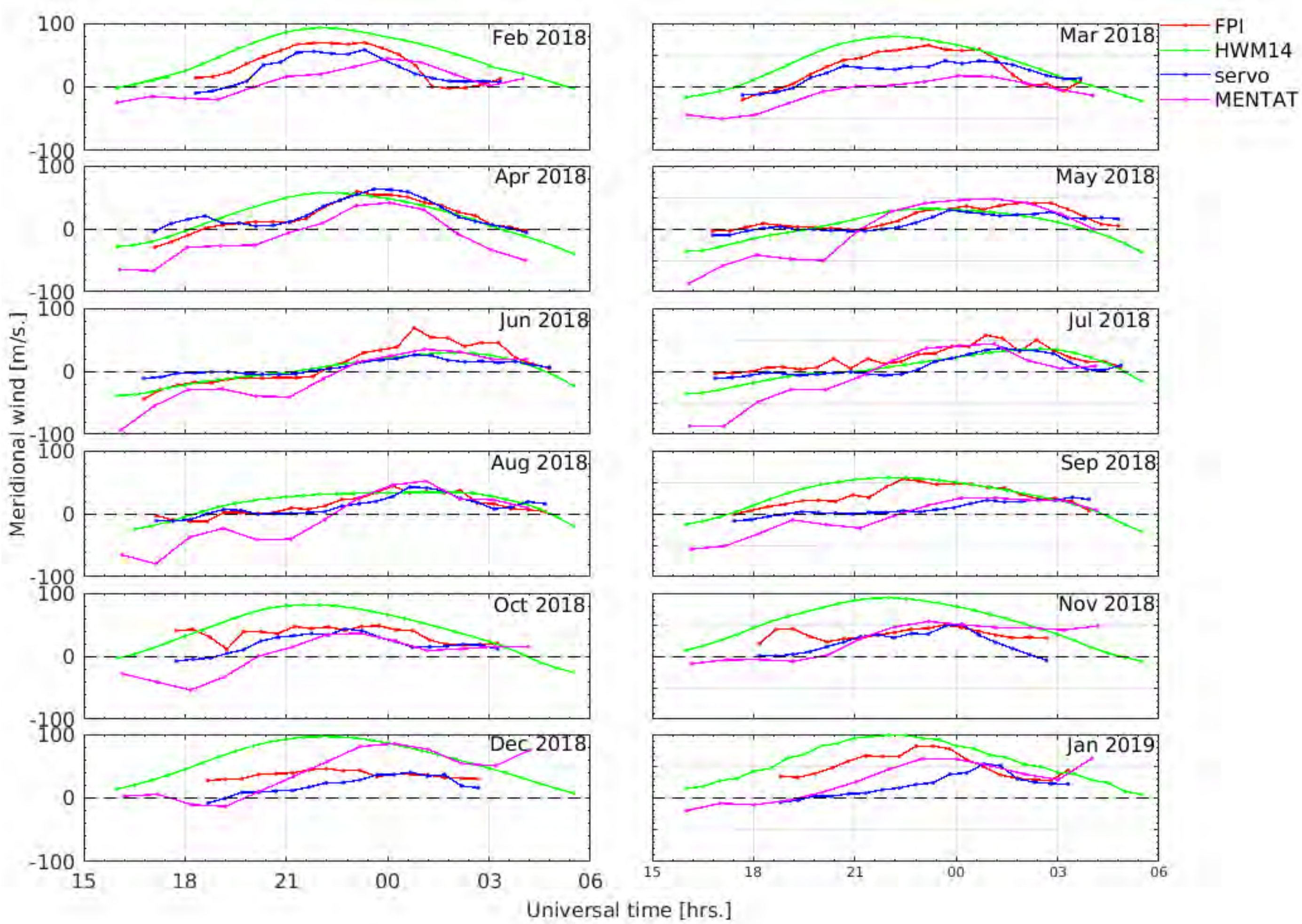

Figure 5.1: Monthly averaged meridional wind derived using the servo model (blue), MENTAT model (magenta), HWM14 model (green) and measured by FPI (red) during the period of February 2018–January 2019 over Hermanus.

As illustrated in Figure 5.1 for the Hermanus ionosonde station, the servo model follows FPI measured wind very closely, including matching the wind peak for most months, especially in April, May, and August, whereas HWM14 and MENTAT models largely underestimated and/or overestimated the wind. In particular, the servo model correctly projected post-sunset poleward wind (e.g. March, May and August) and mostly/entirely equatorward wind throughout the night (e.g. October–December 2018). In addition, the servo model matched observation in predicting the poleward-to-equatorward transition observed around 18:00-19:00 UT in March, May, and August, whereas in HWM14 and MENTAT this occurred a bit latter, at around 18:00 UT-22:00 UT. However, in some of these months, especially in February, March, September, December, and January, the servo model largely underestimated the wind by as much as 20 m/s. In comparison during the same period, HWM14 and MENTAT also mostly underestimate/overestimate the amplitude of the meridional wind, by $\sim$ 30 m/s and $\sim$ 20 m/s respectively.

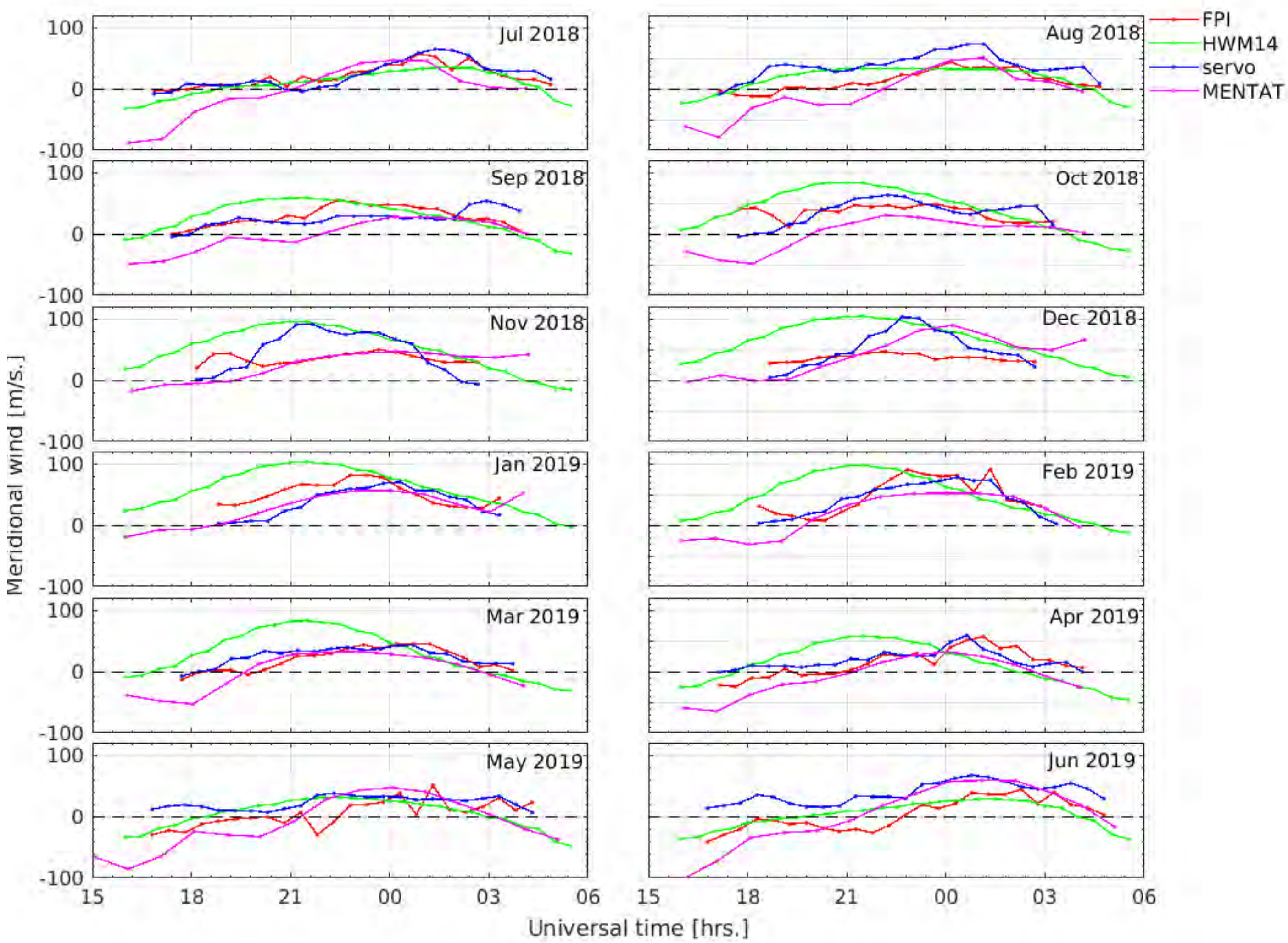

Figure 5.2: Monthly averaged meridional wind derived using the servo model (blue), MENTAT model (magenta), HWM14 model (green) and measured by FPI (red) during the period of July 2018–June 2019 over Grahamstown.

Figure 5.2 presents the results obtained from the Grahamstown ionosonde station. The servo model largely matches the measured wind variability and accurately estimated an equatorward wind throughout the night in August–March, but overestimates the meridional winds

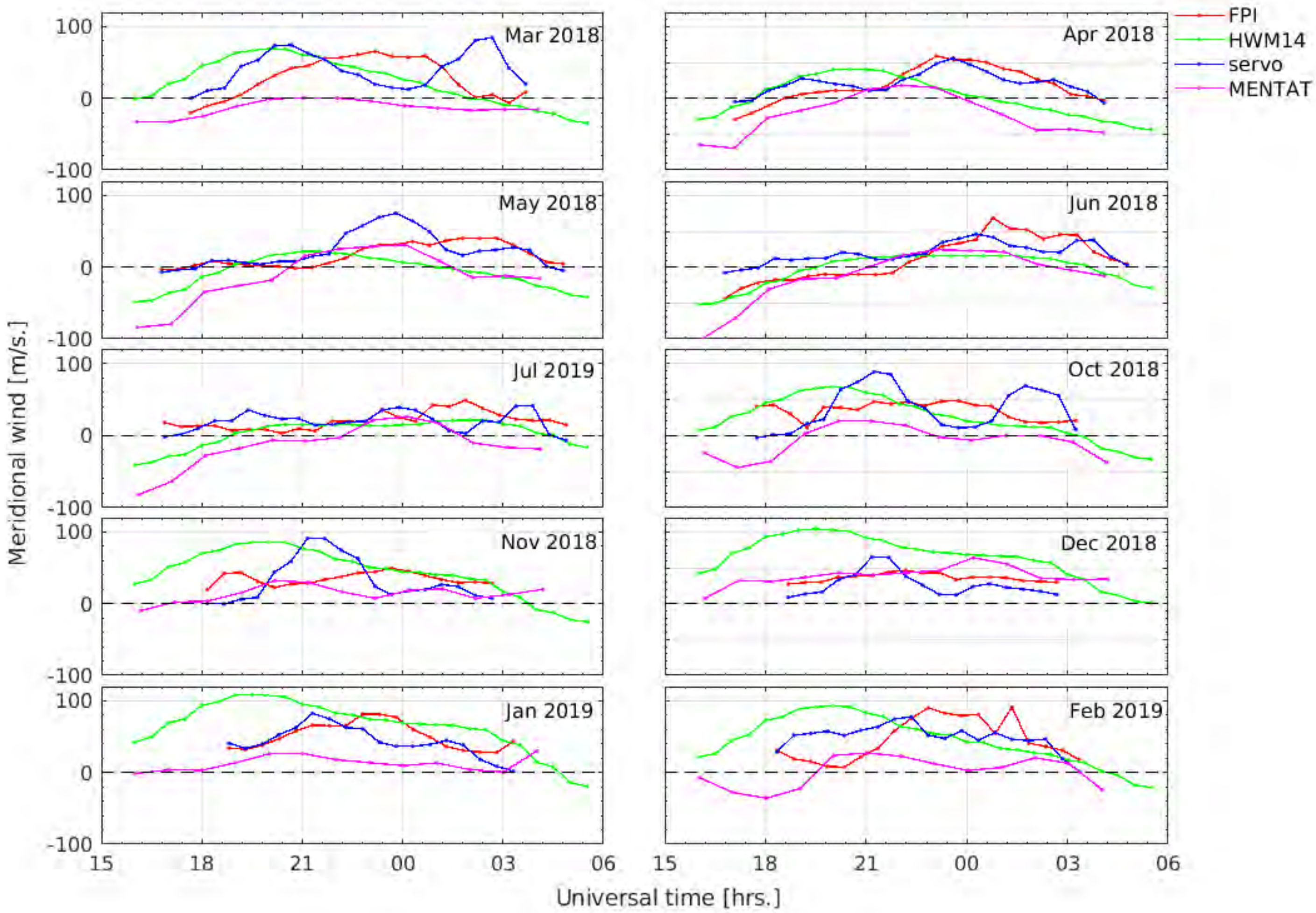

Figure 5.3: Monthly averaged meridional wind derived using the servo model (blue), MENTAT model (magenta), HWM14 model (green) and measured by FPI (red) during the period of March 2018–February 2019 over Madimbo.

by as much as ∼25 m/s in November–December, while the HWM14 and MENTAT models over/under estimates by only ∼10 m/s during the similar period. While the servo model inaccurately shows equatorward throughout April–June, HWM14 and MENTAT models correctly predict winds that transition from poleward to equatorward but with inaccuarate transition times, e.g. they transition by as much as 2-3 hours early in June.

Figure 5.3 shows that over Madimbo the servo model reproduces a predominant meridional equatorward wind for the entire nights in May, July, and October–February similar to the measured data but incorrectly projects an equatorward wind in March–April and June. However, this model inaccurately overestimates the peak and amplitude of the meridional wind by $\sim$ 20 m/s at around 18:00–00:00 UT in May, October, and November. In addition, the peak of the equatorward wind occurs $\sim$ 2 hours earlier in the servo model than in measured data. The HWM14 and MENTAT correctly projects poleward winds from 18:00-22:00 UT in April and June. The poleward-to-equatorward transition occurs at almost the same time as in the measured data in this period. However, the HWM14 and MENTAT models inaccurately predict a poleward wind in July–October, while in November–January, the predicted wind matches the measured data. The servo model mostly overestimate the amplitude of the meridional wind by $\sim$10 m/s in this period. HWM14 and MENTAT mostly overestimate/underestimate the amplitude of the meridional wind by $\sim$ 20 m/s and $\sim$ 10 m/s, respectively, for example in May–February.

Figure 5.4 shows that although the servo model using Louisvale ionosonde data correctly exhibits a predominantly equatorward wind seen by the FPI, the model's wind amplitudes are inaccurate. For example, the wind peak is overestimated by about 15–20 m/s in most months except September when it is underestimated by $\sim$20–25 m/s. Furthermore, the model also underestimates the poleward to equatorward wind transition time by about 2 hours from FPI transition in August. In contrast, the HWM14 also shows a predominant equatorward wind for most of the months, except July, but largely overestimates the wind amplitudes by as much as 25 m/s. Also, the MENTAT model only correctly predicts a predominant equatorward wind in December and mostly underestimates the wind amplitude by as much as 15 m/s. Furthermore, the MENTAT overestimated the poleward to equatorward wind transition time seen in FPI data in July and August by about 3 hours, while the HWM 14 overestimated it by $\sim$ 2 hours in July and underestimated it by $\sim$ 2 hours in August.

Figures 5.5–5.8 present Taylor diagrams for each of the ionosondes stations and Table 5.3 indicates the model with the best agreement in different seasons and per station. Note that the model with the best agreement with measurements mostly fulfils these three criteria: have strong-to-very strong correlation coefficient (i.e. mostly R is 0.6–0.90), low root mean square error, and the normalized standard deviation close to 1.

The meridional wind derived using the servo model yielded the best agreement to the measurements in February, April, May, July, August, October and November over Hermanus as shown in Figure 5.5. On the other hand, the HWM14 model produced the best agreement in March, June, September, December and January. The model that performed the worst was the MENTAT model, as it yielded high RMSE and not close to the reference data, although it has high correlation coefficient in some of the months, e.g., May. Overall the servo model showed the best performance in 58% of the months, while HWM14 did similarly in 42% of the months.

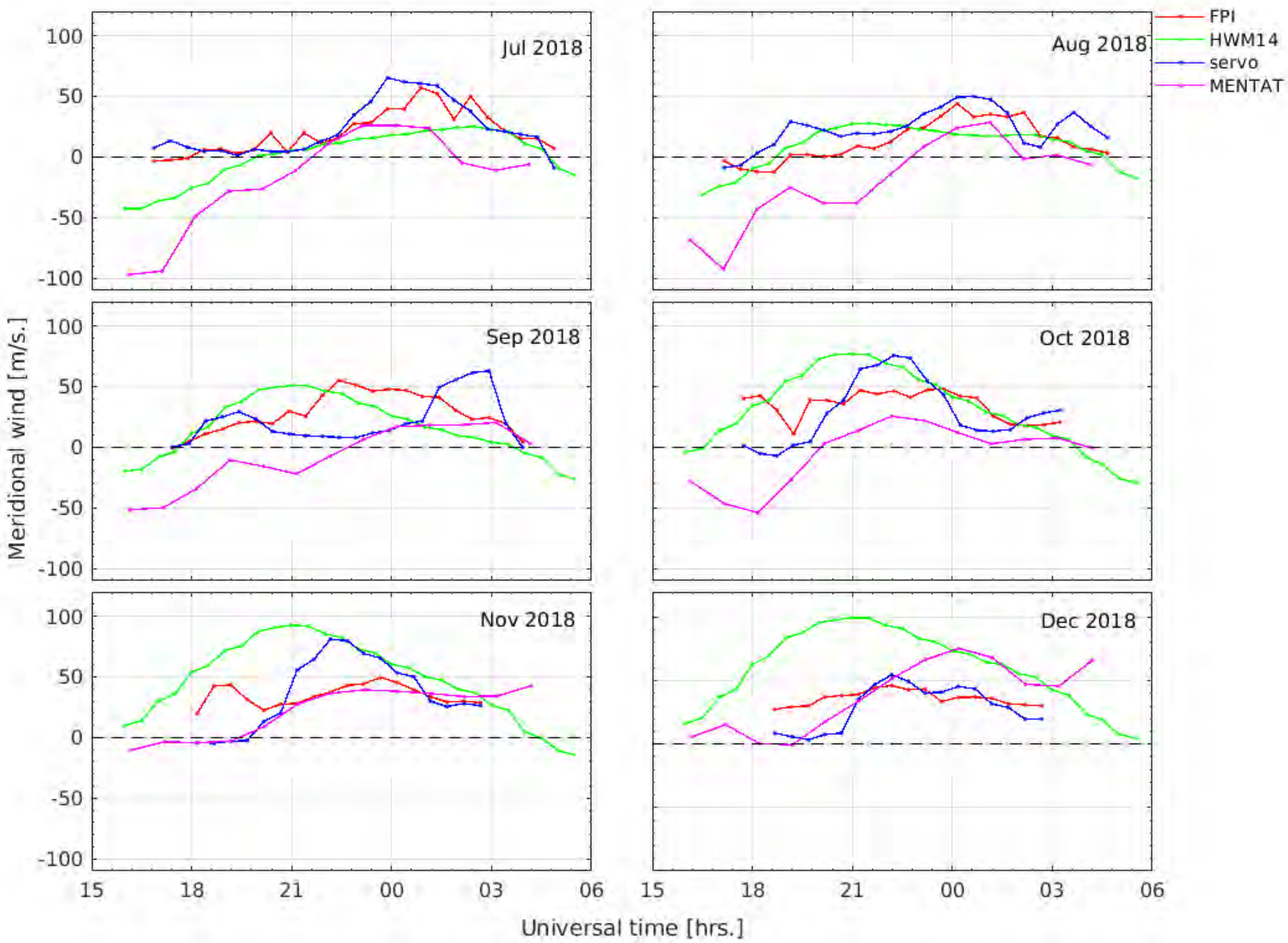

Figure 5.4: Monthly averaged meridional wind derived using the servo model (blue), MENTAT model (magenta), HWM14 model (green) and measured by FPI over Louisvale during the period of July–December 2018 over Louisvale.

Figure 5.6 shows that the meridional wind derived using the HWM14 model yield the best agreement with the FPI measurements in July, August, September, October, December, and January over Grahamstown. In addition, the servo model had the best agreement with observations in February, March, April, and May, while the MENTAT model had the best agreement in only November. This means that in general HWM14 predictions were most accurate compared to the other models in 58% of the months, while the servo and MENTAT models in 33% and 8% of the months, respectively.

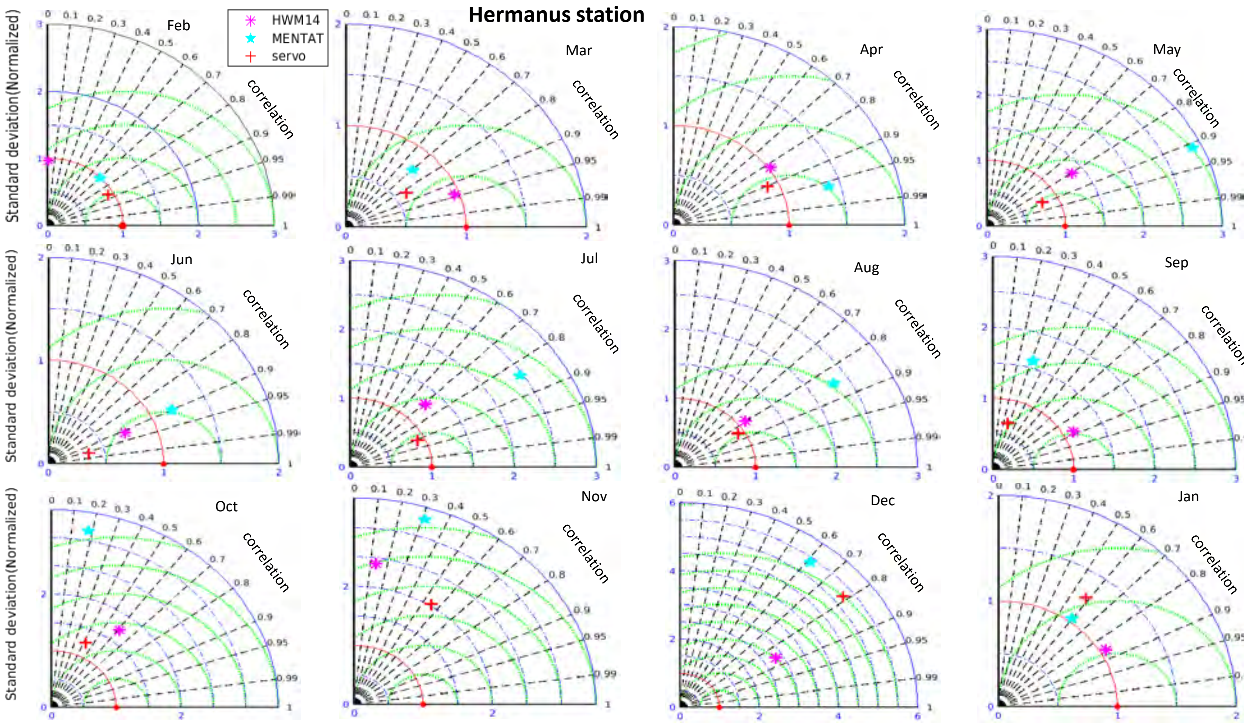

Figure 5.5: Taylor diagram showing performance of servo (red cross), MENTAT (cyan star) and HWM14 model (magenta asterisk) over Hermanus during the period of February 2018-January 2019.

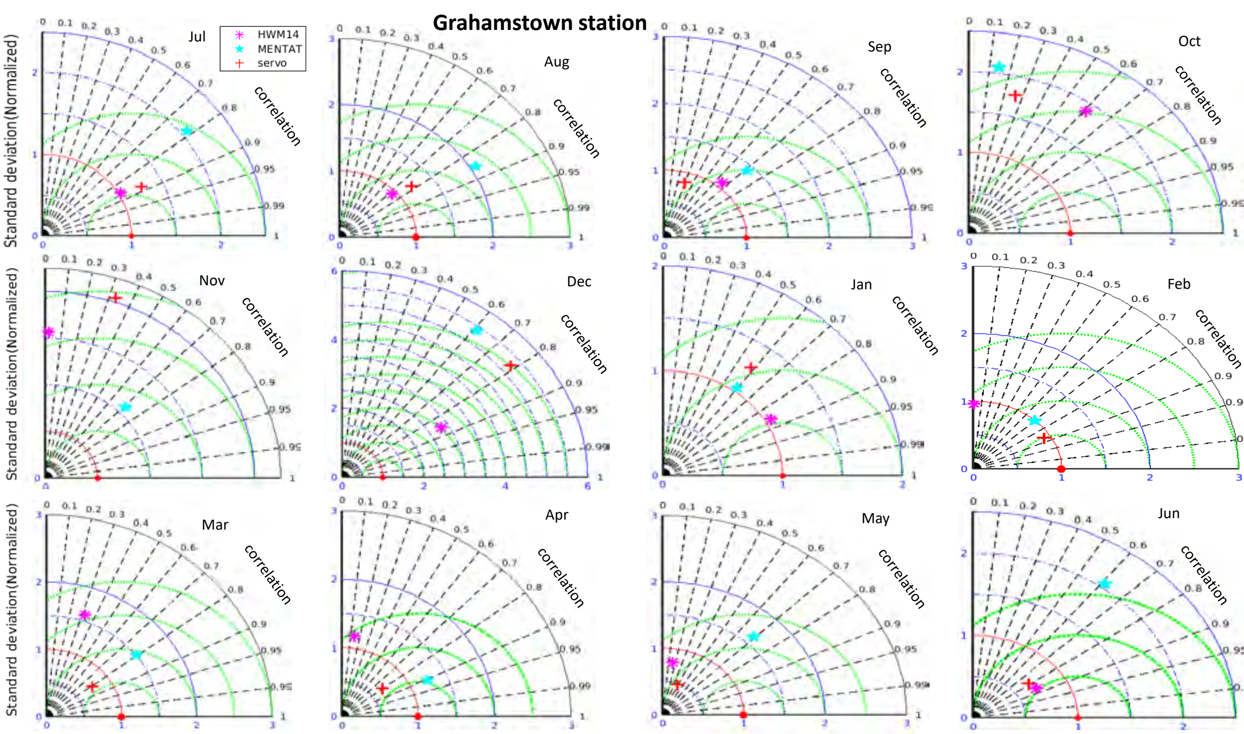

Figure 5.6: Taylor diagram showing performance of servo (red cross), MENTAT (cyan star) and HWM14 model (magenta asterisk) over Grahamstown during the period of July 2018-June 2019.

Table 5.3: Different models agreement according to Taylor diagram per month and stations.

Stations	Months	servo model	MENTAT model	HWM14
	Feb 2018	Best agreement	-	-
	Mar 2018	-	-	Best agreement
	Apr 2018	Best agreement	-	-
	May 2018	Best agreement	-	-
	Jun 2018	-	-	Best agreement
Hermanus	Jul 2018	Best agreement	-	-
	Aug 2018	Best agreement	-	-
	Sep 2018	-	-	Best agreement
	Oct 2018	Best agreement	-	-
	Nov 2018	Best agreement	-	-
	Dec 2018	-	-	Best agreement
	Jan 2019	-	-	Best agreement
	Jul 2018	-	-	Best agreement
	Aug 2018	-	-	Best agreement
	Sep 2018	-	-	Best agreement
	Oct 2018	-	-	Best agreement
	Nov 2018	-	Best agreement	-
Grahamstown	Dec 2018	-	-	Best agreement
	Jan 2019	-	-	Best agreement
	Feb 2019	Best agreement	-	-
	Mar 2019	Best agreement	-	-
	Apr 2019	Best agreement	-	-
	May 2019	Best agreement	-	-
	Jun 2019	-	-	Best agreement
	Mar 2018	Best agreement	-	-
	Apr 2018	Best agreement	-	-
	May 2018	Best agreement	-	-
	Jun 2018	-	Best agreement	-
Madimbo	Oct 2018	-	Best agreement	-
	Nov 2018	-	Best agreement	-
	Dec 2018	-	Best agreement	-
	Jan 2019	Best agreement	-	-
	Feb 2019		-	Best agreement
	Jul 2019	-	-	Best agreement
	Jul 2018	Best agreement	-	
	Aug 2018	-	-	Best agreement
	Sep 2018	-	-	Best agreement
Louisvale	Oct 2018	-	-	Best agreement
	Nov 2018	-	Best agreement	-
	Dec 2018	Best agreement	-	-

The meridional wind derived using the servo model yielded the best agreement to the measurements in March, April, May, and January over Madimbo as shown in Figure 5.7. Similarly, the MENTAT model matched the same level of agreement with the servo model at this same station with the best agreement in June, October, November, and December. On the other hand, the HWM14 model produced the best agreement in July and February, this model performed worst over this station. Overall the servo model and MENTAT showed the best performance in 40% of the months, while HWM14 has the best performance in 20% of the months.

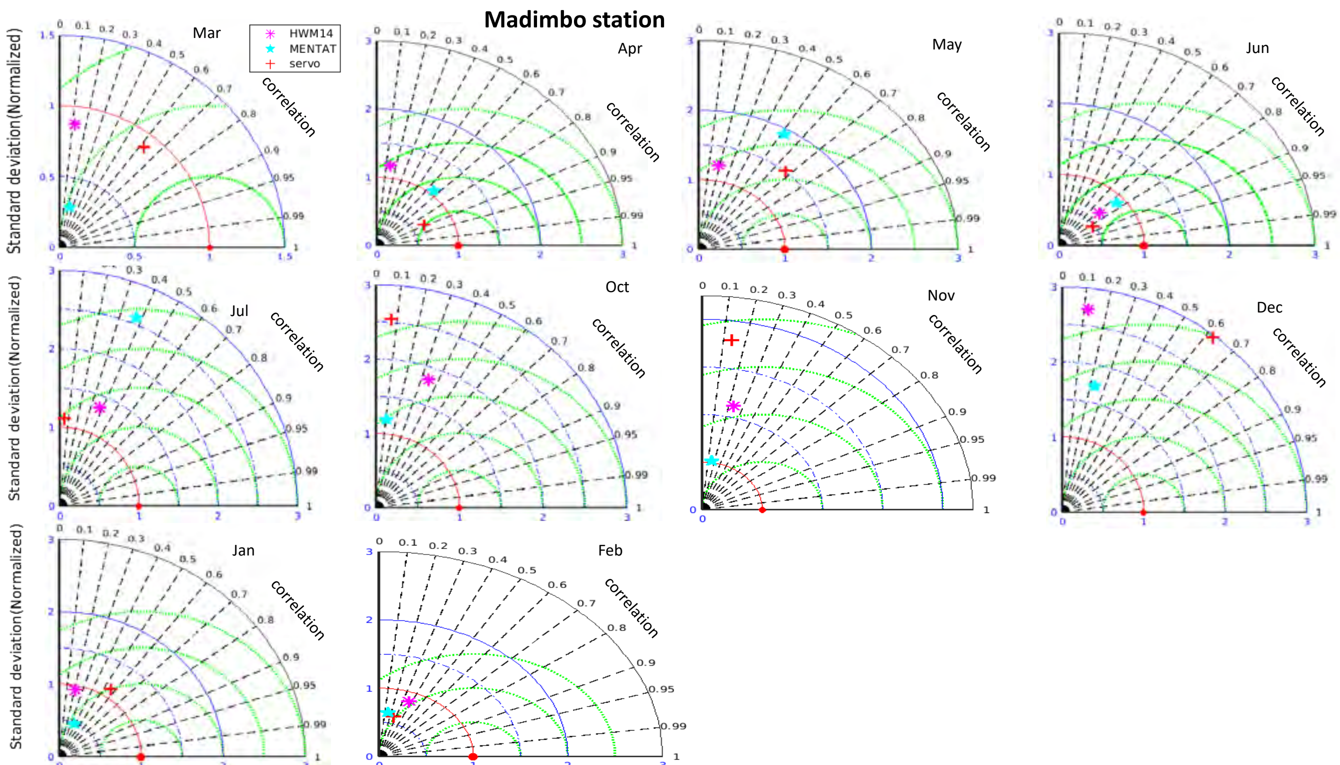

Figure 5.7: Taylor diagram showing performance of servo (red cross), MENTAT (cyan star) and HWM14 model (magenta asterisk) over Madimbo during the period of March 2018–July 2019.

Figure 5.8 shows that the meridional wind derived using the HWM14 model yield the best agreement with the FPI measurements in August, September, and October over Louisvale. In addition, the servo model had the best agreement with observations in July and December while the MENTAT model had the best agreement in only November. In general HWM14 predictions were most accurate compared to the other models in 50% of the months, while the servo and MENTAT models in 33% and 17% of the months, respectively.

5.4 Discussion

The ability to accurately estimate the thermospheric wind is important for accurate modeling of the ionosphere, to better explicate ionospheric and thermospheric phenomena related to

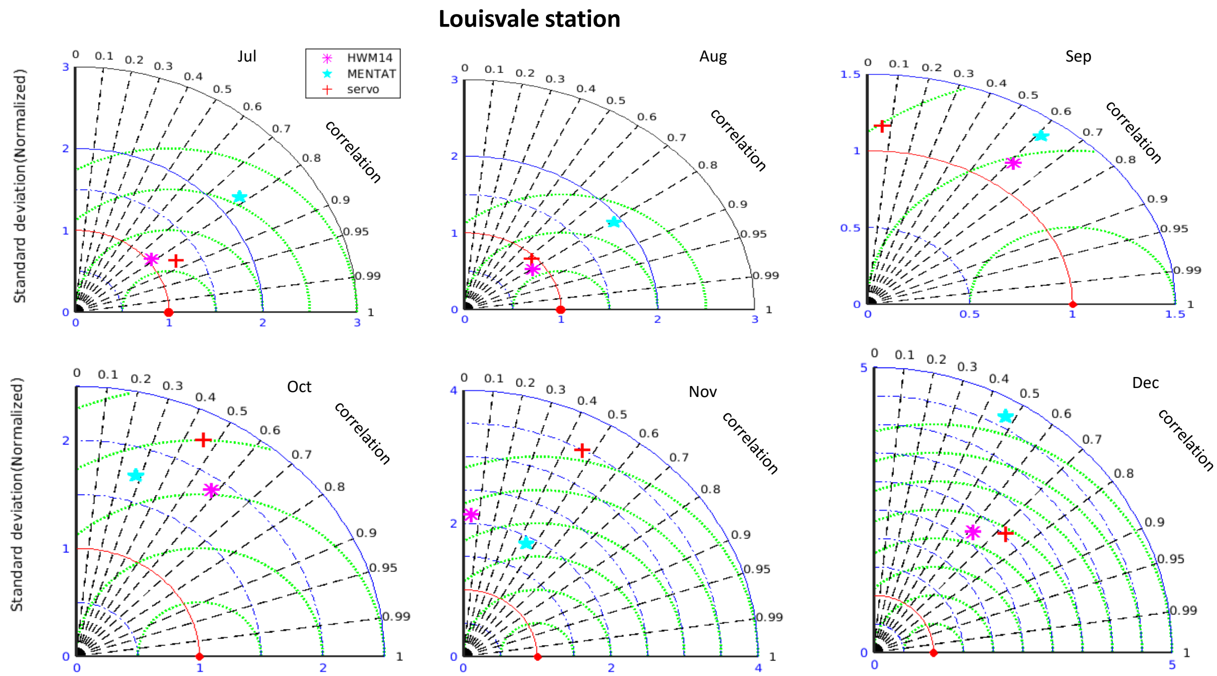

Figure 5.8: Taylor diagram showing performance of servo (red cross), MENTAT (cyan star) and HWM14 model (magenta asterisk) over Louisvale during the period of July-December 2018.

the neutral winds, and for an improved understanding of thermospheric dynamics. This study has found a good agreement between the ionosonde derived meridional wind using the servo method and FPI measured wind, although there are some discrepancies which vary per models, stations, and seasons. This finding is in agreement with other studies of meridional wind derived from ionosonde using similar principles (e.g. Miller *et al.*, 1986; Titheridge, 1995a; Buonsanto *et al.*, 1997; Dyson *et al.*, 1997; Liu *et al.*, 2003; Muella *et al.*, 2008). Both servo and HWM14 showed equatorward wind from dusk to dawn during the local summer months as observed in the FPI measurements consistent with previous works (e.g. Titheridge, 1995a; Fisher *et al.*, 2015; Kaab *et al.*, 2017). However, the MENTAT model failed to reproduce an equatorward wind observed during the summer months over this region, this finding contradicts what was previously reported by Dandenault (2018). At midlatitudes, as shown in Figures 5.1–5.4 across the ionosonde stations, the meridional neutral wind has a general pattern of equatorward motion around midnight hours in agreement similar studies (e.g. Buonsanto *et al.*, 1989; Titheridge, 1995a; Titheridge, 1995b; Dandenault, 2018).

The servo model was observed to sometimes wrongly overestimate/underestimate the meridional winds around dawn (sunrise) in some months across the stations. This inaccuracy at around the dawn of the servo model may be explained by the large upward O^+ flux in the topside shifting the zero-wind F-peak downward from the balanced height or equilibrium level where recombination and diffusion are of equal importance (Titheridge, 1995a; Titheridge, 1995b). Remarkably, the servo model's inaccuracy was also noticed by previous studies (e.g. Buonsanto *et al.*, 1989; Dowdy, 1993; Titheridge, 1995a; Titheridge, 1995b; Buonsanto *et al.*, 1997; Fagundes *et al.*, 1997; Dandenault, 2018).

This research found that ionosonde sites closer to the location of the FPI produce better estimates of servo wind than stations further away. For example, the Hermanus ionosonde, which is closest to the FPI location, has the best agreements across models, followed by the Louisvale ionosonde station, while it was observed that models using data from Madimbo, the farthest distance to the FPI, have large discrepancies with the observations. Furthermore, it is expected that empirical models which incorporated local ionosondes data during their development will perform better in those regions. This is somewhat supported by the results of this study which showed that the servo and MENTAT models, which used local data, yielded best agreements with observations in 2 and 1 stations, respectively, out of 4 stations. However, contrary to this the HWM14, which hardly has local data representation, also yielded the best agreement in 2 out of 4 stations.

Some of the inaccuracies of the servo model may be driven by the quality of the input data. For example, a low hmF2 will be incorrectly interpreted as the effect of poleward wind, when the peak in the altitude distribution of O^+ is higher than the F2 layer peak height (Buonsanto, 1990; Buonsanto *et al.*, 1997). In addition, it should be noted that the MSISE, IRI, and IGRF models that provide the neutral densities, temperatures, and magnetic dip angle, respectively, have less ground-based data in the Southern Hemisphere in their developments. These models are accompanied with some uncertainties, and these may have some effect in the servo model's derivation of meridional neutral winds. These uncertainties have been reported in previous studies (e.g. Buonsanto *et al.*, 1997; Dyson *et al.*, 1997, Buonsanto *et al.*, 1989; Luan & Solomon, 2008). In addition, the discrepancies observed in the servo model could also be due to the altitude difference between hmF2 ($\sim$200–300 km) and peak height of the 630.0 nm airglow emission measured by the FPI (assumed to be $\sim$250 km), which will be exacerbated if there are any strong altitude gradients (Dandenault, 2018). Also, airglow contamination of the 630.0 nm from mesospheric OH emission can affect the accuracy of the measured meridional winds and this may contribute to the discrepancy between servo and measured winds (Burnside & Tepley, 1990; Mende *et al.*, 1993; Dandenault, 2018).

5.5 Summary

Meridional wind derived from hmF2 measurements by the South African midlatitude ionosondes was presented. The derivation was based on the servo model and the wind results were validated using FPI measurements and benchmarked with global models, i.e. HWM14 and MENTAT. The servo model was found to reasonably predict accurate trends of winds when compared to the FPI, especially during the summer and early winter months. It was also found to yield the best agreement to the observed winds in 2 stations (Hermanus and Madimbo), similar to the HWM14 (but in Grahamstown and Louisvale), but MENTAT only did so in 1 station (also Madimbo). Furthermore, results presented here showed that the ionosonde station closest to the FPI location (i.e. Hermanus) has better wind projection with the observed data compared to the ionosonde stations that are located farther.

Chapter 6

Tidal variability in thermospheric winds

This chapter presents the extraction and analysis of atmospheric tides, namely the diurnal, semidiurnal, and terdiurnal components, from a year of quiet-time FPI observations over Sutherland, South Africa. The goal of this study is to investigate the long-term tidal winds variations from the thermospheric wind measurements obtained from the FPI by determining which tidal component(s) dominate(s) during different seasons. This is important because the contribution of tides to the wind has been shown to influence the thermospheric temperature structure. For example, the midnight temperature maximum (MTM) results from the semi-diurnal tide generating convergence in thermospheric winds (Meriwether, 2006).

Since spectral analysis provides the road map to determine the dominant oscillation modes, it was applied to the FPI wind measurements to determine the periodicities of the wind's cyclical variations. Most of the spectral analysis techniques require a uniformly sampled time series, e.g. Fourier transform (FT) and wavelet analysis. However, data obtained from FPIs are often unevenly spaced in time, either due to the nature of the instrument's operation or data gaps, necessitating the use of Lomb Scargle analysis in determining dominant tidal frequencies/periods throughout the year. This method is preferred over the fast Fourier transform because it minimizes the addition of spectral information created when interpolating to fill in data gaps.

Lomb-Scargle is a well-known algorithm for detecting and characterizing periodicity in unevenly sampled time-series (Press & Rybicki, 1989; Hernandez *et al.*, 1993; Oznovich *et al.*, 1997; Fisher *et al.*, 1999; Fisher *et al.*, 2002; Fisher, 2017). The Lomb-Scargle analysis also provides estimates of the significant height of a spectral peak. Lomb (1976) and Scargle (1982) defined the Lomb-Scargle periodogram for N observations of x_k, taken at times t_k, where $k = 1, ..., N$, as:

$$P_{LS}(f) = \frac{1}{2\sigma^2}\left\{\frac{\left[\sum_{k=1}^{N}(x_k-\overline{x})cos(2\pi f(t_k-\tau))\right]^2}{\sum_{k=1}^{N}cos^2(2\pi f(t_k-\tau))}+\frac{\left[\sum_{k=1}^{N}(x_k-\overline{x})sin(2\pi f(t_k-\tau))\right]^2}{\sum_{k=1}^{N}sin^2(2\pi f(t_k-\tau))}\right\}, \tag{6.1}$$

where $\overline{x}$ is the mean, and σ^2 is the variance of the data. The time offset, τ, is given by:

$$tan(2(2\pi f)\tau) = \frac{\sum_{k=1}^{N}sin(2(2\pi f)t_k)}{\sum_{k=1}^{N}cos(2(2\pi f)t_k)}. \tag{6.2}$$

The Lomb Scargle analysis was performed by using a MATLAB function, and returns the Lomb-Scargle power spectral density (PSD) estimate of a data that is sampled at the instants specified in time (Press & Rybicki, 1989; Horne & Baliunas, 1986). It should be noted that time must be positive and increase monotonically even if its not uniformly spaced.

6.1 Results

This section presents the power spectral density results for the FPI measurements of thermospheric winds between February 2018 and January 2019. Separate frequency analyses are done for each of the directions because they are binned independently, i.e. monthly averages were done for the wind in each direction before inputting them into the Lomb Scargle analysis. Peaks of the PSD are only counted if they surpass at least 90% significant level throughout the whole data set, signifying that they are most probably geophysical.

Figure 6.1 presents PSD for the north and south components of the meridional wind. Noticeable peaks are seen around the diurnal, semidiurnal, and terdiurnal tidal periods, which are summarised in Table 6.1. However the detected tidal components' periods may vary and their detection may also vary with months as well as wind direction. For example, for the diurnal tide the period vary between 23.0 and 25.7 hours, and although it is observed in all months it is more prominent in April–August and October–December, with PSD amplitude peaking in May. The period of the semidiurnal tide varies between 12.0 and 12.4 hours and it is also observed in all the months with maximum PSD amplitude in March–May, July, and September–October. It is the most dominant tidal component detected in meridional winds throughout all the months since it has the highest PSD amplitudes compared to the other tidal components. The terdiurnal tidal component with a period range of 8.0–8.6 hours is observed in almost all months but barely visually identifiable in June–August. Also, although it is more dominant in February–March, September–October and January, it has a

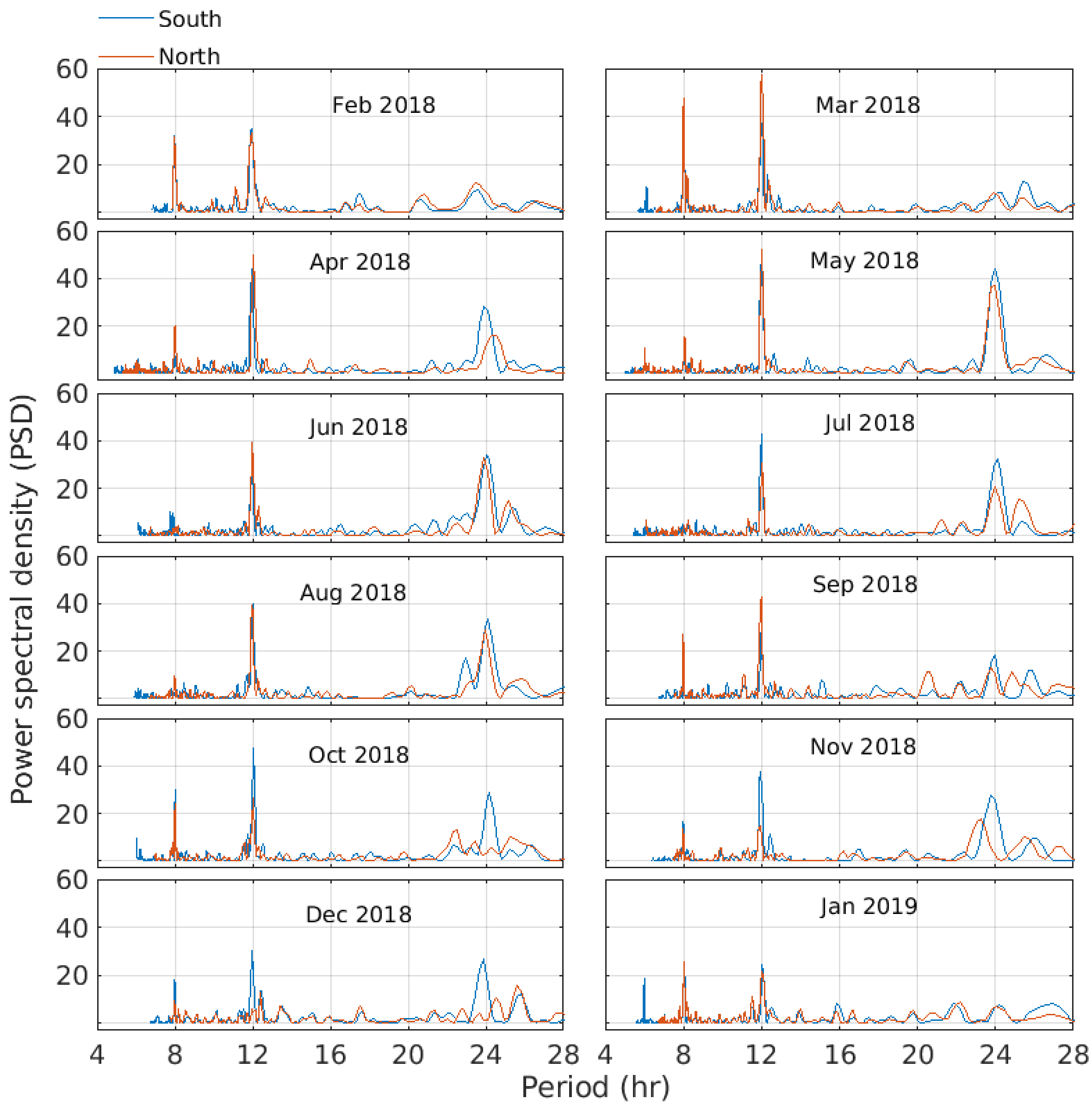

Figure 6.1: Lomb Scargle analysis of the south and north wind direction during the period of February 2018 to January 2019.

maximum PSD in March. Lastly, the signature of the 6 hour tide is clearly detectable in March, May, and January. It is also the least detected tidal component, in terms of PSD amplitude and time of year, i.e. it has the smallest amplitudes and is observed less often. In addition, these tidal components are sometimes detected more strongly in one meridional wind direction versus the other; for example, the diurnal tide has a higher PSD amplitudes in the meridional winds measured in the south compared to the north, most noticeably in April, May, and July–December. Likewise, the semidiurnal and terdiurnal tides are mostly stronger in the north meridional wind compared to the south, except in October–November.

Table 6.1: summary of the peak periods and their respective PSD values for the north and south directions of meridional neutral wind.

Tidal components	24hrs		12 hrs		8 hrs		6hrs	
Months	north	south	north	south	north	south	north	south
Februay	23.7	23.6	12.0	12.0	8.0	8.0	-	-
March	23.9	25.7	12.1	12.0	8.0	8.0	-	6.0
April	24.3	24.0	12.0	12.0	8.0	8.0	6.0	6.0
May	24.0	24.0	12.1	12.0	8.0	8.0	6.0	6.0
June	24.0	24.0	12.1	12.0	-	8.0	-	-
July	24.0	24.0	12.1	12.0	8.0	8.6	6.0	6.2
August	23.8	24.1	12.0	12.0	8.0	8.4	-	6.1
September	23.8	23.9	12.4	12.0	8.0	8.0	-	-
October	23.4	24.2	12.1	12.1	8.0	8.0	-	6.0
November	23.3	23.8	12.0	12.0	8.0	8.0	-	-
December	25.6	24.0	12.4	12.0	8.0	8.0	-	-
January	24.0	24.2	12.0	12.1	8.0	8.0	-	6.0

Similarly, for the PSD of the zonal wind presented in Figure 6.2, noticeable peaks are seen around the diurnal, semidiurnal, and terdiurnal tidal periods with their periods summarised in Table 6.2. However the detected components' periods and amplitudes vary monthly as well as wind direction. For example, for the diurnal tide the period vary between 23.3 and 24.2 hours, and although it is observed in all months, the PSD amplitude peaks in December–January. The period of the semidiurnal tide varies between 12.0 and 12.4 hours and it is also observed in all the months but with PSD amplitude peaking in April, October, and December–January. The tidal terdiurnal component with a period range of 8.0–8.4 hours was observed in the months but was more dominant in March, and August–December. Lastly, the $\sim$6 hour tide was detected in some months, for example, March, April, May, and July although the amplitudes of the PSD are lower compared to other tidal components, and was not detected in all the months. Furthermore, the diurnal tide has higher PSD amplitudes in the zonal wind measured in the east, most noticeably in MarchMay and September–January, compared to the west. Generally, there exist variations in the peak period and PSD values across the year in both wind directions. The peak of the power spectral of the 12 hour tidal component is generally stronger than the 24, 8, and 6 hour components. This result indicates that the 12 hour tides dominate the dynamic structure of the lower thermosphere. In addi-

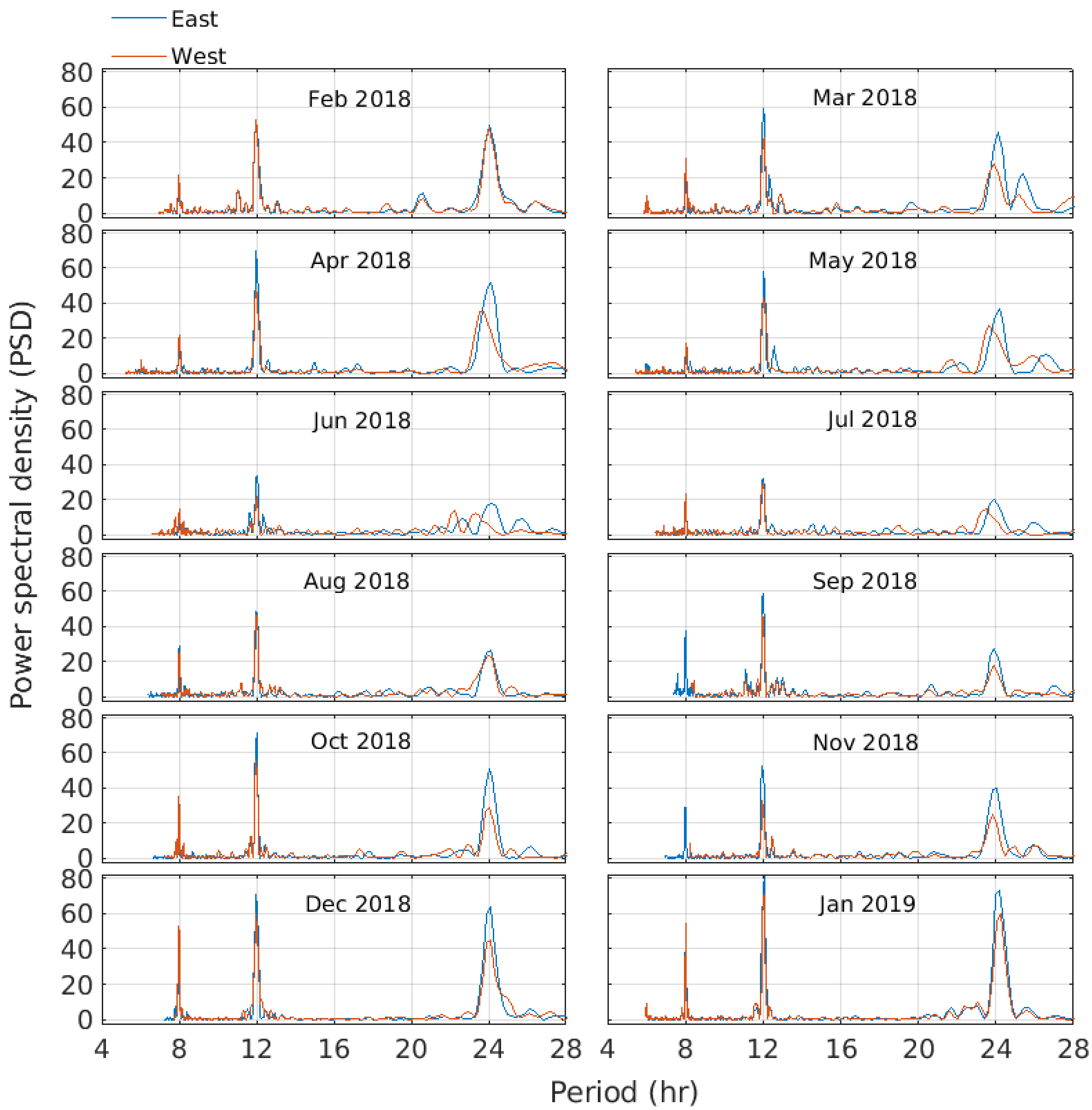

Figure 6.2: Lomb Scargle analysis of the west and east wind direction during the period of February 2018 to January 2019.

tion, although some periods of the tidal components detected in both meridional and zonal winds from the FPI measured wind over this region matched those of solar tides and some lunar tides, it is difficult to distinguish and be certain of their origin due to the ambiguity of the data.

Table 6.2: Summary of the peak periods and their respective PSD values for the west and east direction of zonal neutral wind

Tidal components	24hrs		12 hrs		8 hrs		6hrs	
Months	west	east	west	east	west	east	west	east
February	24.1	24.0	12.0	12.0	8.0	8.0	-	-
March	24.0	24.2	12.1	12.0	8.0	8.0	6.0	-
April	24.1	23.5	12.0	12.0	8.0	8.0	6.0	
May	23.6	24.2	12.0	12.0	8.0	8.0	-	6.0
June	24.0	23.3	12.0	12.0	8.0	8.0	-	-
July	23.5	24.1	12.0	12.0	8.0	8.0	6.9	-
August	24.1	24.2	12.0	12.0	8.0	8.0	-	-
September	24.0	23.9	12.4	12.4	8.4	8.0	-	-
October	24.1	24.2	12.0	12.0	8.0	8.0	-	-
November	24.0	23.8	12.0	12.0	8.1	8.0	-	-
December	24.1	24.1	12.0	12.0	8.0	8.0	-	-
January	24.2	24.2	12.1	12.0	8.0	8.0	-	-

6.2 Discussion

The thermospheric wind from the FPI measurements located in Sutherland, South Africa, from February 2018–January 2019 has been used to analyze different monthly tidal components, dominant monthly tidal components, and their variability for the first time over this region. Quasi-periodic oscillations with periods similar to those of tidal harmonics were detected regularly from both meridional and zonal thermospheric winds. However, the detected periods of the tidal components varied in some months and Fisher *et al.* (1999) suggested that this apparent fluctuation may be due to unresolved combinations of tidal frequencies and planetary waves or due to undersampling and aliasing of the geophysical winds. Generally, the results presented here agree with previous studies that have been reported in different locations using various instruments (e.g. Vasseur, 1969; Deng *et al.*, 1997; Zhou *et al.*, 1997; Fisher *et al.*, 1999; Fisher *et al.*, 2002).

Most of the extracted periods of the tidal components, shown in Tables 6.1–6.2, are closer to the periods expected of solar tides than lunar tides, which may suggest that solar tides were more dominant than lunar tides. This observations may be supported by literature where it has been reported that the dominant dynamic feature of the upper mesosphere and the lower thermosphere is the solar thermal tide (Teitelbaum *et al.*, 1989; Fuller-Rowell, 1995).

The strongest forcing of migrating tides is due to solar radiation absorption by tropospheric water vapour and stratospheric ozone (Lindzen, 1967; Teitelbaum *et al.*, 1989).

The diurnal tide was observed in both meridional and zonal winds as shown in Figures 6.1 and 6.2. This result agrees with previous theoretical work and studies done at other latitudes using similar ground based instruments. For example, theoretical work by Buonsanto (1999) showed that the diurnal tide is largely due to in situ excitation. Also Drob (1996) used redline (630.0nm) airglow emission measurements by an FPI to investigate the existence of tidal components and found a large diurnal oscillation. The diurnal tide reported here most probably represents the response of the atmosphere to the largest component of solar heating. Past observations have shown that the diurnal tide is dominated at low latitudes by the migrating diurnal tide, which itself is dominated by the upward propagating diurnal Hough mode, while evanescent modes dominate the diurnal tidal response at mid to high latitudes (Hays *et al.*, 1994; Burrage *et al.*, 1995; Wu *et al.*, 2006; Wu *et al.*, 2008). The diurnal tide has a strong amplitude and is frequently observed across the months, consistent with reports from various instruments (e.g.Forbes *et al.*, 1995). The results presented here showed that the signature of the diurnal tide in the meridional (zonal) wind was stronger in winter (summer) and weaker in summer (winter). This analysis is consistent with previous studies in terms of the presence of a diurnal tidal component in different seasons and seasonal variations, for example, Gong *et al.* (2021) shows strong diurnal tide during summer and winter at ∼250 km compared to the other seasons.

The semidiurnal tide is the most dominant tidal component in both meridional and zonal winds, as shown in Figures 6.1 and 6.2, consistent with previous studies that have used similar FPI instruments and with studies from other latitudes (e.g. Myrabø, 1984; Walterscheid *et al.*, 1986; Sivjee *et al.*, 1994; Forbes *et al.*, 1995; Walterscheid & Sivjee, 1996; Oznovich *et al.*, 1997; Fisher *et al.*, 1999; Fisher *et al.*, 2002; Schunk & Nagy, 2009). The semidiurnal tide was dominant in almost all the months and seasons, i.e. higher PSD amplitudes in most months of all seasons except summer (winter) in the meridional (zonal) wind. This result is consistent with the report by Harper (1981) using the Arecibo ISR measurements, and concluded that semidiurnal tide dominates the wind field above 110 km. The non-season trend in the semidiurnal tide in both meridional and zonal winds presented here is inconsistent with previous studies. For example, Goncharenko & Salah (1998) reported a strong semidiurnal signature during equinox and summer when using measurements taken below 130 km. On the other hand, Gong *et al.* (2021) showed that the semidiurnal signature is stronger in autumn compared to other season above 250 km. These variations in PSD peak may be attributed to changes in the wind pattern in the middle atmosphere altering the vertical propagation conditions of the tide (Fuller-Rowell *et al.*, 2010; Jin *et al.*, 2012; Fuller-Rowell *et al.*, 2016).

For example, the summer peak of the semidiurnal tide of the zonal wind could be due to zonal-mean circulation of the thermosphere driven by differential solar heating, which is from summer to winter with upwelling in the summer hemisphere and downwelling in the winter hemisphere (Forbes, 2007). The weak summer semidiurnal tide amplitudes could be due to ion drag in momentum coupling between the diurnal component of neutral winds and the diurnal variations of ion densities and drifts which occur in summer (Amayenc, 1974; Mayr *et al.*, 1979; Forbes, 1982).

In this result, the amplitude of the terdiurnal tidal component is generally smaller than the diurnal or semidiurnal tide, consistent with studies by Zhao *et al.* (2005) and Gong & Zhou (2011). A terdiurnal tide was observed in both meridional and zonal winds across all months analysed. The semidiurnal tide may be generated from coupling between the diurnal and semidiurnal variations in winds, while ion drag excite the terdiurnal tide and higher-order modes (e.g., Mayr *et al.*, 1979; Forbes, 1982; Thayaparan, 1997). In addition, Teitelbaum *et al.* (1989) theoretically showed that a significant terdiurnal oscillation can be generated by the superposition of a solar-driven 8 hours tide and a non-linear interaction between the diurnal and semidiurnal tides. The terdiurnal tides exhibit a seasonal variation. This tidal component is stronger in winter for the meridional wind compared to other seasons, this result agrees with typical midlatitude trends reported by other studies (e.g. Manson & Meek, 1986; Manson *et al.*, 1989; Thayaparan, 1997). Generally, the 6-hour tidal component has a small amplitude compared to the 24, 12, and 8 tidal components, and it is occasionally observed. This is consistent with previous studies (e.g. She *et al.*, 2002 ; Jacobi *et al.*, 2017; Gong *et al.*, 2018). The 6-hour tide is mostly detected during winter. This result agrees with previous reports (e.g. Liu *et al.*, 2015; Xu *et al.*, 2012; Xu *et al.*, 2014).

6.3 Summary

This chapter briefly described the spectral analysis-Lomb Scargle analysis. Different tidal harmonics (24, 12, 8, and 6 hours) were extracted from the neutral winds from the FPI located in Sutherland, South Africa. Generally, the semidiurnal tidal component was the most dominant component across the months. The diurnal and terdiurnal tides exhibit a seasonal variation. For example diurnal tide in the meridional (zonal) wind was stronger in winter (summer) and weaker in summer (winter) and the terdiurnal tide component is stronger in winter for the meridional wind compared to other seasons. There is no detected seasonal variation in the semidiurnal tide in both meridional and zonal winds.

Chapter 7

Conclusions and Future work

Thermospheric neutral winds greatly influence the dynamics in the upper atmosphere as they play a crucial role in the dynamics of the ionospheric F region as well as in the generation of electric fields and currents, instabilities, and Joule heating (Rees, 1995; Heelis, 2004). Despite their huge signicant contribution to ionospheric dynamics, they are generally insufficiently sampled, especially in the southern midlatitude region in Africa due to lack of observations. Therefore, in an effort to bridge this gap, this project focused on studying the dynamics of the nighttime thermospheric winds over Sutherland, South Africa, using the observations from a ground-based FPI. The contribution of atmospheric tides to the neutral wind dynamics over this location was also investigated. In addition, in an attempt to extend neutral wind measurements from a single location (Sutherland) to a large area, ionospheric measurements from four ionosondes belonging to the South African ionosonde network were used to derive meridional wind.

7.1 Summary and conclusion

In this work, a brief introduction to and description of the upper atmosphere, thermospheric neutral winds and tides, as well as a mathematical derivation of atmospheric tides were presented. A chapter was dedicated to discussing detailed processes of FPI of observations, ionosondes, and ionosondes derived meridional as well as, data analysis. In general terms, this study was done in three distinct phases, as summarised below.

In the first phase, the first results of the climatology of thermospheric neutral winds were presented using the fairly recently installed FPI located in Sutherland, South Africa (32.2°S, 20.48°E; geomagnetic latitude: 40.7°S), during a geomagnetically quiet period of February 2018–January 2019. The annual behaviour showed meridional wind that is more equatorward during summer, with the poleward wind seen mostly in the early evening during local winter. In addition to the annual variation, the meridional wind exhibited semiannual and quasi-terannual variations where the wind velocities peak around the summer and winter solstices (i.e. January and June) as well as around the spring equinox (i.e. September), with the highest peak seen in summer. The zonal wind exhibited an annual variation, where it was more eastward during winter than summer, and higher in the winter months compared to other seasons. Furthermore, the monthly averages of nighttime thermospheric winds from the HWM14 were validated with the FPI measured data and the model was found to have better agreement with the measurements for the meridional winds compared to the zonal winds. In addition, the HWM14 zonal wind consistently peaked several hours ($\sim$3 h) prior to the measured wind. The cause of this temporal difference was investigated and determined to be the result of a difference in phase shift of the terdiurnal tide. This was achieved by decomposing the HWM14 modeled winds into different tidal components and adjusting the properties of the terdiurnal tide alone, which resulted into an improved agreement between measured and modeled zonal winds.

The second phase focused on deriving meridional wind from ionosonde measurements, since ionosondes are more prolific with wider temporal and spatial coverage than FPIs. In addition, many techniques have been developed to calculate meridional wind from ionospheric F2 peak height (hmF2) measurements (Miller *et al.*, 1986; Buonsanto *et al.*, 1989; Buonsanto *et al.*, 1997; Dyson *et al.*, 1997; Fagundes *et al.*, 2008; Muella *et al.*, 2008; Dandenault, 2018). This study used hmF2 measurements from 4 ionosondes located in Grahamstown, Hermanus, Louisvale and Madimbo to derive the meridional wind based on the servo model, which was then validated using the Sutherland based FPI. The results were also compared to the widely used HWM14, and a model that was developed using historic ionosonde data, including data from our region of interest, called MENTAT in order to benchmark the performance of the servo model. Benchmarking servo model against other models was especially important since none of the ionosonde stations are co-located with the FPI. It was found that the station closest to the FPI, i.e. Hermanus, had better agreement with measurements. Results also showed that generally the servo and HWM14 models provided the best estimates of meridional wind 58% of the time.

Lastly, the final phase of the project focused on extraction and analysis of atmospheric tides from a year of quiet-time Sutherland FPI observations. In addition, variations of these tidal signatures in the FPI wind measurements were investigated by determining which tidal components dominate in each season. Noticeable peaks were mostly seen around the diurnal, semidiurnal, and terdiurnal tidal periods with their periods and PSD amplitudes across the months of observations. The results presented here showed that the semidiurnal tide was the most dominant tidal component throughout the period of this study. In terms of seasonal variations of the tidal signatures, the diurnal tide was stronger in winter (in meridional wind) and summer (in zonal wind). Similarly, the terdiurnal tide was stronger in summer (zonal wind) and winter (meridional wind), while the semidiurnal tide had no clear seasonal trend.

Lastly, the 6 hour tide was also detected in a few months and had the smallest amplitude.

7.2 Future work

This study presented the first tidal analysis from the FPI observations over Sutherland, South Africa, where different tidal components such as diurnal, semidiurnal, and terdiurnal were investigated. The scope of the study can be extended using FPI from other latitudes over the African region, such as Ethiopia, Morocco and Nigeria, so that it would be possible to investigate migrating and non-migrating tides, since migrating and non-migrating tides could not be calculated using data from a single instrument and because tidal influences on thermospheric measurements over this region has not been fully studied yet. Furthermore, although the diurnal and terdiurnal tides exhibited clear seasonal variations, their trends were sometimes different from those observed in other studies. Also, no seasonal trend was detected for the semidiurnal tide in both meridional and zonal winds. Further investigation of the seasonal variations of the tides using longer term dataset in this region is therefore encouraged.

In addition to neutral winds the FPI also measures neutral temperature, but this parameter was not studied in this project, and therefore a study to understand the variability of the temperature over this region would be valuable. One of the interesting features on the night-time thermospheric neutral temperature is the midnight temperature maximum (MTM). The MTM has mostly been studied in various regions such as North and South America, East Africa, Caribbean, and Indian (e.g. Fesen, 1996; Faivre *et al.*, 2006; Martinis *et al.*, 2006; Meriwether *et al.*, 2008; Akmaev *et al.*, 2009; Akmaev *et al.*, 2010; Oliver *et al.*, 2012; Ruan *et al.*, 2013; Hickey *et al.*, 2014), therefore an investigation of this feature using the South African FPI would provide further insight on it.

Due to the sparsity of ionosondes over the Africa continent, the servo model can be extended to the whole of the continent with the use of hmF2 from LEO satellites like COSMIC. Results from a comparison between HWM14 and FPI data showed better agreement between FPI measured winds and HWM14 modeled winds for the meridional component compared to the zonal component. HWM14 zonal wind consistently peaked several hours ($\sim$3 hour) prior to the measured wind due to a phase shift of the terdiurnal tide. Since there is some wind variation that is not currently captured by HWM14 over this region, to further improve on the model's predicton capability, data from the FPI in Sutherland should be used for future versions of the HWM.

References

Akmaev, R., Wu, F., Fuller-Rowell, T. & Wang, H. (2009). Midnight temperature maximum (MTM) in Whole Atmosphere Model (WAM) Simulations. *Geophysical Research Letters*, **36,** L0710836. doi: 10.1029/2009GL037759.

Akmaev, R., Wu, F., Fuller-Rowell, T., Wang, H. & Iredell, M. (2010). Midnight density and temperature maxima, and thermospheric dynamics in Whole Atmosphere Model Simulations. *Journal of Geophysical Research: Space Physics*, **115,**A08326. doi: 10.1029/2010JA015651.

Amabayo, E.B. (2011). *Multi-instrument observations of ionospheric irregularities over South Africa*. Ph.D. thesis, Rhodes University. http://hdl.handle.net/10962/d1005261.

Amayenc, P. (1974). Tidal oscillations of the meridional neutral wind at midlatitudes. *Radio Science*, **9**, 281–293. doi:10.1029/RS009i002p00281.

Amayenc, P. & Reddy, C. (1972). Height structure of tidal winds as inferred from incoherent scatter observations. *Planetary and Space Science*, **20**, 1269–1279. doi: 10.1029/97JA00440.

Appleton, E.V. & Barnett, M. (1925). On some direct evidence for downward atmospheric reflection of electric rays. *Proceedings of the Royal Society of London. Series A, Containing Papers of a Mathematical and Physical Character*, **109**, 621–641. doi:0.1098/rspa.1925.0149.

Babcock, H.D. (1923). A study of the green auroral line by the interference method. *The Astrophysical Journal*, **57**, 209–221. doi: 10.1086/142747.

Baker, D.N. & Lanzerotti, L.J. (2016). Resource letter SW1: Space weather. *American Journal of Physics*, **84**, 166–180. doi:10.1119/1.4938403.

Balan, N., Skoug, R., Tulasi Ram, S., Rajesh, P., Shiokawa, K., Otsuka, Y., Batista, I., Ebihara, Y. & Nakamura, T. (2014). CME front and severe space weather. *Journal of Geophysical Research: Space Physics*, **119**, 10041–10058. doi:10.1002/2014JA020151.

Bamgboye, D. & McClure, J. (1982). Seasonal variation in the occurrence time of the equatorial midnight temperature bulge. *Geophysical Research Letters*, **9**, 457–460, doi:10.1029/GL009i004p00457.

Banks, P. & Kockarts, G. (1973). Aeronomy, part A. Elsevier, ISBN: 9781483260068.

Banks, P.M. & Holzer, T.E. (1968). Charge exchange and ion diffusion for thermal nonequilibrium conditions. *Planetary and Space Science*, **16**, 1019–1022. doi: 10.1016/0032-0633(68)90018-4.

Basu, S., Buchau, J., Rich, F., Weber, E., Field, E., Heckscher, J., Kossey, P., Lewis, E., Dandekar, B., McNamara, L. *et al.* (1985). Ionospheric radio wave propagation. In Jursa, A.S. (Ed.), *Handbook of Geophysics and the Space Environment*. Air Force Geophysics Laboratory.

Baumjohann, W. & Treumann, R. (1997). *Advanced space plasma physics*. World Scientific, ISBN: 9781860940262.

Bens, A., Cogger, L. & Shepherd, G. (1965). Upper atmospheric temperatures from Doppler line widthsIII: Observation of the OI dayglow emission at 6300 Å. *Planetary and Space Science*, **13**, 551–563. doi:10.1016/0032-0633(65)90168-6.

Bibl, K. (1998). Evolution of the ionosonde. *Annals of Geophysics*, **41**, 41(5-6). doi:10.4401/ag-3810.

Bilitza, D. (1993). International reference ionosphere - past, present, and future: 1. Electron Density. *Advances in Space Research*, 13(3), 3-13. doi:10.1016/0273-1177(93)90240-C.

Bilitza, D., Altadill, D., Truhlik, V., Shubin, V., Galkin, I., Reinisch, B. & Huang, X. (2017). International reference ionosphere 2016: From ionospheric climate to real-time weather predictions. *Space Weather*, **15**, 418–429. doi:10.1002/2016SW001593.

Biondi, M.A. & Feibelman, W.A. (1968). Twilight and nightglow spectral line shapes of oxygen λ6300 and λ5577 radiation. *Planetary and Space Science*, **16**, 431–443. doi:10.1016/0032-0633(68)90158-X.

Breit, G. & Tuve, M.A. (1926). A test of the existence of the conducting layer. *Physical Review*, **28**, 431–443. doi: 10.1016/0032-0633(68)90158-X.

Brum, C.G.M., Tepley, C.A., Fentzke, J.T., Robles, E., Dos Santos, P.T. & Gonzalez, S.A. (2012). Long-term changes in the thermospheric neutral winds over Arecibo: Climatology based on over three decades of Fabry-Perot observations. *Journal of Geophysical Research: Space Physics*, 117, A00H14. doi:10.1103/PhysRev.28.554.

Buonsanto, M. (1990). Observed and calculated F2 peak heights and derived meridional winds at mid-latitudes over a full solar cycle. *Journal of Atmospheric and Terrestrial Physics*, **52**, 223–240. doi:10.5194/angeo-25-1337-2007.

Buonsanto, M., Salah, J., Miller, K., Oliver, W., Burnside, R. & Richards, P. (1989). Observations of neutral circulation at mid-latitudes during the equinox transition study. *Journal of Geophysical Research: Space Physics*, **94**, 16987–16997. doi:10.1029/JA094iA12p16987.

Buonsanto, M., Starks, M., Titheridge, J., Richards, P. & Miller, K. (1997). Comparison of techniques for derivation of neutral meridional winds from ionospheric data. *Journal of Geophysical Research: Space Physics*, **102**, 14477–14484. doi: 10.1029/97JA01149.

Buonsanto, M.J. (1999). Ionospheric stormsA review. *Space Science Reviews*, **88**, 563–601. doi.org/10.1023/A:1005107532631.

Burnside, R. & Tepley, C. (1990). Airglow intensities observed in the southern and northern hemispheres. *Planetary and space science*, **38**, 1161–1177. doi:10.1016/0032-0633(90)90024-K.

Burnside, R., Herrero, F., Meriwether Jr, J. & Walker, J. (1981). Optical observations of thermospheric dynamics at Arecibo. *Journal of Geophysical Research: Space Physics*, **86**, 5532–5540. doi:10.1029/JA086iA07p05532.

Burrage, M., Wu, D., Skinner, W., Ortland, D. & Hays, P. (1995). Latitude and seasonal dependence of the semidiurnal tide observed by the high-resolution doppler imager. *Journal of Geophysical Research: Atmospheres*, **100**, 11313–11321. doi:10.1029/95JD00696.

Chamberlain, J. (1961). Physics of the aurora and airglow. Academic Press. ISBN: 9781483222530.

Chapman, S. & Lindzen, R.S. (1970). Quantitative theory of atmospheric tides and thermal tides. In: *Atmospheric Tides*, Springer, Dordercht. Springer. doi:10.1007/978-94-010-3399-2_4.

Chen, F.F. *et al.* (1984). Introduction to plasma physics and controlled fusion. Vol. 1. *Springer* . ISBN: 978-3-319-22309-4.

Chu, K. (2019). Tidal analysis of modeled thermospheric winds to improve agreement with measurements over South Africa. MSc thesis*University of Illinois at Urbana-Champaign*. http://hdl.handle.net/2142/104808.

Cogger, L., Murphree, J., Tepley, C. & Meriwether Jr, J. (1985). Measurements of the E-region neutral wind field. *Planetary and Space Science*, **33**, 373–379. doi: 10.1016/0032-0633(85)90080-7.

Dalgarno, A. (1964). Ambipolar diffusion in the F-region. *Journal of Atmospheric and Terrestrial Physics*, **26**, 939-939. doi: 10.1016/0021-9169(64)90236-3.

Dandenault, P. (2018). Mentat: A new wind model for earth's thermosphere. *Journal of Geophysical Research: Space Physics*, **123**, 7124–7147. doi:10.1029/2018JA025551.

Dandenault, P.B. (2017). Characterization of Thermospheric Neutral Winds Using Empirical Modeling and Observational Validation. Ph.D. thesis. https://hdl.handle.net/1920/11261.

Dauni, P., Firdaus, M., Asfariani, R., Saputra, M., Hidayat, A. & Zulfikar, W. (2019). Implementation of Haversine formula for school location tracking. In *Journal of Physics: Conference Series*, **1402**, 077028 , doi: 10.1088/1742-6596/1402/7/07702.

Davies, K. (1990). Ionospheric radio. Peter Peregrinus. London. *NOAA Space Environment Center*, doi: 10.1049/PBEW031E.

Deng, W., Salah, J., Clark, R., Franke, S., Fritts, D., Hoffmann, P., Kuerschner, D., Manson, A., Meek, C., Murphy, D. *et al.* (1997). Coordinated global radar observations of tidal and planetary waves in the mesosphere and lower thermosphere during January 20–30, 1993. *Journal of Geophysical Research: Space Physics*, **102**, 7307–7318. doi: 10.1029/96JA01630.

Dickinson, R.E., Roble, R. & Ridley, E. (1971). Response of the neutral thermosphere at F-layer heights to interaction of a global wind with anomalies of ionization. *Journal of Atmospheric Sciences*, **28**, 1280–1293. doi:10.1175/1520-0469.

Dowdy, K.R. (1993). An improved neutral wind model with predictive capabilities. Defense Technical Information Center. dentifier:DTIC$_A DA$282283

Drob, D.P. (1996). Ground-based optical detection of atmospheric waves in the upper mesosphere and lower thermosphere. *University of Michigan*. ISBN 0591194945, 9780591194944.

Drob, D.P., Emmert, J.T., Meriwether, J.W., Makela, J.J., Doornbos, E., Conde, M., Hernandez, G., Noto, J., Zawdie, K.A., McDonald, S.E. *et al.* (2015). An update to the Horizontal Wind Model (HWM): The quiet time thermosphere. *Earth and Space Science*, **2**, 301–319. doi:10.1002/2014EA000089.

Dyson, P., Davies, T., Parkinson, M., Reeves, A., Richards, P. & Fairchild, C. (1997). Thermospheric neutral winds at southern mid-latitudes: A comparison of optical and ionosonde hmF2 methods. *Journal of Geophysical Research: Space Physics*, **102**, 27189–27196. doi:10.1029/97JA02138.

Emmert, J., Fejer, B.G., Shepherd, G. & Solheim, B. (2002). Altitude dependence of middle and low-latitude daytime thermospheric disturbance winds measured by WINDII. *Journal of Geophysical Research: Space Physics*, **107**, 1483. doi: 10.1029/2002JA009646.

Emmert, J., Faivre, M., Hernandez, G., Jarvis, M., Meriwether, J., Niciejewski, R., Sipler, D. & Tepley, C. (2006). Climatologies of nighttime upper thermospheric winds measured by ground-based Fabry-Perot interferometers during geomagnetically quiet conditions: 1. Local time, latitudinal, seasonal, and solar cycle dependence. *Journal of Geophysical Research: Space Physics*, **111**, A12303. doi:10.1029/2006JA011948.

England, S. (2012). A review of the effects of non-migrating atmospheric tides on the Earths low-latitude ionosphere. *Space Science Reviews*, **168**, 211–236. doi: 10.1007/s11214-011-9842-4.

Fagundes, P., Sahai, Y., Medeiros, R., Batista, I., Bittencourt, J. & Takahashi, H. (1997). Nighttime F2-layer peak height changes due to thermospheric winds. *Advances in Space Research*, **20**, 1141–1144. doi: 10.1029/97JA01387.

Fagundes, P., Muella, M., Bittencourt, J., Sahai, Y., Lima, W., Guarnieri, F., Becker-Guedes, F., Pillat, V., Ferreira, A. & Lima, N. (2008). Nighttime ionosphere–thermosphere coupling observed during an intense geomagnetic storm. *Advances in Space Research*, **41**, 539–547. doi: 10.1016/j.asr.2007.11.005.

Faivre, M., Meriwether, J., Fesen, C. & Biondi, M. (2006). Climatology of the midnight temperature maximum phenomenon at Arequipa, Peru. *Journal of Geophysical Research: Space Physics*, **111**, A06302. doi: 10.1029/2005JA011321.

Fejer, B.G., Emmert, J. & Sipler, D. (2002). Climatology and storm time dependence of nighttime thermospheric neutral winds over Millstone Hill. *Journal of Geophysical Research: Space Physics*, **107**, 1052 . doi: 10.1029/2001JA000300.

Fesen, C. (1996). Simulations of the low-latitude midnight temperature maximum. *Journal of Geophysical Research: Space Physics*, **101**, 26863–26874. doi:10.1029/96JA01823.

Fisher, D. (2013). Three-dimensional wind measurements and modeling using a bi-static Fabry-Perot interferometer system in Brazil. MSc. thesis, University of *Illinois at Urbana-Champaign*, http://hdl.handle.net/20.500.12816/4458.

Fisher, D.J. (2017). Observations of the thermosphere using measurements from long-term Fabry-Perot interferometers. Ph.D. thesis, *University of Illinois at Urbana-Champaign*. http://hdl.handle.net/2142/98114

Fisher, D.J., Makela, J.J., Meriwether, J.W., Buriti, R.A., Benkhaldoun, Z., Kaab, M. & Lagheryeb, A. (2015). Climatologies of nighttime thermospheric winds and temperatures from Fabry-Perot interferometer measurements: From solar minimum to solar maximum. *Journal of Geophysical Research: Space Physics*, **120**, 6679–6693. doi: 10.1002/2015JA021170.

Fisher, G.M., Killeen, T.L., Wu, Q., Hays, P.B. & Reeves, J. (1999). Tidal variability of the geomagnetic polar cap mesopause above Resolute Bay. *Geophysical Research Letters*, **26**, 573–576. doi: 10.1029/1999GL900046.

Fisher, G.M., Niciejewski, R.J., Killeen, T.L., Gault, W.A., Shepherd, G.G., Brown, S. & Wu, Q. (2002). Twelve-hour tides in the winter northern polar mesosphere and lower thermosphere. *Journal of Geophysical Research: Space Physics*, **107**,1211. doi: 10.1029/2001JA000294.

Forbes, J., Russell, J., Miyahara, S., Zhang, X., Palo, S., Mlynczak, M., Mertens, C. & Hagan, M. (2006). Troposphere-thermosphere tidal coupling as measured by the SABER instrument on TIMED during July–September 2002. *Journal of Geophysical Research: Space Physics*, **111**, A10S06. doi:10.1029/2005JA011492.

Forbes, J.M. (1982). Atmospheric tides: 1. Model description and results for the solar diurnal component. *Journal of Geophysical Research: Space Physics*, **87**, 5222–5240. doi.org/10.1029/JA087iA07p05222

Forbes, J.M. (2007). Dynamics of the thermosphere. *Journal of the Meteorological Society of Japan. Ser. II*, **85**, 193–213. doi:10.2151/jmsj.85B.193.

Forbes, J.M., Bruinsma, S.L., Miyoshi, Y. & Fujiwara, H. (2008). A solar terminator wave in thermosphere neutral densities measured by the CHAMP satellite. *Geophysical Research Letters*, **35**, 14. L14802, doi:10.1029/2008GL034075.

Forbes, J.M. *et al.* (1995).Tidal and planetary waves. In: Upper mesosphere and lower thermosphere: A review of experiment and theory, Vol 87, (pp. 67–87), *American Geophysical Union* , doi: 10.1029/GM087p0067.

Fraser-Smith, A.C. (1972). Spectrum of the geomagnetic activity index Ap. *Journal of Geophysical Research*, **77**, 4209–4220. doi:10.1029/JA077i022p04209.

Fuller-Rowell, T. (1995). The dynamics of the lower thermosphere. In: The Upper Mesosphere and Lower Thermosphere: A Review of Experiment and Theory, 87, (pp 23–36). doi:10.1186/s40645-015-0035-8.

Fuller-Rowell, T., Wu, F., Akmaev, R., Fang, T.W. & Araujo-Pradere, E. (2010). A whole atmosphere model simulation of the impact of a sudden stratospheric warming on thermosphere dynamics and electrodynamics. *Journal of Geophysical Research: Space Physics*, **115**. doi: 10.1029/2010JA015524

Fuller-Rowell, T.J., Fang, T., Wang, H., Matthias, V., Hoffmann, P., Hocke, K. & Studer, S. (2016). Impact of migrating tides on electrodynamics during the January 2009 sudden stratospheric warming. In: Ionospheric Space Weather: Longitude and Hemispheric Dependences and Lower Atmosphere Forcing, (pp. 165–174). doi:10.1002/9781118929216.ch14.

Goncharenko, L. & Salah, J. (1998). Climatology and variability of the semidiurnal tide in the lower thermosphere over Millstone Hill. *Journal of Geophysical Research: Space Physics*, **103**, 20715–20726. doi:10.1029/98JA01435.

Gong, Y. & Zhou, Q. (2011). Incoherent scatter radar study of the terdiurnal tide in the E-and F-region heights at Arecibo. *Geophysical Research Letters*, **38**, L15101. doi: 10.1029/2011GL048318.

Gong, Y., Ma, Z., Lv, X., Zhang, S., Zhou, Q., Aponte, N. & Sulzer, M. (2018). A study on the quarterdiurnal tide in the thermosphere at Arecibo during the February 2016 sudden stratospheric warming event. *Geophysical Research Letters*, **45**, 13142–13149. doi:10.1029/2018GL080422.

Gong, Y., Lv, X., Zhang, S., Zhou, Q. & Ma, Z. (2021). Climatology and seasonal variation of the thermospheric tides and their response to solar activities over Arecibo. *Journal of Atmospheric and Solar-Terrestrial Physics*, **215**, 105592. doi:10.1016/j.jastp.2021.105592.

Grawe, M.A., Chu, K.T. & Makela, J.J. (2019). Measurement of atmospheric neutral wind and temperature from Fabry–Perot interferometer data using piloted deconvolution. *Applied optics*, **58**, 3685–3695. doi:10.1364/AO.58.003685.

Groves, G. (1981). Notes on obtaining the eigenvalues of Laplace's tidal equation. *Planetary and Space Science*, **29**, 1339–1344. doi: 10.1016/0032-0633(81)90100-8.

Guo, H., Chen, S., Bao, A., Hu, J., Yang, B. & Stepanian, P.M. (2016). Comprehensive evaluation of high-resolution satellite-based precipitation products over China. *Atmosphere*, **7**, 1–6. doi: 10.3390/atmos7010006.

Gurubaran, S. (1993). Investigations of low latitude thermosphere-ionosphere system. *Ph.D. thesis*. Department of Physics, Gujarat University. http://hdl.handle.net/10603/46555.

Hanson, W. & Moffett, R. (1966). lonization transport effects in the equatorial F region. *Journal of Geophysical Research*, **71**, 5559–5572. doi:10.1029/JZ071i023p05559.

Harding, B.J. (2017). Midlatitude thermospheric wind and temperature: networked Fabry-Perot interferometer observations and radiative transfer modeling. Ph.D. thesis, University of Illinois at Urbana-Champaign. http://hdl.handle.net/2142/97286.

Harding, B.J., Gehrels, T.W. & Makela, J.J. (2014). Nonlinear regression method for estimating neutral wind and temperature from Fabry–Perot interferometer data. *Applied Optics*, **53**, 666–673. doi:10.1364/AO.53.000666.

Harding, B.J., Ridley, A.J. & Makela, J.J. (2019). Thermospheric weather as observed by ground-based FPIs and modeled by GITM. *Journal of Geophysical Research: Space Physics*, **124**, 1307–1316. doi:10.1029/2018JA026032.

Hargreaves, J.K. (1992). *The solar-terrestrial environment: an introduction to geospace-the science of the terrestrial upper atmosphere, ionosphere, and magnetosphere*. Cambridge University Press. doi:10.1017/CBO9780511628924.

Harper, R. (1981). Some results on mean tidal structure and day-to-day variability over Arecibo. *Journal of Atmospheric and Terrestrial Physics*, **43**, 255–262. doi: 10.1016/0021-9169(81)90047-7.

Haurwitz, B. (1964). Atmospheric tides. *Science*, **144**, 1415–1422. doi: 10.1126/science.144.3625.1415.

Häusler, K., Lühr, H., Rentz, S. & Köhler, W. (2007). A statistical analysis of longitudinal dependences of upper thermospheric zonal winds at dip equator latitudes derived from CHAMP. *Journal of Atmospheric and Solar-Terrestrial Physics*, **69**, 1419–1430. doi:10.1016/j.jastp.2007.04.004.

Hays, P., Rusch, D., Roble, R. & Walker, J. (1978). The OI (6300 Å) airglow. *Reviews of Geophysics*, **16**, 225–232. doi:10.1029/RG016i002p00225.

Hays, P.B., Wu, D. & HRDI Science Team, T. (1994). Observations of the diurnal tide from space. *Journal of Atmospheric Sciences*, **51**, 3077–3093. doi:10.1175/1520-0469(1994).

Hedin, A., Fleming, E., Manson, A., Schmidlin, F., Avery, S., Clark, R., Franks, S., Fraser, G., Tsuda, T., Vial, F. *et al.* (1996). Empirical wind model for the upper, middle and lower atmosphere, *Journal of Atmospheric and Terrestrial Physics*, 58 (13), 1421-1447. doi:10.1016/0021-9169(95)00122-0.

Hedin, A.E., Spencer, N. & Killeen, T. (1988). Empirical global model of upper thermosphere winds based on Atmosphere and Dynamics Explorer satellite data. *Journal of Geophysical Research: Space Physics*, **93**, 9959–9978. doi:10.1029/JA093iA09p09959.

Hedin, A.E., Biondi, M., Burnside, R., Hernandez, G., Johnson, R., Killeen, T., Mazaudier, C., Meriwether, J., Salah, J., Sica, R. *et al.* (1991). Revised global model of thermosphere winds using satellite and ground-based observations. *Journal of Geophysical Research: Space Physics*, **96**, 7657–7688. doi: 10.1029/91JA00251.

Heelis, R. (2004). Electrodynamics in the low and middle latitude ionosphere: A tutorial. *Journal of Atmospheric and Solar-Terrestrial Physics*, **66**, 825–838. doi:10.1016/j.jastp.2004.01.034.

Hernandez, G. (1982). Vertical motions of the neutral thermosphere at midlatitude. *Geophysical Research Letters*, **9**, 555–557. doi: 10.1029/GL009i005p00555.

Hernandez, G. & Roble, R. (1976). Direct measurements of nighttime thermospheric winds and temperatures, 2. Geomagnetic storms. *Journal of Geophysical Research*, **81**, 5173–5181. doi:10.1029/JA081i028p05173.

Hernandez, G. & Roble, R. (1979). Thermospheric dynamics investigations with very high resolution spectrometers. *Applied Optics*, **18**, 3376–3385. doi:10.1364/AO.18.003376.

Hernandez, G., Fraser, G. & Smith, R. (1993). Mesospheric 12-hour oscillation near South Pole, Antarctica. *Geophysical Research Letters*, **20**, 1787–1790. doi:10.1029/93GL01983.

Herzberg, G. & Spinks, J.W.T. (1944). *Atomic spectra and atomic structure*. Dover Publications. ISBN:0486601153.

Hickey, D.A., Martinis, C.R., Erickson, P.J., Goncharenko, L.P., Meriwether, J.W., Mesquita, R., Oliver, W.L. & Wright, A. (2014). New radar observations of temporal and spatial dynamics of the midnight temperature maximum at low latitude and midlatitude. *Journal of Geophysical Research: Space Physics*, **119**, 10–499. doi: 10.1002/2014JA020719.

Hickey, M.P., Schubert, G. & Walterscheid, R. (2009). Propagation of tsunami-driven gravity waves into the thermosphere and ionosphere. *Journal of Geophysical Research: Space Physics*, **114** A08304. doi.org/10.1029/2009JA014105.

Holton, J.R. (1975). The development of dynamical models. In Holton, J.R. (Ed.), *The Dynamic Meteorology of the Stratosphere and Mesosphere*, (pp. 27-80). Springer. ISBN: 97830306672980.

Horne, J.H. & Baliunas, S.L. (1986). A prescription for period analysis of unevenly sampled time series. *The Astrophysical Journal*, **302**, 757–763. doi: 10.1086/164037.

Hough, S. (1897). On the application of harmonic analysis to the dynamical theory of the tides. part II. On the general integration of Laplace's dynamical equations. *Proceedings of the Royal Society of London Series I*, **62**, 209–210. doi.org/10.1098/rsta.1898.0005.

Hough, S.S. (1898). V. On the application of harmonic analysis to the dynamical theory of the tides.part II. On the general integration of laplaces dynamical equations. *Philosophical Transactions of the Royal Society of London. Series A, Containing Papers of a Mathematical or Physical Character*, 139–185. d: 10.1098/rsta.1898.0005.

Hunsucker, R.D. & Hargreaves, J.K. (2007). *The high-latitude ionosphere and its effects on radio propagation*. Cambridge University Press. doi:10.1017/CBO9780511535758.

Jacobi, C., Krug, A. & Merzlyakov, E. (2017). Radar observations of the quarterdiurnal tide at midlatitudes: Seasonal and long-term variations. *Journal of Atmospheric and Solar-Terrestrial Physics*, **163**, 70–77. doi:10.1016/j.jastp.2017.05.014.

Jiang, G., Xu, J., Wang, W., Yuan, W., Zhang, S., Yu, T., Zhang, X., Huang, C., Kerr, R.B., Noto, J. *et al.* (2018). A comparison of quiet time thermospheric winds between FPI observations and model calculations. *Journal of Geophysical Research: Space Physics*, **123**, 7789–7805. doi:10.1029/2018JA025424.

Jin, H., Miyoshi, Y., Pancheva, D., Mukhtarov, P., Fujiwara, H. & Shinagawa, H. (2012). Response of migrating tides to the stratospheric sudden warming in 2009 and their effects on the ionosphere studied by a whole atmosphere-ionosphere model GAIA with COSMIC and TIMED/SABER observations. *Journal of Geophysical Research: Space Physics*, **117**. doi:10.1029/2012JA017650.

Kaab, M., Benkhaldoun, Z., Fisher, D.J., Harding, B., Bounhir, A., Makela, J.J., Laghriyeb, A., Malki, K., Daassou, A. & Lazrek, M. (2017). Climatology of thermospheric neutral winds over Oukaïmeden observatory in Morocco. *Ann. Geophys*, **35**, 161–170. doi:10.5194/angeo-35-161-2017, 2017.

Kelley, M. & Ulwick, J. (1988). Large-and small-scale organization of electrons in the high-latitude mesosphere: Implications of the state data. *Journal of Geophysical Research: Atmospheres*, **93**, 7001–7008. doi:10.1029/JD093iD06p07001.

Kelley, M.C. (2009). *The Earth's ionosphere: plasma physics and electrodynamics*. Academic Press. ISBN: 9780080916576.

Killeen, T., Roble, R.G. & Spencer, N.W. (1987). A computer model of global thermospheric winds and temperatures. *Advances in Space Research*, **7**, 207–215. doi:10.1016/0273-1177(87)90094-9.

Kudeki, E., Akgiray, A., Milla, M., Chau, J.L. & Hysell, D.L. (2007). Equatorial spread-F initiation: Post-sunset vortex, thermospheric winds, gravity waves. *Journal of Atmospheric and Solar-Terrestrial Physics*, **69**, 2416–2427. doi:10.1016/j.jastp.2007.04.012.

Laplace, P.S. (1799). *Traité de mécanique céleste*. De l'Imprimerie de Crapelet.

Lindzen, R.S. (1967). Thermally driven diurnal tide in the atmosphere. *Quarterly Journal of the Royal Meteorological Society*, **93**, 18–42. doi:10.1002/qj.49709339503.

Lindzen, R.S. & Chapman, S. (1969). Atmospheric tides. *Space Science Reviews*, **10**, 3–188. doi:10.1007/BF00171584.

Link, R. & Cogger, L. (1988). A reexamination of the OI 6300-Å nightglow. *Journal of Geophysical Research: Space Physics*, **93**, 9883–9892. doi:10.1029/JA093iA09p09883.

Liu, H.L., McInerney, J., Santos, S., Lauritzen, P., Taylor, M. & Pedatella, N. (2014). Gravity waves simulated by high-resolution whole atmosphere community climate model. *Geophysical Research Letters*, **41**, 9106–9112. doi:10.1002/2014GL062468.

Liu, L., Luan, X., Wan, W., Ning, B. & Lei, J. (2003). A new approach to the derivation of dynamic information from ionosonde measurements. *Annales Geophysicae*, **21**, 2185-2191. doi:10.5194/angeo-21-2185-2003.

Liu, L., Wan, W., Zhang, M.L., Ning, B., Zhang, S.R. & Holt, J. (2007). Variations of topside ionospheric scale heights over Millstone Hill during the 30-day incoherent scatter radar experiment. *Annales Geophysicae*, **25**, 2019-2027. doi:10.5194/angeo-25-2019-2007.

Liu, M., Xu, J., Yue, J. & Jiang, G. (2015). Global structure and seasonal variations of the migrating 6-h tide observed by SABER/TIMED. *Science China Earth Sciences*, **58**, 1216–1227. doi: 10.1007/s11430-014-5046-6.

Lomb, N.R. (1976). Least-squares frequency analysis of unequally spaced data. *Astrophysics andSpace Science*, **39**, 447–462. doi:10.1007/BF00648343.

Luan, X. & Solomon, S.C. (2008). Meridional winds derived from COSMIC radio occultation measurements. *Journal of Geophysical Research: Space Physics*, **113**, A08302. doi: 10.1029/2008ja013089.

Macmillan, S. & Finlay, C. (2011). The International Geomagnetic Reference Field. In Mandea, M. and Korte, M. (Eds.), *Geomagnetic observations and models*, 183, 265-276. Springer. ISBN : 978-90-481-9857-3.

Makela, J.J., Meriwether, J.W., Ridley, A.J., Ciocca, M. & Castellez, M.W. (2012). Large-scale measurements of thermospheric dynamics with a multisite Fabry-Perot interferometer network: Overview of plans and results from midlatitude measurements. *International Journal of Geophysics*, **2012**,140 .doi:10.1155/2012/872140.

Makela, J.J., Fisher, D.J., Meriwether, J.W., Buriti, R.A. & Medeiros, A.F. (2013). Near-continual ground-based nighttime observations of thermospheric neutral winds and temperatures over equatorial Brazil from 2009 to 2012. *Journal of Atmospheric and Solar-Terrestrial Physics*, **103**, 94–102. doi: 10.1016/j.jastp.2012.11.019.

Mandea, M. & Macmillan, S. (2000). International geomagnetic reference fieldthe eighth generation. *Earth, planets and space*, **52**, 1119–1124. doi: 10.1016/j.jastp.2012.11.019.

Manson, A. & Meek, C. (1986). Dynamics of the middle atmosphere at Saskatoon (52^0 N, 107^0 W): A spectral study during 1981, 1982. *Journal of Atmospheric and Terrestrial physics*, **35**, 445–449, doi:10.1016/0032-0633(87)90101-2.

Manson, A., Meek, C., Teitelbaum, H., Vial, F., Schminder, R., Kürschner, D., Smith, M.J., Fraser, G. & Clark, R. (1989). Climatologies of semi-diurnal and diurnal tides in the middle atmosphere (70–110 km) at middle latitudes (40–55°). *Journal of Atmospheric and Terrestrial Physics*, **51**, 579–593. doi10.1016/0021-9169(89)90056-1.

Marquis de Laplace, P.S. (1825). *Traité de mécanique céleste*, vol. 5. Crapelet.

Martinis, C., Baumgardner, J., Smith, S., Colerico, M. & Mendillo, M. (2006). Imaging Science at El Leoncito, Argentina, 24, 13751385. doi: 10.5194/angeo-24-1375-2006.

Martyn, D. (1956). Processes controlling ionization distribution in the F2 region of the ionosphere. *Australian Journal of Physics*, **9**, 161–166. doi:10.1071/PH560161.

Mayaud, P. (1967). Atlas of indices K, Part 1,. *IAGA Bulletinitalics*. doi:10.1007/978-3-642-78717-$1_2$6.

Mayr, H., Harris, I., Spencer, N., Hedin, A., Wharton, L., Porter, H., Walker, J. & Carlson Jr, H. (1979). Tides and the midnight temperature anomaly in the thermosphere. *Geophysical Research Letters*, **6**, 447–450. doi:10.1029/GL006i006p00447.

McLandress, C., Shepherd, G.G. & Solheim, B.H. (1996). Satellite observations of thermospheric tides: Results from the Wind Imaging Interferometer on UARS. *Journal of Geophysical Research: Atmospheres*, **101**, 4093–4114. doi:10.1029/95JD03359.

McNamara, L.F. (1991). *The ionosphere: communications, surveillance, and direction finding*. Krieger publishing company. ISBN-13: 978-0894640407.

Mende, S., Swenson, G., Geller, S., Viereck, R., Murad, E. & Pike, C. (1993). Limb view spectrum of the earth's airglow. *Journal of Geophysical Research: Space Physics*, **98**, 19117–19125. doi:10.1029/93JA02282.

Menvielle, M. & Berthelier, A. (1991). The K-derived planetary indices: Description and availability. *Reviews of Geophysics*, **29**, 415–432. doi:10.1029/91RG00994.

Meriwether, J., Faivre, M., Fesen, C., Sherwood, P. & Veliz, O. (2008). New results on equatorial thermospheric winds and the midnight temperature maximum. In *Annales Geophysicae*, **26**, 447–466. doi: 10.5194/angeo-26-447-2008.

Meriwether, J. (2006). Studies of thermospheric dynamics with a Fabry–Perot interferometer network: A review. *Journal of Atmospheric and Solar-Terrestrial physics*, **68**, 1576–1589. doi: 10.1016/j.jastp.2005.11.014.

Meriwether Jr, J., Tepley, C., Price, S., Hays, P. & Cogger, L. (1983). Remote ground-based observations of terrestrial airglow emissions and thermospheric dynamics at Calgary, Alberta, Canada. *Optical Engineering*, **22**, 221128. doi:10.1117/12.7973060.

Merzlyakov, E., Jacobi, C., Portnyagin, Y.I. & Solovjova, T. (2009). Structural changes in trend parameters of the MLT winds based on wind measurements at Obninsk and Collm. *Journal of Atmospheric and Solar-Terrestrial Physics*, **71**, 1547–1557. doi: 10.1016/j.jastp.2009.05.013

Miller, K., Torr, D. & Richards, P. (1986). Meridional winds in the thermosphere derived from measurement of F2 layer height. *Journal of Geophysical Research: Space Physics*, **91**, 4531–4535. doi:10.1029/JA091IA04P04531.

Moldwin, M. (2008). *An introduction to space weather*, (Vol. 1). Cambridge University Press. ISBN: 9780511801365.

Muella, M., Fagundes, P., Bittencourt, J., Sahai, Y., Lima, W., Becker-Guedes, F. & Pillat, V. (2008). Nighttime thermospheric meridional neutral winds inferred from ionospheric h'F and hpF2 data. *Advances in Space Research*, **41**, 599–610. doi: 10.1016/j.asr.2007.09.032.

Myrabø, H. (1984). Temperature variation at mesopause levels during winter solstice at 78^0N. *Planetary and Space Science*, **32**, 249–255. doi.org/10.1016/0032-0633(84)90159-4.

Nwankwo, V.U. & Chakrabarti, S.K. (2018). Effects of space weather on the ionosphere and LEO satellites orbital trajectory in equatorial, low and middle latitude. *Advances in Space Research*, **61**, 1880–1889. /doi:10.1016/j.asr.2017.12.034.

Oberheide, J., Hagan, M., Roble, R. & Offermann, D. (2002). Sources of nonmigrating tides in the tropical middle atmosphere. *Journal of Geophysical Research: Atmospheres*, **107**, 4567. doi: 10.1029/2002JD002220.

Oberheide, J., Forbes, J., Zhang, X. & Bruinsma, S. (2011). Climatology of upward propagating diurnal and semidiurnal tides in the thermosphere. *Journal of Geophysical Research: Space Physics*, **116**, A11. doi: 10.1029/2011JA016784.

Oberheide, J., Hagan, M., Richmond, A. & Forbes, J. (2015). Dynamical meteorology— atmospheric tides. *In North, G.R., Pyle J. Zhang, F. (Eds.)Encyclopedia of Atmospheric Sciences (2nd ed.) (pp. 287-297).* Elsevier. ISBN: 9780123822253.

Oliver, W., Martinis, C., Hickey, D., Wright, A. & Amory-Mazaudier, C. (2012). A night-time temperature maximum in the thermosphere above Saint Santin in winter. *Journal of Geophysical Research: Space Physics*, **117**, A06324. doi:10.1029/2012JA017855.

Oznovich, I., McEwen, D., Sivjee, G. & Walterscheid, R. (1997). Tidal oscillations of the Arctic upper mesosphere and lower thermosphere in winter. *Journal of Geophysical Research: Space Physics*, **102**, 4511–4520. doi:10.1029/96JA03560.

Parish, H., Fuller-Rowell, T., Rees, D., Virdi, T. & Williams, P. (1990). Numerical simulations of the seasonal response of the thermosphere to propagating tides. *Advances in Space Research*, **10**, 287–291.doi: 10.1016/0273-1177(90)90262-X.

Park, J., Lühr, H. & Min, K.W. (2010). Characteristics of F-region dynamo currents deduced from CHAMP magnetic field measurements. *Journal of Geophysical Research: Space Physics*, **115**, A10302. doi:10.1029/2010JA015604.

Paulino, A., Batista, P. & Batista, I. (2013). A global view of the atmospheric lunar semidiurnal tide. *Journal of Geophysical Research: Atmospheres*, **118**, 13128–13139. doi.org/10.1002/2013JD019818.

Pesnell, W.D., Omidvar, K. & Hoegy, W.R. (1993). Momentum transfer collision frequency of O^+-O. *Geophysical Research Letters*, **20**, 1343–1346. doi:10.1029/93GL01597.

Picone, J., Hedin, A., Drob, D.P. & Aikin, A. (2002). NRLMSISE-00 empirical model of the atmosphere: Statistical comparisons and scientific issues. *Journal of Geophysical Research: Space Physics*, **107**, 1468-1470 . doi:10.1029/2002JA009430.

Portnyagin, Y.I., Forbes, J., Fraser, G., Vlncent, R., Avery, S., Lysenko, I. & Makarov, N. (1993). Dynamics of the Antarctic and Arctic mesosphere and lower thermosphere regionsII. The semidiurnal tide. *Journal of Atmospheric and Terrestrial Physics*, **55**, 843–855. doi: 10.1016/0273-1177(92)90449-8.

Press, W.H. & Rybicki, G.B. (1989). Fast algorithm for spectral analysis of unevenly sampled data. *The Astrophysical Journal*, **338**, 277–280. doi:10.1086/167197.

Prölss, G.W. (2004). Neutral upper atmosphere. In *Physics of the Earths Space Environment* (pp. 11-76). Springer. ISBN: 978-3-642-97123-5.

Rabiu, A., Okoh, D., Wu, Q., Bolaji, O., Abdulrahim, R., Dare-Idowu, O. & Obafaye, A. (2021). Investigation of the variability of night-time equatorial thermospheric winds over Nigeria, West Africa. *Journal of Geophysical Research: Space Physics*, **126**, e2020JA028528. doi:10.1029/2020JA028528

Ranade, J. (1950). Application of the Fabryo-Perot interferrometer for high resolution studies. Royal Holloway College, United Kingdom. ISBN: 9781339606644.

Ratcliffe, J.A. *et al.* (1972). *An introduction to ionosphere and magnetosphere*. Cambridge University Press. ISBN 05210834199780521083416.

Rawer, K., Bilitza, D. & Ramakrishnan, S. (1978). Goals and status of the International Reference Ionosphere. *Reviews of Geophysics*, **16**, 177–181. doi: 10.1029/RG016i002p00177.

Reddy, C., Hoegy, W., Pesnell, W., Mayr, H. & Hines, C. (1994). Accuracy of O^+-O collision cross-section deduced from ionosphere-thermosphere observations. *Geophysical research letters*, **21**, 2429–2432.doi:10.1029/94GL02494.

Rees, D. (1995). Observations and modelling of ionospheric and thermospheric disturbances during major geomagnetic storms: A review. *Journal of Atmospheric and Terrestrial Physics*, **57**, 1433–1457. doi:10.1016/0021-9169(94)00142-B.

Reinisch, B., Galkin, I., Khmyrov, G., Kozlov, A. & Kitrosser, D. (2005). Automated collection and dissemination of ionospheric data from the digisonde network. *Advances in Radio Science*, **2**, 241–247. doi:10.5194/ars-2-241-2004.

Richards, P. (1991). An improved algorithm for determining neutral winds from the height of the F2 peak electron density. *Journal of Geophysical Research: Space Physics*, **96**, 17839–17846. doi:10.1029/91JA01467.

Richmond, A., Ridley, E. & Roble, R. (1992). A thermosphere/ionosphere general circulation model with coupled electrodynamics. *Geophysical Research Letters*, **19**, 601–604. doi:10.1029/92GL00401

Rishbeth, H. (1967). The effect of winds on the ionospheric F2-peak. *Journal of Atmospheric and Terrestrial Physics*, **29**, 225–238. doi:10.1016/0021-9169(68)90041-X.

Rishbeth, H. (1972). Thermospheric winds and the F-region: A review. *Journal of Atmospheric and Terrestrial Physics*, **34**, 1–47. doi:10.1016/0021-9169(72)90003-7.

Rishbeth, H. (2000). The equatorial F-layer: progress and puzzles. In *Annales Geophysicae*, 18, 730-739. doi.org/10.1007/s00585-000-0730-6.

Rishbeth, H. & Garriott, O.K. (1969). *Introduction to ionospheric physics*, vol. 14. Academic Press New York. ISBN: 978-0-12-588940-7.

Rishbeth, H., Ganguly, S. & Walker, J. (1978). Field-aligned and field-perpendicular velocities in the ionospheric F2-layer. *Journal of Atmospheric and Terrestrial Physics*, **40**, 767–784. doi: 10.1016/0021-9169(78)90028-4.

Ruan, H., Lei, J., Dou, X., Zhang, S.R., Noto, J. & Kapali, S. (2013). Enhancements of nighttime neutral and ion temperatures in the F region over Millstone Hill. *Journal of Geophysical Research: Space Physics*, **118**, 1768–1776. doi: 10.1002/jgra.50202.

Sahai, Y., Takahashi, H., Fagundes, P., Clemesha, B., Teixeira, N. & Bittencourt, J. (1992). Observations of thermospheric neutral winds at 23^0. *Planetary and Space Science*, **40**, 767–773. doi:10.1016/0273-1177(95)00169-F.

Salah, J.E. (1993). Interim standard for the ion-neutral atomic oxygen collision frequency. *Geophysical Research Letters*, **20**, 1543–1546. doi:10.1029/93GL01699.

Scargle, J.D. (1982). Studies in astronomical time series analysis. II-statistical aspects of spectral analysis of unevenly spaced data. *The Astrophysical Journal*, **263**, 835–853. doi: 10.1086/160554.

Schunk, R. & Nagy, A. (2009). *Ionospheres: physics, plasma physics, and chemistry*. University press. doi.org/10.1017/CBO9780511635342.

Sergeyeva, N., Gvishiani, A., Soloviev, A., Zabarinskaya, L., Krylova, T., Nisilevich, M. & Krasnoperov, R. (2021). Historical K index data collection of soviet magnetic observatories, 1957–1992. *Earth System Science Data*, **13**, 1987–1999. doi:10.5194/essd-13-1987-2021.

She, C., Chen, S., Williams, B., Hu, Z., Krueger, D.A. & Hagan, M. (2002). Tides in the mesopause region over Fort Collins, Colorado ($41°N$, $105°W$) based on lidar temperature observations covering full diurnal cycles. *Journal of Geophysical Research: Atmospheres*, **107**, 2–9. doi: 10.1029/2001JD001189.

Sipler, D.P. & Biondi, M.A. (1978). Equatorial F-region neutral winds from nightglow OL 630.0 nm Doppler shifts. *Geophysical Research Letters*, **5**, 373–376. doi:10.1029/GL005i005p00373.

Sivjee, G., Walterscheid, R. & McEwen, D. (1994). Planetary wave disturbances in the arctic winter mesopause over eureka (80° N). *Planetary and Space Science*, **42**, 973–986. doi.org/10.1016/0032-0633(94)90057-4.

Sivla, W., Ogunjobi, O., Okoro, E., Ugonabo, O. & Orji, P. (2019). Thermospheric neutral winds over Abuja, Nigeria. International Journal of Physical Sciences, **42**, 15-20. doi: 10.5897/IJPS2018.4773.

Spencer, N., Wharton, L., Carignan, G. & Maurer, J. (1982). Thermosphere zonal winds, vertical motions and temperature as measured from Dynamics Explorer. *Geophysical Research Letters*, **9**, 953–956. doi:10.1029/GL009i009p00953.

Taylor, K.E. (2001). Summarizing multiple aspects of model performance in a single diagram. *Journal of Geophysical Research: Atmospheres*, **106**, 7183–7192. doi:10.1029/2000JD900719.

Teitelbaum, H., Vial, F., Manson, A., Giraldez, R. & Massebeuf, M. (1989). Non-linear interaction between the diurnal and semidiurnal tides: Terdiurnal and diurnal secondary waves. *Journal of Atmospheric and Terrestrial Physics*, **51**, 627–634. doi:10.1016/0021-9169(89)90061-5.

Tesema, F., Mesquita, R., Meriwether, J., Damtie, B., Nigussie, M., Makela, J., Fisher, D., Harding, B., Yizengaw, E. & Sanders, S. (2017). New results on equatorial thermospheric winds and temperatures from Ethiopia, Africa. *Annales Geophysicae*, **35(2)**, 333-344. doi:10.5194/angeo-35-333-2017.

Thayaparan, T. (1997). The terdiurnal tide in the mesosphere and lower thermosphere over London, Canada (43○N, 81○ W). *Journal of Geophysica Research: Atmospheres*, **102**, 21695–21708. doi:10.1186/BF03351823.

Titheridge, J. (1995a). The calculation of neutral winds from ionospheric data. *Journal of Atmospheric and Terrestrial Physics*, **57**, 1015–1036. doi:10.1016/0021-9169(94)00106-X.

Titheridge, J. (1995b). Winds in the ionospherea review. *Journal of Atmospheric and Terrestrial Physics*, **57**, 1681–1714. doi:10.1016/0021-9169(95)00091-F.

Torr, D. & Torr, M.R. (1979). Chemistry of the thermosphere and ionosphere. *Journal of Atmospheric and Terrestrial Physics*, **41**, 797–839. doi: 10.1016/0021-9169(79)90126-0

Vasseur, G. (1969). Dynamics of the F-region observed with Thomson-scatterI Atmospheric circulation and neutral winds. *Journal of Atmospheric and Terrestrial Physics*, **31**, 397–420. doi: 10.1016/0021-9169(69)90066-X.

Vaughan, J. (1989). The Fabry-Perot interferometer. IOP Publishing. ISBN: 0852741383 9780852741382.

Venkateswara Rao, N., Tsuda, T., Gurubaran, S., Miyoshi, Y. & Fujiwara, H. (2011). On the occurrence and variability of the terdiurnal tide in the equatorial mesosphere and lower thermosphere and a comparison with the Kyushu-GCM. *Journal of Geophysical Research: Atmospheres*, **116**, D02117. doi: 10.1029/2010JD014529.

Villard Jr, O.G. (1976). The ionospheric sounder and its place in the history of radio science. *Radio Science*, **11**, 847–860. doi: 10.1029/RS011i011p00847

Walterscheid, R. & Sivjee, G. (1996). Very high frequency tides observed in the airglow over Eureka (80°). *Geophysical Research Letters*, **23**, 3651–3654. doi:10.1029/96GL03482.

Walterscheid, R., Sivjee, G., Schubert, G. & Hamwey, R. (1986). Large-amplitude semidiurnal temperature variations in the polar mesopause: evidence of a pseudotide. *Nature*, **324**, 347–349. doi.org/10.1038/324347a0.

Wang, H., Boyd, J. & Akmaev, R. (2016). On computation of Hough functions. *Geoscientific Model Development*, *9*, 1477–1488. doi:10.5194/gmd-9-1477-2016.

Wang, J., Yi, W., Wu, J., Chen, T., Xue, X., Vincent, R.A., Reid, I.M., Batista, P.P., Buriti, R.A., Tsuda, T. *et al.* (2021). Climatology of migrating and non-migrating tides observed by three meteor radars in the southern equatorial region. *Atmospheric Chemistry and Physics Discussions*, 9,1–28. doi:10.5194/acp-2021-33.

Wu, Q., Killeen, T., Ortland, D., Solomon, S., Gablehouse, R., Johnson, R., Skinner, W., Niciejewski, R. & Franke, S. (2006). Timed doppler interferometer (TIDI) observations of Migrating diurnal and semidiurnal tides. *Journal of atmospheric and Solar-Terrestrial Physics*, **68**, 408–417. /doi:10.1016/j.jastp.2005.02.031.

Wu, Q., Ortland, D., Killeen, T., Roble, R., Hagan, M., Liu, H.L., Solomon, S., Xu, J., Skinner, W. & Niciejewski, R. (2008). Global distribution and interannual variations of mesospheric and lower thermospheric neutral wind diurnal tide: 1. migrating tide. *Journal of Geophysical Research: Space Physics*, **113**,A05308, doi: 10.1029/2007JA012542

Wu, Q., Sheng, C., Wang, W., Noto, J., Kerr, R., McCarthy, M., Huang, C., Zhang, X. & Sarris, T. (2019). The Midlatitude Thermospheric Dynamics From an Interhemispheric Perspective. *Journal of Geophysical Research: Space Physics*, **124**, 7971–7983. doi:10.1029/2019JA026967.

Xu, H., Shiokawa, K., Oyama, S.I. & Nozawa, S. (2019). High-latitude thermospheric wind study using a Fabry–Perot interferometer at Tromsø in Norway: averages and variations during quiet times. *Earth, Planets and Space*, **71**, 1–8. doi: 10.1186/s40623-019-1093-8.

Xu, J., Smith, A., Jiang, G., Yuan, W. & Gao, H. (2012). Features of the seasonal variation of the semidiurnal, terdiurnal and 6-h components of ozone heating evaluated from Aura/MLS observations. *Annales Geophysicae*, **30**, 259–281. doi:10.5194/angeo-30-259-2012.

Xu, J., Smith, A., Liu, M., Liu, X., Gao, H., Jiang, G. & Yuan, W. (2014). Evidence for nonmigrating tides produced by the interaction between tides and stationary planetary waves in the stratosphere and lower mesosphere. *Journal of Geophysical Research: Atmospheres*, **119**, 471–489. doi: 10.1002/2013JD020150.

Yagi, T. & Dyson, P. (1985). The response of the mid-latitude thermospheric wind to magnetic activity. *Planetary and Space Science*, **33**, 461–467. doi:10.1016/0032-0633(85)90090-X.

Yu, T., Huang, C., Zhao, G., Mao, T., Wang, Y., Zeng, Z., Wang, J. & Xia, C. (2014). A preliminary study of thermosphere and mesosphere wind observed by Fabry-Perot over Kelan, China. *Journal of Geophysical Research: Space Physics*, **119**, 4981–4997. doi: 10.1002/2013JA019492.

Yuan, W., Liu, X., Xu, J., Zhou, Q., Jiang, G., Ma, R. *et al.* (2013). FPI observations of nighttime mesospheric and thermospheric winds in China and their comparisons with HWM07. *Ann. Geophys*, **31**, 1365–1378. doi: 10.5194/angeo-31-1365-2013.

Zhang, X., Forbes, J.M., Hagan, M.E., Russell III, J.M., Palo, S.E., Mertens, C.J. & Mlynczak, M.G. (2006). Monthly tidal temperatures 20–120 km from TIMED/SABER. *Journal of Geophysical Research: Space Physics*, **111**, A10S08. doi:10.1029/2005JA011504.

Zhao, G., Liu, L., Ning, B., Wan, W. & Xiong, J. (2005). The terdiurnal tide in the mesosphere and lower thermosphere over Wuhan (30○N, 114°E). *Earth, planets and space*, **57**, 393–398. doi.org/10.1186/BF03351823.

Zhou, Q.H., Sulzer, M.P. & Tepley, C.A. (1997). An analysis of tidal and planetary waves in the neutral winds and temperature observed at low-latitude E region heights. *Journal of Geophysical Research: Space Physics*, **102**, 11491–11505. doi.org/10.1029/97JA00440.

Zmuda, A. (1971). The International geomagnetic reference field 1965.0: introduction. *Bull. Int. Assoc. Geomag. Aeron.*, **28**, 148–152. https://ci.nii.ac.jp/naid/10003531535/en/.

Zolesi, B. & Cander, L.R. (2014). *Ionospheric prediction and forecasting*. Springer. ISBN: 978-3-642-38430-1.